Title
Spin transport in ferromagnets, antiferromagnets, paramagnets, and nuclear spins

Author
Reitz, Derek

Publication Date
2023

Peer reviewed|Thesis/dissertation

UNIVERSITY OF CALIFORNIA

Los Angeles

Spin Transport In Ferromagnets, Antiferromagnets, Paramagnets, And Nuclear Spins

A thesis submitted in partial satisfaction

of the requirements for the degree Doctor of Philosophy

in Physics

by

Derek Russel Reitz

2023

ABSTRACT OF THE THESIS

Spin Transport In Ferromagnets, Antiferromagnets, Paramagnets, And Nuclear Spins

by

Derek Russel Reitz

Doctor of Philosophy in Physics

University of California, Los Angeles, 2023

Professor Yaroslav Tserkovnyak, Chair

The central scientific objective in this thesis is to develop experimentally-testable theories for the dynamical behavior of magnetic systems. Our second objective is to use our understanding of these systems to investigate their potential for generating thermally-induced spin currents, ultimately having thermoelectric applications. This phenomena is known as the spin Seebeck effect. In Chapter 1, we derive the low-energy, long-wavelength spectra of Heisenberg ferromagnets (FMs) and antiferromagnets (AFs), in their strongly-ordered regimes, from an intuitive starting point in a classical theory. Once quantized, these spin excitations become magnons. The strongly ordered phases are understood as a dilute magnon gas, but interactions become increasingly complex as we approach the magnetic transition temperature in 3D. In order to pursue a theory of magnetism which treats all phases–both ordered and disordered–on equal footing, we turn to Schwinger boson mean field theory (SBMFT). The Schwinger boson transformation fractionalizes the spin operators into two bosonic field operators, and the language initially appears to be less intuitive. Nonetheless, we will show how two-spinon excitations reproduce magnons, and then press on to regimes where both magnon-like and paramagnetic-like excitations proliferate in thermal equilibrium.

In Chapter 2, we investigate the dynamical linear response of insulating magnetic systems

in equilibrium. In the ordered phases, where time-reversal symmetry is broken, we find that spin currents are present in equilibrium. The thermally-averaged spin-spin correlators, which make up spin currents, may be evaluated from the dissipative part of the dynamic susceptibility tensor using the semiclassical fluctuation-dissipation theorem (FDT). Since spin currents are not directly measurable, we interface the insulating magnet with a metal. The interface acts as weak link, and when the two are out-of-equilibrium with each other, a spin current flows across the interface. By the inverse spin Hall effect, this is picked up as a voltage drop across the metal. In the FDT method, we compute the interfacial spin current up to an overall phenomenological parameter called the (dissipative part of the) spin-mixing conductance. An alternative method, used for Schwinger bosons, is to compute the interfacial spin current directly using Fermi's golden rule.

In Chapter 3, we summarize and analyze our final results for the spin Seebeck coefficients in FMs, AFs, PMs, and discuss a novel SSE which is relevant at temperatures below where electronic spin dynamics freeze out – the nuclear SSE. In Chapter 4, we compare our results to experiments on the AF SSE in chromium oxide (Cr_2O_3), the paramagnetic SSE in gadolinium gallium garnet (GGG), and the nuclear SSE in manganese carbonate ($MnCO_3$). We discovered remarkable quantitative agreement between our theory and the Cr_2O_3 data after comparing the SSE across a metamagnetic phase transition. Here, the overall thermal and electronic transport properties such as thermal conductivities and metallic resistivities which affect the measured SSE were eliminated in this comparison, because they are unaffected by the magnetic configuration of the AF. We then applied this technique to the paramagnetic and nuclear SSE analysis to extract additional, specific information from the overall magnetic field profile of the SSE. Finally, we conclude with predictions from SBMFT for future experimental proposals. These investigate the strength of paramagnetic fluctuations in ordered magnetic phases and signatures of magnetic correlations in disordered phases.

The dissertation of Derek Russel Reitz is approved.

Anshul Kogar

Rahul Roy

Seth J. Putterman

Yaroslav Tserkovnyak, Committee Chair

University of California, Los Angeles

2023

DEDICATION

In loving memory of my grandfather, Bob Reitz, whose passion for teaching physics was an inspiration to all.

TABLE OF CONTENTS

LIST OF FIGURES

Page

ACKNOWLEDGMENTS

Work completed for this dissertation was was supported by the U.S. Department of Energy, Office of Basic Energy Sciences under Award No. DE-SC0012190, the Bhaumik Institute for Theoretical Physics, and the UCLA Dissertation Year Fellowship.

I acknowledge the work of Takahashi Kikkawa, Eiji Saitoh, and colleagues, whose ultra low temperature spin transport experiments greatly motivated my PhD work on the nuclear spin Seebeck effect. I also acknowledge the work of Junxue Li, Jing Shi, and colleagues, whose experimental data on spin transport in antiferromagnets was the first to demonstrate the striking behavior of the antiferromagnetic spin Seebck effect around a metamagnetic phase transition, which is understood from our theory. As a theorist, being able to compare one's work to experiment directly over the course of one's PhD is a great honor and privilege.

I would also like to thank my advisor, Yaroslav Tserkovnyak, for the incredible opportunity to be a part of an exciting and engaging scientific group, where new ideas were generated on a weekly basis. Yaroslav's intuition for condensed matter physics is extraordinary, and he has a deep appreciation for understanding the meaning and purpose in science. I am grateful to take a small part of this with me for the rest of my life.

VITA

Derek Russel Reitz

B.S. in Physics **2018**

The Johns Hopkins University *Baltimore, MD*

Teaching assistant and graduate student researcher **2018-2022**

University of California, Los Angeles *Los Angeles, CA*

Dissertation year fellowship **2022-2023**

University of California, Los Angeles *Los Angeles, CA*

Principal transformational physicist **2023-**

Northrop Grumman Corporation *Baltimore, MD*

PUBLICATIONS

1. Derek Reitz, Junxue Li, Wei Yuan, Jing Shi, and Yaroslav Tserkovnyak. Spin Seebeck Effect near the Antiferromagnetic Spin-Flop Transition. Phys. Rev. B 102, 020408, July 2020.

2. Junxue Li, Haakon T Simensen, Derek Reitz, Qiyang Sun, Wei Yuan, Chen Li, Yaroslav Tserkovnyak, Arne Brataas, Jing Shi. Observation of magnon polarons in a uniaxial antiferromagnetic insulator. Phys. Rev. Lett. 125, 217201. November 2020.

3. Kyongmo An, Ryuhei Kohno, Nicolas Thiery, Derek Reitz, Laurent Vila, Vladimir V Naletov, Nathan Beaulieu, J Ben Youssef, Grégoire de Loubens, Yaroslav Tserkovnyak, Olivier Klein. Short-range thermal magnon diffusion in magnetic garnet. Phys. Rev. B 103, 174432, May 2021.

4. Takashi Kikkawa, Derek Reitz, H Ito, Takahiko Makiuchi, T Sugimoto, K Tsunekawa, Shunsuke Daimon, Koichi Oyanagi, R Ramos, Satoshi Takahashi, Yuki Shiomi, Yaroslav

Tserkovnyak, Eiji Saitoh. Observation of nuclear-spin Seebeck effect. Nature Communications 12, 4356, July 2021.

5. Derek Reitz, Yaroslav Tserkovnyak. Spin transport from order to disorder. *Unpublished*, 2023.

6. Rodolfo Rodriguez and Derek Reitz, Shirash Regmi, Allison Tossounian, Yaroslav Tserkovnyak, Igor Barsukov. Magnetic damping of antiferromagnetic Cr_2O_3 crystals. *Unpublished*, 2023.

Chapter 1

Introduction to the spin wave spectra of magnetic systems

In this chapter, we derive the spectra of linear excitations in ferromagnets (FMs), antiferromagnets (AFs), and paramagnets (PMs). The dispersive bandwidth of spin excitations is set by the Heisenberg exchange constant times, loosely speaking, the average strength of spin-spin correlations. On the other hand, the band gap generally comes from a uniform, effective magnetic field, which may be comprised of crystalline anisotropies and external magnetic fields, for example. The FM and AF exchange interactions result in different dispersions near the bottom of the band: FM exchange results in quadratic dispersion, while AF exchange results in linear dispersion. If we take this as one baseline difference between FMs and AFs, it is then not surprising that the behaviors of the two systems differ significantly at low temperatures, where only the lowest-energy excitations are thermalized. In addition, as we will investigate in more detail in Chapter 2, there can be major qualitative differences in the overall character of linear response (dynamics of linear excitations) of strongly-ordered FMs and AFs.

To illustrate their separate character, consider a FM (AF) which has an easy axis along which there is magnetic (Néel – staggered) ordering, respectively, at temperatures well below where the FM (AF) transition occurs – the Curie (Néel) temperature $T_{C(N)}$. In Chapter 2, we will find that once a small magnetic field is applied collinear to the easy axis, the spin current in the AF at $T \ll T_N$ carries spin angular momentum that is oppositely-oriented to the FM's at $T \ll T_C$! The origin of this striking difference becomes apparent after studying the lowest-energy spin excitations, called magnons, of the two systems. Magnons are bosons, carrying spin angular momentum $\hbar$. In FMs at $T \ll T_C$, nearly all the spins are oriented along the same direction, and so magnons are spin flips, with spin polarization opposite the magnetic order. In AFs at $T \ll T_N$, nearly all the spins are staggered, pointing in one of two directions along a given axis. Again, since magnons are spin flips, intuitively one would expect two magnon branches in the AF (which are degenerate in the absence of magnetic field). In the absence of canting, the two magnons carry oppositely-oriented spin angular momentum along the Néel axis. This is the case for the easy-axis AF at low fields, and the magnons which carry momentum polarized along the direction of the magnetic field are in the majority (in terms of thermal occupation numbers), so they determine the net polarization of the spin current. A second class are canted AFs, which instead behave qualitatively similar to a weak FM. We discuss both.

Well ordered FMs (AFs) (when $T \ll T_{C(N)}$) have magnetic (Néel) order which can be described by a classical, rigid vector. In a classical theory, spin waves are transverse oscillations of the order parameter. Once quantized, they become magnons. We construct the classical theory for the low energy, long-wavelength excitations by expanding in small transverse deformations of the order parameter (a gradient expansion). In 3D, the phenomenological parameters in the classical Hamiltonian may be obtained, from first principles, by the classical limit $S \to \infty$ of the quantum Heisenberg model [4], which remains reliable for low spin lengths in 3D.

In order to treat magnetic systems at arbitrary temperature on the same footing, we must resort to mean-field theory. The Schwinger boson transformation takes SU(N) generators to a product of N bosonic operators. The Hamiltonian is then decoupled by a Hubbard-Stratonovich transformation where the mean-field theory is the saddle point (SP), and the order n fluctuations about the SP scale as $O(1/N^n)$ [5, 6]. This approach has no small or large parameter for fixed $N \sim 1$, but still has the ability to qualitatively capture essential physics in regimes where we do not have an accurate theory.

1.1 Phenomenological theories for magnetic systems

In this section, our goal is to pursue a straightforward route to obtaining the lowest-energy excitations of an arbitrary FM or AF insulator at temperatures well below its ordering temperature. Since the central quantity which describes a magnet is its order parameter, we will start by using it to construct a conjugate pair of coordinate and momentum. We will then write down the Hamiltonian for these generalized coordinates whose form is intuitive. Moreover, Hamilton's equations of motion are first order differential equations and can be solved immediately after linearization, yielding the spin wave spectra. While the generalized coordinates offer an intuitive path for constructing the equations of motion, it will be most convenient to parameterize the phenomenological quantities in the Hamiltonian as energetic coefficients for the stiffness and anisotropy of the order parameter itself.

1.1.1 Strongly ordered ferromagnets

In ferromagnets at $T \ll T_C$, the thermal equilibrium state is strongly ordered with spin density $\boldsymbol{m} = (\sin\theta\cos\phi, \sin\theta\cos\phi, \cos\theta)$, where $\boldsymbol{m}^2 = 1$ is valid when the longitudinal fluctuations are frozen out. The conjugate coordinates are the spin projected along an

arbitrary axis, e.g. m^z, and the angle between its transverse component and another axis, e.g. the angle ϕ between $\boldsymbol{m}_\perp$ and the x-axis [7] (one can verify $\cos\theta$ and $-\phi$ are conjugate from the Poisson algebra $\{m^z, m^+\} = -im^+$ with $m^+ = m_x + im^y$). The Hamiltonian of the Heisenberg ferromagnet is

$$H(m^z, -\phi) = A\left[(\nabla m^z)^2/m_\perp^2 + m_\perp^2(\nabla\phi)^2\right]/2, \tag{1.1}$$

where $m_\perp^2 = 1-(m^z)^2$ and A is the spin stiffness. Notably, there is no kinetic term. We work well below the ordering temperature T_N, so that we retain only the lowest-order gradient term of the Néel order. Hamilton's equations are $\partial_t m^z \equiv \dot{m^z} = \delta H/\delta\phi$ and $-\dot{\phi} = -\delta H/\delta\phi$. Next we insert Hamilton's equations into $d\boldsymbol{m}/dt = (\partial\boldsymbol{m}/\partial m^z)\dot{m^z} + (\partial\boldsymbol{m}/\partial\phi)\dot{\phi} \equiv \dot{\boldsymbol{m}}$ and compare it to the quantity

$$\boldsymbol{m} \times \frac{\delta E}{\delta \boldsymbol{m}} \equiv \boldsymbol{m}(m^z, \phi) \times \left(\frac{\delta H}{\delta m^z}\frac{\delta m^z}{\delta \boldsymbol{m}} + \frac{\delta H}{\delta \phi}\frac{\delta \phi}{\delta \boldsymbol{m}}\right), \tag{1.2}$$

which yields the Landau-Lifshitz equation

$$\dot{\boldsymbol{m}} = \dot{\boldsymbol{m}} \times \boldsymbol{\Omega}, \;\; \boldsymbol{\Omega} = \frac{\delta E}{\delta \boldsymbol{m}}, \tag{1.3}$$

and the energy density $E(\boldsymbol{m}) = H(m^z, -\phi)$.

For example, in the case of uniaxial anisotropy with constant K and collinear applied field, the total energy density reads

$$E(\boldsymbol{m}) = A(\boldsymbol{\nabla}\boldsymbol{m})^2/2 + K(\hat{\boldsymbol{K}} \cdot \boldsymbol{m})^2/2 - \boldsymbol{b} \cdot \boldsymbol{m}, \tag{1.4}$$

where $\boldsymbol{b} \equiv \gamma s \boldsymbol{B}$ and γ is the gyromagnetic ratio, whose sign is lumped into the value of B; e.g., for free electrons, our B has opposite sign to the applied field. The spin waves are found

by inserting $\boldsymbol{m} = \boldsymbol{m}_0 + \delta\boldsymbol{m}$ into the equations of motion, giving the dispersion

$$\omega_k = \gamma(B + K) + Ak^2, \tag{1.5}$$

which is the real part of the eigenvalues; and the decay rate

$$\epsilon_k = \alpha\omega_k. \tag{1.6}$$

which is the imaginary part. The quality factor is $\boldsymbol{k} \equiv \omega_k/\epsilon_k = \alpha^{-1}$. The eigenvectors are damped, circularly-polarized spin waves.

Resonance dragging effect. The dragging effect is the change in field linewidth due to a change in angle between the applied field and the order parameter (see, e.g., Ref. [8]). Measuring this effect allows the direction of the order parameter to be determined. For a ferromagnet with uniaxial anisotropy constant K (or equivalently, an approximately uniform dipolar field such as in a thin film) the field linewidth for $k = 0$ as a function of θ is $\Delta B = \Delta\omega\partial B/\partial\omega = \Delta\omega/\cos\theta$. For inhomogenous broadening $\Delta^{IB}\omega$, the result is

$$\Delta_{FM}B(\theta) = \frac{\Delta^{IB}\omega/\gamma + \alpha(K + B\cos\theta)}{\cos\theta}. \tag{1.7}$$

In the limit $B \ll K$, $\Delta_{FM}B(\theta) \approx C/\cos\theta$.

1.1.2 Strongly ordered antiferromagnets

In antiferromagnets at temperatures $T \ll T_N$, the thermal equilibrium state is strongly ordered. The AF state is parameterized by directional Néel order $\boldsymbol{l}$ and normalized spin density $\boldsymbol{m} = \mathbf{s}/s$ ($\mathbf{s}$ being the spin density and $s \equiv \hbar S/V$, for spin S and volume V per site), in a nonlinear σ model with constraint $\boldsymbol{l}^2 = 1$ and $\boldsymbol{l} \cdot \boldsymbol{m} = 0$. The Hamiltonian of the

Heisenberg antiferromagnet is

$$H(\boldsymbol{l},\boldsymbol{p}) = A(\boldsymbol{\nabla l})^2/2 + \boldsymbol{p}^2/2m, \tag{1.8}$$

where $\boldsymbol{p} = \boldsymbol{m} \times \boldsymbol{l}$ is the conjugate momentum (as one can verify from the Poisson algebra $\{l^z, l^+\} = -il^+$ with $l^+ = l^x + il^y$ and analogous relations for $\boldsymbol{m}$). Notably, there is a kinetic term. Hamilton's equations are $\dot{\boldsymbol{l}} = \delta H/\delta \boldsymbol{p}$ and $\dot{\boldsymbol{p}} = -\delta H/\delta \boldsymbol{l}$. Next we insert Hamilton's equations into $d\boldsymbol{p}/dt = (\partial \boldsymbol{p}/\partial \boldsymbol{l})\dot{\boldsymbol{l}} + (\partial \boldsymbol{p}/\partial \boldsymbol{m})\dot{\boldsymbol{m}} \equiv \dot{\boldsymbol{p}}$, in the same fashion as Eq.(1.2) for the FM, and use $\boldsymbol{l}^2 = 1$, $\boldsymbol{l}\cdot\boldsymbol{m} = 0$ along with the vector identity $\boldsymbol{A}\times(\boldsymbol{B}\times\boldsymbol{C}) = \boldsymbol{B}(\boldsymbol{A}\cdot\boldsymbol{C}) - \boldsymbol{C}(\boldsymbol{A}\cdot\boldsymbol{B})$ to obtain the equations of motion for the nonlinear-σ model [9]:

$$\dot{\boldsymbol{l}} = \boldsymbol{m} \times \frac{\delta E}{\delta \boldsymbol{l}}, \tag{1.9}$$

$$\dot{\boldsymbol{m}} = \boldsymbol{m} \times \frac{\delta E}{\delta \boldsymbol{m}} + \boldsymbol{l} \times \frac{\delta E}{\delta \boldsymbol{l}}, \tag{1.10}$$

and the energy density $E(\boldsymbol{l},\boldsymbol{m}) = H(\boldsymbol{l},\boldsymbol{p})$. We will consider a diagonal anisotropy tensor with constant $\boldsymbol{K}$ and external field $\boldsymbol{B}$, making the total energy density

$$E(\boldsymbol{m}) = A(\boldsymbol{\nabla l})^2/2 + (\boldsymbol{m})^2/2\chi + \boldsymbol{K}(\hat{\boldsymbol{K}}\cdot\boldsymbol{l})^2/2 - \boldsymbol{b}\cdot\boldsymbol{m}, \tag{1.11}$$

where χ is the static transverse susceptibility. Going forward, we will use non-negative anisotropy constants, with the sign factored out explicitly.

Biaxial, two easy axes

In this section we consider two easy axes for the Néel order, with $K_1 > K_2$. The field is applied at an angle θ between $\boldsymbol{K_1}$ and the axis perpendicular to $\boldsymbol{K_1}$. The energy density is

$$E(\boldsymbol{l},\boldsymbol{m}) = A(\boldsymbol{\nabla l})^2/2 + \boldsymbol{m}^2/2\chi - K_1 l_z^2/2 - K_2 l_x^2/2 - b\boldsymbol{m}\cdot\hat{\theta}, \tag{1.12}$$

where when $\theta = 0$, $\boldsymbol{B}$ is along $\boldsymbol{K_1}$.

Collinear applied field. In easy-axis AFs, when the Zeeman energy due to an applied field along the easy axis exceeds the anisotropy energy, there is a metamagnetic phase transition called spin flop (SF). Below SF (state I), the Néel order aligns with the easy axis, and there is a small net magnetization due to remnant longitudinal magnetic susceptibility [10, 11]. Dynamically, there are two circularly-polarized spin-wave modes with opposite handedness. When quantized, they correspond to magnons with magnetic moment parallel or antiparallel to the order parameter [12]. Above SF (state II), the Néel order reorients into the hard plane, and the spins cant giving net magnetization along the easy axis, due to a sizeable transverse magnetic susceptibility. There are now two distinct spin-wave modes at long wavelengths: a ferromagnetic-like mode ($\omega \to \gamma B$ when applied field $B \to \infty$) and a low-energy Goldstone mode associated with the U(1)-symmetry breaking Néel orientation in the hard plane. See Fig. 1.1.

The ground states I and II are $(\boldsymbol{l}_0, \boldsymbol{m}_0)_{\rm I} = (\hat{\mathbf{z}}, 0)$ and $(\boldsymbol{l}_0, \boldsymbol{m}_0)_{\rm II} = (\hat{\mathbf{y}}, \chi b \hat{\mathbf{z}})$, with the critical field B_c marking the jump from I to II. Spin waves are linear excitations, $\boldsymbol{l} = \boldsymbol{l}_0 + \delta\boldsymbol{l}$ and $\boldsymbol{m} = \boldsymbol{m}_0 + \delta\boldsymbol{m}$, satisfying the equations of motion. The six Cartesian components of $\delta\boldsymbol{l}$ and $\delta\boldsymbol{m}$ reduce to four independent and two slave variables, after applying the nonlinear constraints. Correspondingly, there are four spin-wave modes with momentum k, as shown in Fig. 1.1 (for consistency of the gradient expansion, we require $k \ll a^{-1}$, the inverse lattice spacing). When $K_2 = 0$, ω_{1k} and ω_{2k} are waves with circularly precessing $\delta\boldsymbol{l}$ and $\delta\boldsymbol{m}$ in the plane perpendicular to $\boldsymbol{l}_{0,\rm I}$. ω_{3k} has linearly polarized $\delta\boldsymbol{l}(t) \propto e^{i\omega_{3k}t}\hat{\mathbf{x}}$ and $\delta\boldsymbol{m}(t) \propto (\omega_{3k}/\omega_x)e^{i(\omega_{3k}t-\pi/2)}\hat{\mathbf{z}}$. ω_{4k} has linearly polarized $\delta\boldsymbol{l}(t) \propto e^{i\omega_{4k}t}\hat{\mathbf{z}}$ and elliptically polarized $\delta\boldsymbol{m}(t) \propto (\omega_{4k}/\omega_x)e^{i\omega_{4k}t}\hat{\mathbf{x}} - \chi b e^{i(\omega_{3k}t-\pi/2)}\hat{\mathbf{y}}$, where $\omega_x \equiv 1/\chi s$. Adding K_2 slightly shifts the ground states, gaps ω_3, and introduces ellipticities in precession. When $k_B T \gg (\hbar/s)\sqrt{K_2/\chi}$, these modifications become negligible.

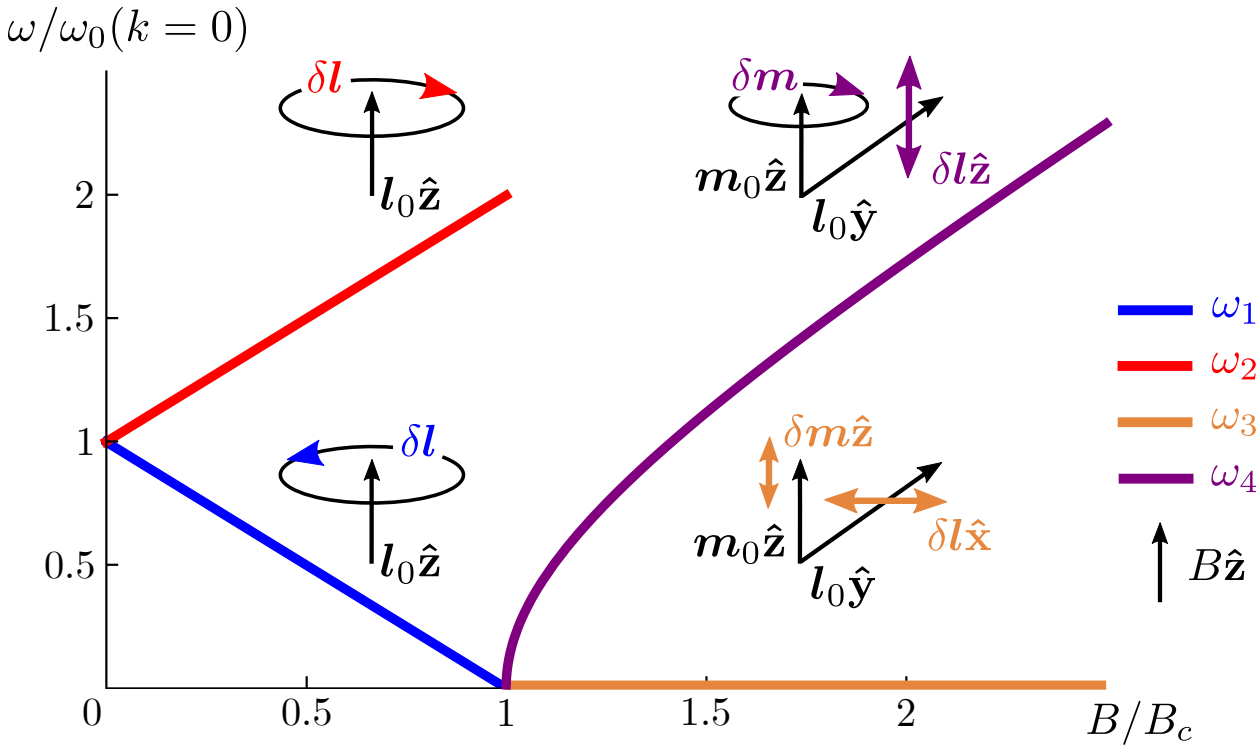

Figure 1.1: $k = 0$ resonance frequencies are plotted for an easy-axis AF: ω_1 and ω_2 below SF and ω_3 and ω_4 above SF. B is the magnetic field (absorbing the sign of γ), $B_c = (\gamma s)^{-1}\sqrt{K_1/\chi}$ is the spin-flop field according to the energy (1.12), and $\omega_0 = \gamma B_c$ is the gap in I. The ω_1 mode is right-hand and ω_2 is left-hand circularly polarized in $\delta\boldsymbol{l}$ and $\delta\boldsymbol{m}$ (however the magnitude of $\delta\boldsymbol{m}$ is a factor χK_1 smaller than $\delta\boldsymbol{l}$ below SF, so it is omitted from the Figure). ω_3 is linearly polarized in $\delta\boldsymbol{l}$ and $\delta\boldsymbol{m}$ so it does not produce spin currents. ω_4 is linearly polarized in $\delta\boldsymbol{l}$ and elliptically polarized in $\delta\boldsymbol{m}$.

The dispersions are

$$\omega_{1k}, \omega_{2k} = \mp\gamma B + \sqrt{(\gamma B_c)^2 + (ck)^2}, \tag{1.13a}$$

$$\omega_{3k} = ck, \quad \omega_{4k} = \sqrt{\gamma^2 B^2 - \gamma^2 B_c^2 + (ck)^2}, \tag{1.13b}$$

where $c = s^{-1}\sqrt{A/\chi}$ is the speed of the large-k AF spin waves. ω_{4k} is called the quasi-ferromagnetic (QFM) mode, because it is associated with circularly polarized precession of $\boldsymbol{\delta m}$ about $\boldsymbol{m_0}$. The decay rates below spin flop are

$$\epsilon_{ik} = \frac{2\omega_{ik}\omega_x}{\omega_{1k} + \omega_{2k}} \left[\alpha + \beta \left(\frac{|\delta \boldsymbol{m}_i|}{|\delta \boldsymbol{l}_i|}\right)^2\right] = \frac{2\omega_{ik}\omega_x}{\omega_{1k} + \omega_{2k}} \left(\alpha + \beta \frac{\omega_0^2}{\omega_x^2}\right), \tag{1.14}$$

giving Q-factor at $k = 0$

$$Q_{AF,I} = Q_1 = Q_2 = \frac{\omega_0}{\omega_x} \left(\alpha + \beta \frac{\omega_0^2}{\omega_x^2}\right)^{-1}. \tag{1.15}$$

Above spin flop the decay rates are

$$\epsilon_{ik} = \omega_x \left[\alpha + \beta \left(\frac{|\delta \boldsymbol{m}_i|}{|\delta \boldsymbol{l}_i|}\right)^2\right]. \tag{1.16}$$

Note that since ω_{4k} is independent of B it has zero field linewidth ΔB when $\theta = 0$, while ω_{3k} has nonzero ΔB. The Q-factor for the QFM mode at $k = 0$ is

$$Q_{AF,II-QFM} = \frac{\sqrt{B^2 - B_c^2}}{B_x} \left[\alpha + \beta \frac{B^2 - B_c^2}{B_x^2}\right]^{-1}. \tag{1.17}$$

Finally, we compare the easy-axis AF to the FM. For the lowest energy modes when $\beta \sim \alpha$ the β contributions become negligible so we discard them for comparison purposes. The field linewidths (as measured in resonance experiments) are defined as $\Delta B \equiv 2\epsilon(\partial\omega/\partial B)^{-1}$, which

at $k = 0$ are

$$\Delta B_{FM,k=0} = 2(B + K)\alpha, \tag{1.18a}$$

$$\Delta B_{AF,\mathrm{I},k=0} = 2(B_c - B)\frac{B_x}{B_c}\alpha, \tag{1.18b}$$

$$\Delta B_{AF,\mathrm{II},k=0} = 2\frac{B_x}{B}\sqrt{B^2 - B_c^2}\alpha, \tag{1.18c}$$

showing that the AF resonance linewidths are generally *exchange-enhanced*, leading to relatively smaller quality factors.

Noncollinear applied field. The solutions for general θ cannot be obtained analytically, so we compute the eigenvalues numerically and plot them in Fig. 1.2. In the limit $\theta \to 0$, our numerical and analytical results match.

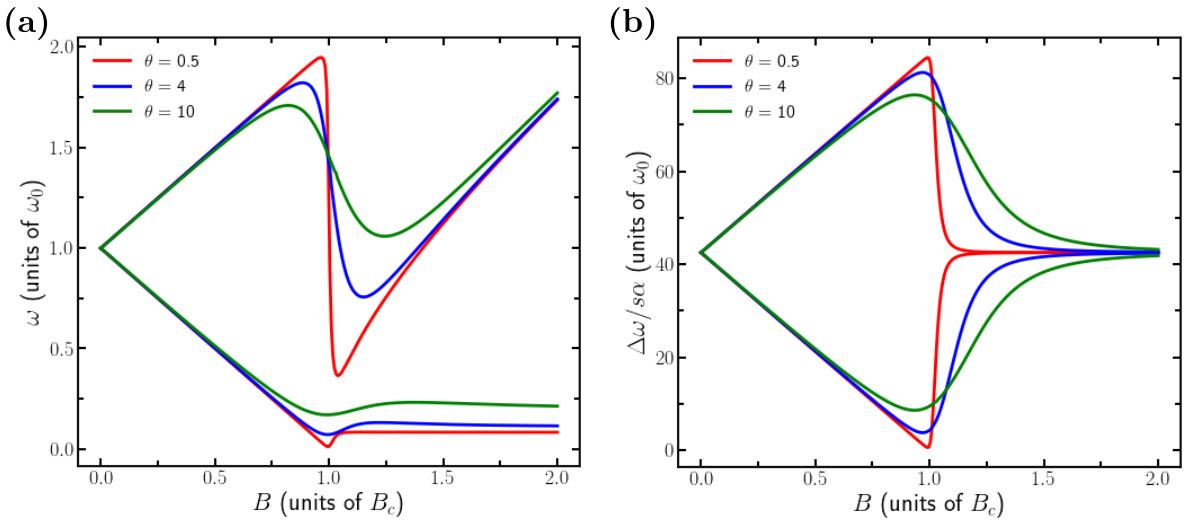

Figure 1.2: Real (a) and imaginary (b) parts of the eigenvalues at $k = 0$ from the AF equations of motion for various values of the angle θ between the applied field and easy axis.

Resonance dragging effect. Analogously to the FM, an uniaxial antiferromagnet also

exhibits a dragging effect. It is similar to the FM when $B < B_c$:

$$\Delta_{AF,I} B(\theta) = \frac{\Delta^{IB}\omega/\gamma + \alpha(B_c - B\cos\theta)}{\cos\theta}. \tag{1.19}$$

In the limit $B \ll B_c$, $\Delta_{AF,I} B(\theta) \approx C/\cos\theta$. As $B_z \equiv B\cos\theta$ increases above B_c, there is a steep climb of Δ^G. For example, this nonlinear dragging effect can be observed by tuning B_z to be slightly above B_c and increasing θ until the state returns to I.

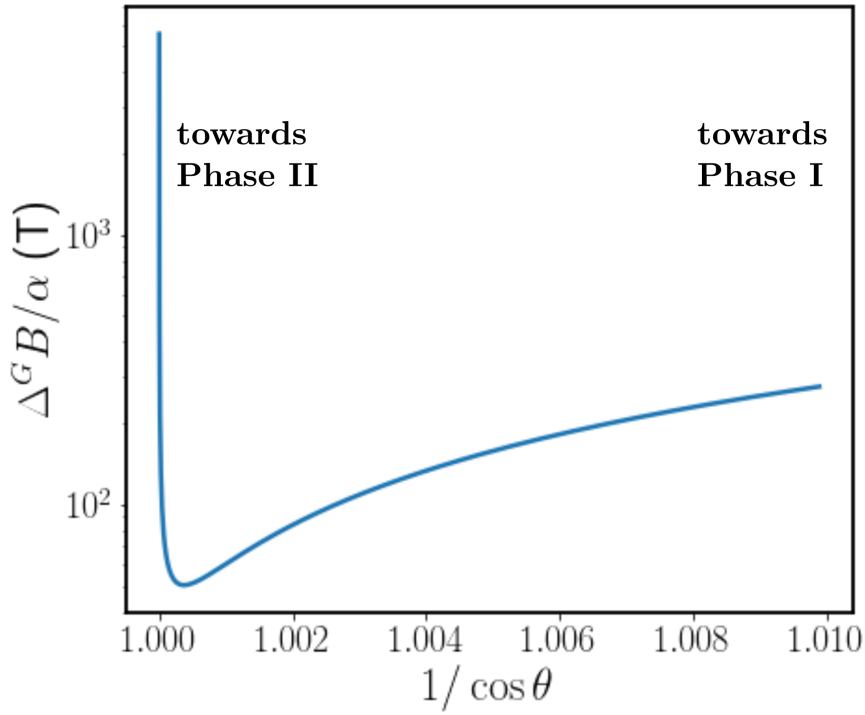

Figure 1.3: The nonlinear-dragging effect in the Gilbert field linewidth near spin-flop in an AF at $B = 1.03B_c$. For large θ, the state is below spin-flop with $\Delta^G B(\theta) \approx C/\cos\theta$ while as $\theta \to 0$ the state transitions to above spin-flop and $\Delta^G B(\theta)$ is sharply enhanced by both factors $\Delta^G\omega$ and $d\omega/dB$.

Biaxial, easy plane with easy axis within plane

We consider an easy-plane AF with an additional, weaker, easy axis within the plane. The field is applied within the easy plane, perpendicular to the second easy axis. Antisymmetric exchange is also allowed in crystals with broken inversion symmetry, but is not included here. The energy density is

$$E = \frac{\alpha^2}{2}|\boldsymbol{\nabla l}|^2 + \frac{1}{2\chi}|\boldsymbol{m}|^2 + \frac{K_1}{2}l_z^2 - \frac{K_2}{2}l_y^2 - b\hat{\boldsymbol{x}}\cdot\boldsymbol{m}, \tag{1.20}$$

where $K_1 > K_2$. We expand linearly about the ground state, subject to the nonlinear constraints. The constraint $\boldsymbol{l}^2 = 1$ sets $\delta l_y = 0$ and $\boldsymbol{l}\cdot\boldsymbol{m} = 0$ sets $\delta m_y = -m_0\delta l_x$. The solutions are linearly polarized spin waves; the low energy (when $B < B_c$) solution is

$$\boldsymbol{\delta L}_1(t) = \delta L_1 \cos(\omega_{1k}t)\hat{\boldsymbol{x}}, \tag{1.21a}$$

$$\boldsymbol{\delta M}_1(t) = \chi\omega_{1k}s_e\delta L_1 \cos(\omega_{1k}t + \pi/2)\hat{\boldsymbol{z}}, \tag{1.21b}$$

$$\omega_{1k} = \sqrt{(\gamma B)^2 + (\gamma B_{c2})^2 + c^2k^2}, \tag{1.21c}$$

where $B_{c2} = (\gamma s)^{-1}\sqrt{K_2/\chi}$, and the high energy solution is

$$\boldsymbol{\delta L}_2(t) = \delta L_2 \cos(\omega_{2k}t)\hat{\boldsymbol{z}}, \tag{1.22a}$$

$$\boldsymbol{\delta M}_2(t) = \chi\omega_2 s_e\delta L_2 \cos(\omega_{2k}t - \pi/2)\hat{\boldsymbol{x}}, \tag{1.22b}$$

$$\omega_{2k} = \sqrt{(\gamma B_c)^2 + c^2k^2}. \tag{1.22c}$$

1.1.3 Nuclear-spin-hybridized antiferromagnets

Nuclear spin waves were discovered theoretically in FMs by Suhl [13] and in AFs by Nakamura [14]. Nakamura demonstrated that the hyperfine interaction (HFI) between nuclei and electrons leads to indirect coupling between nuclei via applying the Holstein-Primakoff transformation to both nuclear and electronic spins. The coupled spectra in AFs was later derived by DeGennes [15] using a Landau-Lifshitz type of approach for the AF sublattice magnetization [16]. Here, we cast DeGennes' theory into the more modern formalism which describes AFs by directional Néel order $\boldsymbol{L}$ and normalized spin density $\boldsymbol{M} = \mathbf{s}_m/s_m$ with the nonlinear σ-model constraint $\boldsymbol{L}^2 = 1$ and sublattice symmetry, $\boldsymbol{L} \cdot \boldsymbol{M} = 0$. Since the nuclei are coupled to electrons, they are described on the same footing by similarly defined $\boldsymbol{l}$ and $\boldsymbol{m}$ with $\boldsymbol{l} \cdot \boldsymbol{m} = 0$. Here $s_m = s_m/V$ and $s_n = S_n/V$ are the saturated electronic and nuclear volume spin densities in units of $\hbar$. Nuclear spin dynamics are described by the Bloch equations [17]. For a thorough, historically-based account of nuclear-magnon hybridization and research, see Ref. [18].

The nuclear spins are coupled to the electronic spins through the (local on-site) hyperfine interaction [19, 20]. At low temperatures, the nuclear spins become weakly polarized antiparallel to the local electronic spins. It also introduces a dynamic coupling between the nuclear and electronic systems. We expect the coupling to be substantial when the nuclear and electronic resonant frequencies are within 1-2 orders of magnitude of one another. Nuclear static resonant frequencies are tens - hundreds of MHz, so coupling occurs at low temperatures in FMs, easy-plane AFs, and possibly–although this has yet to be researched–easy-axis AFs near spin-flop). In this investigation, we analyze nuclear coupling to an easy-plane AF.

Labeling the lattice sites 1 and 2, and (normalized) nuclear/electronic sublattice spin

density $\boldsymbol{m_i}, \boldsymbol{M_i}$, the hyperfine interaction is

$$E_{hf} = A\left(\boldsymbol{m_1}\cdot\boldsymbol{M_1} + \boldsymbol{m_2}\cdot\boldsymbol{M_2}\right), \tag{1.23}$$

where A is an energy density and favors antialigned spins. Rewriting both in terms of Néel order and spin density,

$$E_{hf} = \frac{A}{2}\left(\boldsymbol{L}\cdot\boldsymbol{l} + \boldsymbol{M}\cdot\boldsymbol{m}\right). \tag{1.24}$$

The total energy density is $E = E_{hf} + E_{EPAF} + E_Z$, where E_{EPAF} is given by Eq. 1.20 and E_Z is the nuclear Zeeman coupling. For nuclear spin density s_n (defined in terms of zero-temperature saturation magnetization m_s, $s_n = m_s/\gamma_n$), the undamped Bloch equations are

$$s_n\frac{\partial \boldsymbol{l}}{\partial t} = -\boldsymbol{H}_m\times\boldsymbol{l} - \boldsymbol{H}_l\times\boldsymbol{m}, \tag{1.25a}$$
$$s_n\frac{\partial \boldsymbol{m}}{\partial t} = -\boldsymbol{H}_m\times\boldsymbol{m} - \boldsymbol{H}_l\times\boldsymbol{l}, \tag{1.25b}$$

with effective fields $\boldsymbol{H}_i \equiv -\delta E/\delta\boldsymbol{q_i}$ for the variable $\boldsymbol{q_i}$. The Bloch equations inherently conserve spin lengths.

Ground state

To calculate the nuclear equilibrium polarization, we balance the entropy and Zeeman energy in the standard Curie's Law calculation. For N nuclear spins polarized along $\hat{\boldsymbol{z}}$, the normalized nuclear paramagnetic moment is

$$\langle m_z\rangle \approx \frac{\hbar\omega_n}{k_BT} + \mathrm{C}\left(\frac{\hbar\omega_n}{k_BT}\right)^3 + \cdots \equiv \chi_n H_0 \tag{1.26}$$

where $H_0\hat{\boldsymbol{z}}$ is the (normalized) local field at each nuclear site for χ_n in units of volume/energy. In the presence of the AF Néel ordering, $H_0 = A + s_n\gamma_n B$, known as the Overhauser field [21, 22], and we will approximate the Brillouin function to leading order in $\hbar\omega_n \ll k_B T$. For example in the nuclear magnet $MnCO_3$, $\omega_n = 660$MHz which corresponds to $T = 50$ mK (additionally, near 50 mK the nuclear spins are theorized to undergo a spin-ordering phase transition in this material [23]; however, we will stay at temperatures above this regime). This defines the (normalized) static nuclear spin susceptibility, χ_n. Switching to the staggered and spin density, we have

$$\boldsymbol{l_0} = \chi_n \frac{A}{2} \boldsymbol{L_0} \tag{1.27a}$$

$$\boldsymbol{m_0} = \chi_n (\frac{A}{2} \boldsymbol{M_0} + s_n \gamma_n \boldsymbol{B}) \tag{1.27b}$$

System of approximations

The previously-obtained solutions to this system rely on a system of approximations which account for the relative strengths of the exchange and hyperfine interactions and the weak relative magnetic coupling strength γ_n/γ_m of the nuclear spins. To compare these interactions, we express the couplings in terms of effective fields. These are the exchange field $B_x \equiv (\gamma_e s_m \chi)^{-1}$, the hyperfine field $B_A \equiv (\gamma_n s_n)^{-1} A/2$, and the crystalline anisotropy (within easy plane) field, $B_{c2} \equiv (\gamma s)^{-1}(K_2/\chi)^{1/2}$. The hyperfine field is the field experienced by each nuclear spin due to an electron on the same site.

In the well known nuclear magnet $MnCO_3$, $B_x = 68$T, $B_A = 57$T, $B_{c2} \approx 0.01$T. Since we will compare our theory to spin transport data on $MnCO_3$ in Chapter 4, we develop our system of approximations with these values in mind. In the equations of motion, we will neglect the following terms (and higher orders) with respect to unity: $(B/B_x)^2, (B/B_A)^2$.

Finally, there is an additional small dimensionless quantity reflecting the smaller nuclear static susceptibility: $\chi_n/\chi \propto \gamma_n/\gamma_m$, which appears in the equations of motion. We retain the largest term containing this factor, which turns out to be $B_A^2\chi_n/\chi \equiv B_\Delta^2(T)$. This is called the nuclear pulling field, sometimes written as a phenomenological effective anisotropy field within the easy plane and defined differently as $B_x B_\Delta(T)$. Here, we have derived this field analytically. *The nuclear pulling field is the exchange-enhanced field experienced by an electron due to a nuclear spin (which is already polarized by the electron's field) on the same site.* It is a second-order effect of the hyperfine coupling, expanded perturbatively with respect to the electronic exchange coupling. We also neglect $(B_\Delta/B_x)^2, (B_\Delta/B_A)^2$, but retain $(B_\Delta/B)^2$.

Spin wave spectra

We expand linearly about the electronic and nuclear ground states. As guaranteed by the Bloch equations, the individual nuclear spin lengths are conserved, so $\boldsymbol{m}_1^2 = \boldsymbol{m}_2^2$ is fixed. To linear order in $\boldsymbol{\delta m}$, we have $\delta m_{1y} = -M_0 \delta m_{1x}$ and $\delta m_{2y} = M_0 \delta m_{x2}$. Equivalently, $\delta m_y = -M_0 \delta l_x$ and $\delta l_y = -M_0 \delta m_x$. Hence, our set of dynamical coordinates is expanded from 4 to 8 coordinates. We arbitrarily select $\{\delta L_x, \delta L_z, \delta M_x, \delta M_z, \delta l_x, \delta l_z, \delta m_x, \delta m_z\}$. By decomposing the equations of motion into matrix form, we observe that the coordinates decouple into two systems, as was the case without nuclear coupling. One system, $\{\delta L_z, \delta M_x, \delta l_z, \delta m_x\}$, has an eigenfrequency near the high energy electronic frequency ω_2, and the other system, $\{\delta L_x, \delta M_z, \delta l_x, \delta m_z\}$, has an eigenfrequency near the low energy electronic frequency, ω_1. Each subsystem also has a pulled nuclear eigenfrequency ω_n, but the pulling is more substantial in the low energy subsystem.

As mentioned in the section of easy-plane AFs, there are two spin wave modes associated with rotation of the Néel order either out of or within the easy-plane. The hybridized low-

energy modes are

$$\omega_{mk} = \sqrt{\omega_{1k}^2 + \gamma_m^2 B_\Delta^2} \tag{1.28}$$

$$= \sqrt{\gamma_m^2 (B_{c2}^2 + B^2 + B_\Delta^2) + c^2 k^2}$$

$$\omega_{nk} = \omega_n \sqrt{1 - \gamma_m^2 B_\Delta^2 / \omega_{mk}^2} \tag{1.29}$$

where $B_\Delta^2 = (\hbar\omega_n / k_B T) B_A B_x \gamma_n / \gamma_m$ with $B_A = A/\gamma_n s_n$ and $B_x = (\chi \gamma_m s_m)^{-1}$, and γ_n, γ_m are the nuclear and magnonic gyromagnetic ratios. The low-energy modes in Eq. (1.13) have elliptically precessing spin-density and linearly-polarized Néel order excitations.

Nuclear-magnon hybridized resonance frequencies

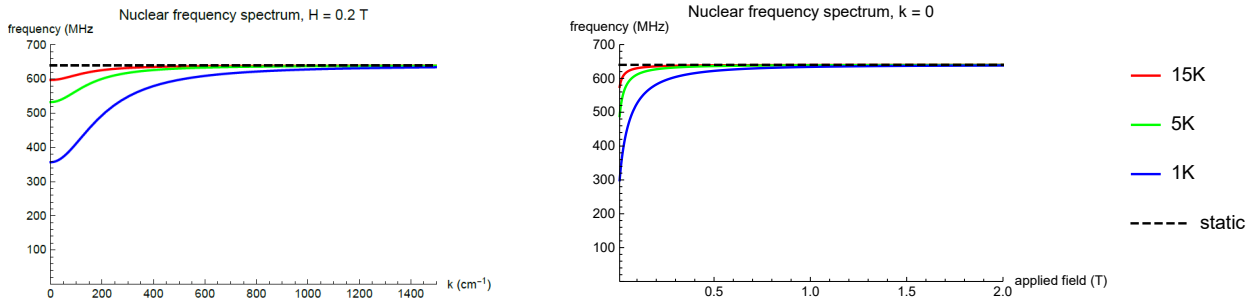

(a) ω_n at $k = 0$ as a function of applied field. (b) ω_n at $B = 0.2T$ as a function of momentum.

Figure 1.4: Example of nuclear pulled frequencies in the nuclear magnet $MnCO_3$.

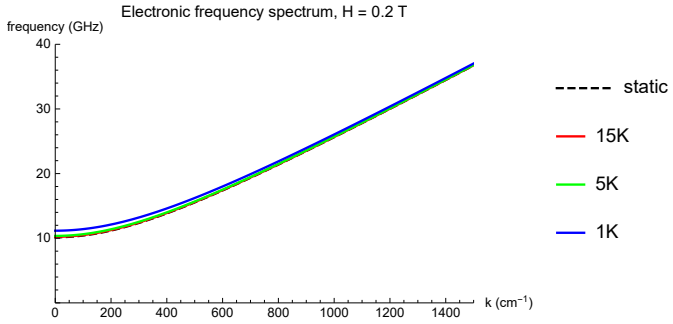

Figure 1.5: Example of shifted magnon frequencies in the nuclear magnet $MnCO_3$ at $B = 0.2T$ as a function of momentum.

1.2 Schwinger boson mean-field theory

The Schwinger boson transformation is an exact transformation which replaces the spin operators by a product of bosonic creation and annihilation operators,

$$S^+ = a_\uparrow^\dagger a_\downarrow, \tag{1.30a}$$

$$S^- = a_\downarrow^\dagger a_\uparrow, \tag{1.30b}$$

$$S^z = \sum_\sigma \sigma a_\sigma^\dagger a_\sigma/2, \tag{1.30c}$$

$$S = \sum_\sigma a_\sigma^\dagger a_\sigma/2, \tag{1.30d}$$

where $\sigma = \pm$ and the operators obey bosonic commutation relations, $\left[a_\sigma, a_{\sigma'}^\dagger\right] = \delta_{\sigma\sigma'}$. Eq. (1.30d) is the constraint which fixes the spin length on each site. In terms of Schwinger bosons, the nearest-neighbor Heisenberg Hamiltonian on a bipartite lattice written in terms of SBs a_σ and b_σ for sublattices $\mathcal{A}$ and $\mathcal{B}$, respectively, reads

$$H = -J\sum_{\langle ij\rangle} \mathbf{S}_i \cdot \mathbf{S}_j = -2J\sum_{\langle ij\rangle} \left[\alpha : F_{ij}^\dagger F_{ij} : -(1-\alpha) A_{ij}^\dagger A_{ij}\right] - \sum_{i\sigma} \lambda_i (a_{i\sigma}^\dagger a_{i\sigma} - 2S). \tag{1.31}$$

Here, summing over $\langle ij\rangle$ avoids double counting, $F_{ij} = \sum_\sigma a_{i\sigma}^\dagger b_{j\sigma}/2$, $A_{ij} = \sum_\sigma \sigma a_{i\sigma} b_{j\bar{\sigma}}/2$, and λ_i is the Lagrange multiplier which implements the constraint on the ith site. Since the Hamiltonian written in terms of SBs contains terms which are quartic in the field operators, it must be decoupled by a Hubbard-Stratonovich transformation [6]. In this thesis, we pursue a mean-field theory (neglecting fluctuations beyond the saddle point), in the interest of performing a preliminary investigation into the spin excitations and spin transport at arbitrary temperatures in Heisenberg FMs, AFs, and PMs.

Generally, one should include all terms in their mean-field decomposition, except those that may be ruled out by symmetry considerations. In magnets, U(1)-symmetry is broken

spontaneously in the ordered phase. However, the SU(2)-preserving SBMFT decomposition is the standard used throughout the field of SB research, including in ordered magnets, e.g. [5, 24, 25, 26, 27, 28]. Without SU(2)-breaking terms in the mean-field decomposition, the symmetry in the ordered phase most be broken explicitly by an infinitesimal applied field. Additionally, disordered magnets in the presence of applied fields are known to obey the Curie-Weiss law, which arises from a U(1)-symmetric effective field felt by a spin due to the weak polarization of neighboring spins. Thus, when performing our SB mean-field decomposition of the Heisenberg Hamiltonian, we should attempt to consider all terms which respect U(1) symmetry. The most general (Hartree-Fock-Bogoliubov) U(1)-preserving mean-field decomposition of the nearest-neighbor Heisenberg Hamilitonian on a bipartite lattice, is

$$H_{\rm mf} = H_{\rm mf}^{SU(2)} + H_{\rm mf}^{U(1)}, \tag{1.32a}$$

$$H_{\rm mf}^{SU(2)} = -2J\sum_{\langle ij\rangle}\Big[\alpha F_{ij}^\dagger F - (1-\alpha)A_{ij}^\dagger A + \text{H.c.}\Big] - \mu_{\mathcal{A}}\sum_{i\in\mathcal{A},\sigma} a_{i\sigma}^\dagger a_{i\sigma} - \mu_{\mathcal{B}}\sum_{i\in\mathcal{B},\sigma} b_{i\sigma}^\dagger b_{i\sigma}, \tag{1.32b}$$

$$H_{\rm mf}^{U(1)} = -JZ\left(\sum_{i\in\mathcal{A}} S_{\mathcal{B}}^z S_i^z + \sum_{i\in\mathcal{B}} S_{\mathcal{A}}^z S_i^z\right) - 2J\sum_{\langle ij\rangle,\sigma}\Big[\alpha C_{ij,\sigma}^\dagger C_{\bar\sigma} - (1-\alpha)D_{ij,\sigma}^\dagger D_{\bar\sigma} + \text{H.c.}\Big]. \tag{1.32c}$$

Here, summing over $\langle ij\rangle$ avoids double counting, $F_{ij} = \sum_\sigma a_{i\sigma}^\dagger b_{j\sigma}/2$, $A_{ij} = \sum_\sigma \sigma a_{i\sigma} b_{j\bar\sigma}/2$, $C_{ij,\sigma} = a_{i\sigma} b_{j\bar\sigma}$ and $D_{ij,\sigma} = a_{i\sigma}^\dagger b_{j\sigma}$. The mean-fields are $F = \langle F_{ij}\rangle$ and similarly for A, C, D, $S_{\mathcal{A}(\mathcal{B})}^z$ is the mean z-component of spin on the $\mathcal{A}(\mathcal{B})$ sublattice, and $JZS_{\mathcal{A}(\mathcal{B})}^z$ is the effective field which yields the Curie-Weiss law for Z nearest neighbors. The quartic terms in Eq. (1.31) are approximated in our MF decomposition by the product of a quadratic term and the mean-fields, and in the same spirit the spin length constraints are implemented via two aggregate Lagrange multipliers $\mu_{\mathcal{A}(\mathcal{B})}$. This decomposition applies to isotropic lattice models where there is a single F and single A parameter. Note that while the exact con-

straint fixes the sum of the SB species' number operators on each site, $\mu_{\mathcal{A}(\mathcal{B})}$ instead fix the expectation value of this operator sum on each sublattice. In deriving Eq. (1.32a) we made use of the identities [5, 6] (where $: \ldots :$ is normal ordering)

$$: F_{ij}^{\dagger} F_{ij} := F_{ij}^{\dagger} F_{ij} - S, \tag{1.33a}$$

$$: F_{ij}^{\dagger} F_{ij} : + A_{ij}^{\dagger} A_{ij} = S^2, \tag{1.33b}$$

which can in turn be derived, respectively, by inserting the constraint once or twice into $: F_{ij}^{\dagger} F_{ij} :$. α is a parameter that is free to vary in the exact Hamiltonian, but parameterizes separate mean-field Hamiltonians [29, 6]. To fix α, we match the poles of the dynamic susceptibilities to the Holstein-Primakoff result at $T = 0$, giving the usual [5] $\alpha = 1$ for the FM and $\alpha = 0$ for the AF, and for simplicity fix these values for α at all T.

As we will see, the solutions to the SU(2) problem are consistent with $C = D = 0$, but the effective field $JZS^z_{\mathcal{A}(\mathcal{B})}$ is generally finite in the ordered phase, or when SU(2) symmetry is broken by an applied field in the disordered phase. Therefore, we do not have a reason *a priori* to discard it. Starting from $T = \infty$, we find a gaseous paramagnetic phase with $F = A = 0$ that survives at finite temperatures down to the liquid-gas transition. In the gaseous phase, the susceptibility follows the Curie-Weiss law. This U(1) term also provides spontaneous symmetry breaking at the Curie/Néel transition. However, it introduces a magnon gap in the ordered phase, where we expect gapless Goldstone modes in the Heisenberg FM and AF, and results in first-order Curie and Néel transitions. There is an indication that the issues may be resolved, for example, by taking the full U(1) decomposition for a given α in Eq.(1.32a). When we take $\alpha = 1$ at $T \ll T_C$ and consider both $F \neq 0$ and $C_\sigma \neq 0$, we find a low-T solution which restores the Bloch law. However, since this significantly increases the complexity of the MF equations and is not within the scope of this work, we do not consider finite C and D in detail, and instead call for future investigations into a more complete SBMFT in the ordered phase. The effect of treating α as a separate mean-field parameter is

also an open question, though Ref. [30] used it as a fitting parameter to reproduce data on the dynamical spin structure factor of a $S = 1/2$ triangular lattice antiferromagnet, obtaining $\alpha = 0.436$.

In this thesis, we present SBMFT solutions to the SU(2)-symmetric decomposition of the Heisenberg FM, uniaxial AF below spin flop, and PM, for infinitesimal applied fields. In these systems, infinitesimal fields are sufficient for generating interfacial spin transport, which is our main research objective. In total, the bipartite FM (uniaxial AF below spin flop) has three mean-field parameters: F (A), $\mu \equiv (\mu_{\mathcal{A}} + \mu_{\mathcal{B}})/2$, and $\delta\mu \equiv (\mu_{\mathcal{A}} - \mu_{\mathcal{B}})/2$. Additionally, we will include the U(1) effective fields $JZS^z_{\mathcal{A}(\mathcal{B})}$ for the $\mathcal{A}(\mathcal{B})$ sublattices in the high-temperature limit of Heisenberg PMs to demonstrate this, fully self-consistent, decomposition does yield the expected Curie-Weiss law. In Chapter 4, we will show that these U(1) terms are essential for explaining recent spin transport experiments in paramagnetic materials.

1.2.1 Heisenberg ferromagnet

Here, we consider ferromagnetic exchange in the SU(2)-symmetric MF decomposition with $\alpha = 1$, and take a uniform chemical potential $\mu_{\mathcal{A}} = \mu_{\mathcal{B}}$.

Cubic lattices

For cubic lattices (simple cubic, bcc, fcc), the unit cell contains a single SB operator a_σ, so $F_{ij} = 1/2(a^\dagger_{i\uparrow}a_{j\uparrow} + a^\dagger_{i\downarrow}a_{j\downarrow})$. The MF Hamiltonian is

$$\begin{aligned} H_{mf} &= -2JF\sum_{ij}\left[F_{ij} + F^\dagger_{ij}\right] - \lambda\sum_{i\sigma} a^\dagger_{i\sigma}a_{i\sigma} - \hbar\gamma B\sum_{i\sigma} s_\sigma a^\dagger_{i\sigma}a_{i\sigma} \\ &= \sum_{\boldsymbol{k}\sigma}(\epsilon_{\boldsymbol{k}\sigma} - \mu)a^\dagger_{\boldsymbol{k}\sigma}a_{\boldsymbol{k}\sigma}, \end{aligned} \tag{1.34a}$$

where in the second line we assumed isotropic mean-fields, $F \equiv \langle F_{ij}\rangle = \langle F_{ji}\rangle$ (also noting that $F^\dagger_{ij} = F_{ji}$), and we defined $\mu \equiv JFZ + \lambda$. There are two bands whose energies, in the presence of magnetic field $B\hat{\boldsymbol{z}}$, are

$$\epsilon_{\boldsymbol{k}\sigma} = JFZ(1 - \gamma_{\boldsymbol{k}}) - \hbar\gamma B s_\sigma, \tag{1.35}$$

with structure factor $\gamma_{\boldsymbol{k}} \equiv Z^{-1}\sum_{\boldsymbol{\delta}} \cos \boldsymbol{k}\cdot\boldsymbol{\delta}$ where Z is the number of nearest neighbors. At arbitrary temperatures, the self-consistent mean-field equations for F and S give the solutions to $F(T)$ and either the condensate density $n_c(T)$ or $\mu(T)$ according to

$$F = (2N)^{-1}\sum_{\boldsymbol{k}\sigma} n_{\boldsymbol{k}\sigma}\gamma_{\boldsymbol{k}} = S - (2N)^{-1}\sum_{\boldsymbol{k}\sigma} n_{\boldsymbol{k}\sigma}(1 - \gamma_{\boldsymbol{k}}), \tag{1.36a}$$

$$S = (2N)^{-1}\sum_{\boldsymbol{k}\sigma} n_{\boldsymbol{k}\sigma}, \tag{1.36b}$$

where N is the number of sites arising from the normalization factor in the Fourier transform: $a_i = \sum_{\boldsymbol{k}} e^{-i\boldsymbol{k}\cdot\boldsymbol{r_i}}a_{\boldsymbol{k}}/\sqrt{N}$. If μ reaches $-b/2$ there are zero-energy modes at $\boldsymbol{k} = 0$ that condense with density $n_c \equiv N_c/N$. Then at $T \le T_C$, $\mu(T)$ is fixed and we instead solve for $n_c(T)$, or equivalently at $B = 0$, $S^z(T) = n_c/2$. The numerical mean-field solutions on the cubic lattices have first-order Curie transitions, as shown in Fig. 1.6. However, the diamond transition turns out to be second-order for $S = 1/2$, as discussed in the next section.

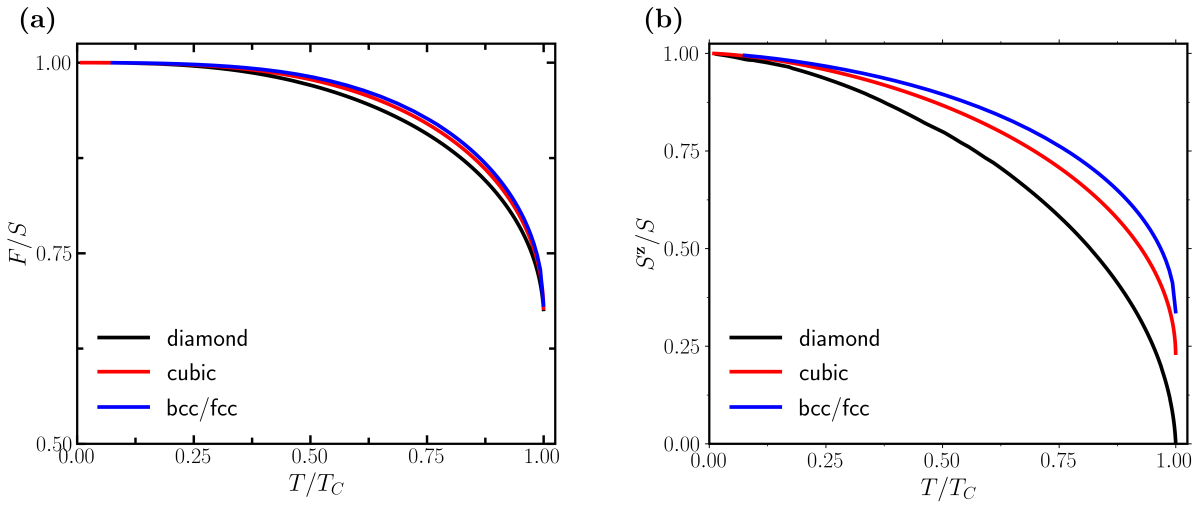

Figure 1.6: Numerical mean-field solutions for the FM with $S = 1/2$ at $B = 0$ and $T < T_C$. T for each lattice is in units of its respective T_C. (a) Numerical solutions to $F(T)$. (b) Numerical solutions to $S^z(T)$ (equivalent to the condensate density at $B = 0$).

Diamond lattice

The following section will be published in Ref. [31]. The SU(2)-preserving MFT yields a first-order Curie transition on cubic Bravais lattices, but is second-order on the diamond lattice, possibly due to its higher-order connectivity [32]. The FM mean-field Hamiltonian plus applied field on the diamond lattice, setting $\delta\mu = 0$, after Fourier transforming and casting in terms of sublattice pseudospin, $\psi_{\boldsymbol{k}\sigma} = (a_{\boldsymbol{k}\sigma}, b_{\boldsymbol{k}\sigma})$, is

$$H_{\mathrm{mf}}^{\mathrm{FM}} = \sum_{\boldsymbol{k}\sigma} \psi_{\boldsymbol{k}\sigma}^{\dagger} \left[-(\mu + b\sigma/2) + \boldsymbol{\eta}_{\boldsymbol{k}} \cdot \boldsymbol{\tau} \right] \psi_{\boldsymbol{k}\sigma}, \tag{1.37}$$

where $b \equiv \hbar\gamma B$, $\boldsymbol{\eta}_{\boldsymbol{k}} = (-JF \operatorname{Re}\gamma_{\boldsymbol{k}}, JF \operatorname{Im}\gamma_{\boldsymbol{k}}, 0)$, $\gamma_{\boldsymbol{k}} = Z^{-1} \sum_{\boldsymbol{\delta}} e^{i\boldsymbol{k}\cdot\boldsymbol{\delta}}$ is the structure factor and $\boldsymbol{\delta}$ is the vector between nearest neighbors on sublattice $\mathcal{A}$ to $\mathcal{B}$, and $\boldsymbol{\tau}$ is the vector of Pauli matrices. There are four bands with energies

$$\epsilon_{\boldsymbol{k}\sigma}^{\pm} = JZF(1 \pm |\gamma_{\boldsymbol{k}}|) - (\mu + b\sigma/2), \tag{1.38}$$

where a factor of JZF was absorbed into the definition of μ. The eigenvectors are $v^{\pm}_{\boldsymbol{k}\sigma} = (1, \mp|\gamma_{\boldsymbol{k}}|/\gamma_{\boldsymbol{k}})/\sqrt{2}$. If μ reaches $-b/2$ the lowest energy branch, $\epsilon^{-}_{\boldsymbol{k}\uparrow}$, has zero-energy modes that condense, resulting in long-ranged spin ordering along the $+\hat{\boldsymbol{z}}$ axis in the language of SBs [5, 33]. At arbitrary temperatures, the self-consistent mean-field equations for F and S give the solutions to $F(T)$ and either the condensate density $n_c(T)$ or $\mu(T)$ according to

$$F = -(4N)^{-1} \sum_{\boldsymbol{k}\sigma\lambda} n^{\lambda}_{\boldsymbol{k}\sigma} \lambda |\gamma_{\boldsymbol{k}}|, \tag{1.39}$$

$$S = (4N)^{-1} \sum_{\boldsymbol{k}\sigma\lambda} n^{\lambda}_{\boldsymbol{k}\sigma}, \tag{1.40}$$

where $n^{\lambda}_{\boldsymbol{k}\sigma}$ is the Bose-Einstein distribution function for energy $\epsilon^{\lambda}_{\boldsymbol{k}\sigma}$, and N is the number of sites per sublattice. In order to solve Eqs. (1.36) at $T < T_N$, the sums are converted to integrals with the contributions from the condensate density separated explicitly: for an arbitrary function z and a single condensation point at momentum $\boldsymbol{k_c}$, $\sum_{\boldsymbol{k}} z_{\boldsymbol{k}}/N \approx z(\boldsymbol{k_c})N_c/N + \mathcal{V}\int_{\mathrm{BZ}} d^3\boldsymbol{k}\; z(\boldsymbol{k})$, where $n_c \equiv N_c/N$ and $\mathcal{V}$ is the unit cell volume. The complete numerical solutions of the MFT for $B = 0$ with $S = 1/2$ for the FM, where $n_c \propto S^z$ are plotted in Fig. 1.7 ($T_C = 0.633J$ and $T_N = 5.12J$ in units where the Boltzmann constant $k_B = 1$).

1.2.2 Easy-axis antiferromagnet below spin flop

The following section will be published in Ref. [31]. On the other hand, we find the Néel transition is second-order on all cubic Bravais lattices, so we take the simple cubic lattice for simplicity. The AF mean-field Hamiltonian with easy-axis anisotropy constant K plus

collinear applied field is

$$H_{\rm mf}^{\rm AF} = \sum_{\boldsymbol{k}\sigma} \psi_{\boldsymbol{k}\sigma}^{\dagger} \left[\zeta_\sigma - (\delta\mu + b\sigma/2)\tau_z\right] \psi_{\boldsymbol{k}\sigma} + \sum_{\boldsymbol{k}\sigma} (i\sigma\psi_{\boldsymbol{k}\sigma}^{\intercal} \boldsymbol{\eta}_{\boldsymbol{k}} \cdot \boldsymbol{\tau} \psi_{-\boldsymbol{k}\bar{\sigma}}/2 + \text{H.c.}), \quad (1.41)$$

where we consider $b \ll \sqrt{JK}$, the spin-flop field; here $\zeta_\sigma = -\mu - KL^z\sigma/2$ for mean staggered spin polarization $L^z = (S_{\mathcal{A}}^z - S_{\mathcal{B}}^z)/2$, $\boldsymbol{\eta}_{\boldsymbol{k}} = (JA\,\mathrm{Im}\,\gamma_{\boldsymbol{k}}, JA\,\mathrm{Re}\,\gamma_{\boldsymbol{k}}, 0)$, and $\psi^{\intercal}$ is the vector transpose. Diagonalizing the Hamiltonian via a Bogoliubov transformation for each σ yields four bands, we get energies

$$\epsilon_{\boldsymbol{k}\sigma}^{+} = -\delta\mu - b\sigma/2 + \epsilon_{\boldsymbol{k}\sigma},\ \epsilon_{\boldsymbol{k}\sigma}^{-} = \delta\mu - b\sigma/2 + \epsilon_{\boldsymbol{k}\bar{\sigma}}, \quad (1.42)$$
$$\epsilon_{\boldsymbol{k}\sigma} \equiv \sqrt{\zeta_\sigma(2JZA + \zeta_\sigma) + (JZA)^2(1 - \gamma_{\boldsymbol{k}}^2)},$$

where, like for the FM, we shifted μ by a factor of JZA, and $\overline{\sigma} = -\sigma$. Here, the ansatz $\delta\mu = -b/2$ was found by matching $\epsilon_{\boldsymbol{k}\downarrow}^{+}$ and $\epsilon_{\boldsymbol{k}\uparrow}^{-}$ to the usual AF magnon modes from HPA, which turns out to be the self-consistent solution for $\delta\mu$ at all T. Analogously to the FM, BEC occurs when the lowest-energy modes of $\epsilon_{\uparrow}^{+}$ and $\epsilon_{\downarrow}^{-}$ become gapless at $\mu = -KL^z/2$, so that $\zeta_\sigma = KL^z(1-\sigma)/2$ [26], resulting in long-ranged staggered ordering. The equations for $T < T_N$ are obtained by eliminating $n_c(T)$ to give two independent equations for $A(T)$ and $L^z(T)$.

The Bogoliubov transformation (very similar to, c.f. Ref. [34], the usual Bogoliubov transformation for AF magnons in the Holstein-Primakoff approximation; specifically, when $\sigma = \downarrow$, our transformation matches the structure of the magnonic one) that diagonalizes the AF Heisenberg Hamiltonian after a SU(2)-symmetric mean-field decomposition, plus uniaxial

anisotropy and collinear applied field below spin flop, is

$$(a_{\boldsymbol{k}\sigma}, b_{-\boldsymbol{k}\bar{\sigma}}) = u_{\boldsymbol{k}\sigma}\Psi_{\boldsymbol{k}\sigma} + \sigma v_{\boldsymbol{k}\sigma}\tau_x\Psi^{\dagger}_{\boldsymbol{k}\sigma}, \tag{1.43a}$$

$$u^2_{\boldsymbol{k}\sigma} = \frac{1}{2}\left[\frac{2\zeta_\sigma + 2JZA}{\epsilon^+_{\boldsymbol{k}\sigma} + \epsilon^-_{\boldsymbol{k}\bar{\sigma}}} + 1\right], \tag{1.43b}$$

$$v^2_{\boldsymbol{k}\sigma} = \frac{1}{2}\left[\frac{2\zeta_\sigma + 2JZA}{\epsilon^+_{\boldsymbol{k}\sigma} + \epsilon^-_{\boldsymbol{k}\bar{\sigma}}} - 1\right], \tag{1.43c}$$

where τ_x is the pauli matrix, $\zeta_\sigma \equiv -\mu - KL^z\sigma/2$, $\Psi_{\boldsymbol{k}\sigma} \equiv (\alpha_{\boldsymbol{k}\sigma}, \beta_{-\boldsymbol{k}\sigma})$ and α, β are the Bogoliubon field operators whose energies are $\epsilon^+_{\boldsymbol{k}\sigma}, \epsilon^-_{\boldsymbol{k}\sigma}$, respectively.

General mean-field equations

The mean-field equations are

$$A = \frac{1}{2N}\sum_{\boldsymbol{k}\sigma}\gamma_{\boldsymbol{k}}(n^+_{\boldsymbol{k}\sigma} + n^-_{\boldsymbol{k}\bar{\sigma}} + 1)u_{\boldsymbol{k}\sigma}v_{\boldsymbol{k}\sigma}, \tag{1.44a}$$

$$S = \frac{1}{4N}\sum_{\boldsymbol{k}\sigma}\left[(n^+_{\boldsymbol{k}\sigma} + n^-_{\boldsymbol{k}\bar{\sigma}})(u^2_{\boldsymbol{k}\sigma} + v^2_{\boldsymbol{k}\sigma}) + 4v^2_{\boldsymbol{k}\sigma}\right], \tag{1.44b}$$

where Eq. (1.44b) is the mean-field constraint. Other quantities of interest are

$$L^z = \frac{1}{4N}\sum_{\boldsymbol{k}\sigma}\sigma\left[(n^+_{\boldsymbol{k}\sigma} + n^-_{\boldsymbol{k}\bar{\sigma}})(u^2_{\boldsymbol{k}\sigma} + v^2_{\boldsymbol{k}\sigma}) + 4v^2_{\boldsymbol{k}\sigma}\right], \tag{1.45a}$$

$$S^z = \frac{1}{4N}\sum_{\boldsymbol{k}\sigma}\sigma(n^+_{\boldsymbol{k}\sigma} - n^-_{\boldsymbol{k}\bar{\sigma}}). \tag{1.45b}$$

When $T \leq T_N$, $\mu = -KL^z/2$ and the condensate density is separated from the sums. Note that the condensate contributions, which go as $n_c(u^2_{\boldsymbol{k_c}\uparrow} + v^2_{\boldsymbol{k_c}\uparrow})$, where $\boldsymbol{k_c}$ are the condensation points in the BZ, appear to diverge since $(u^2_{\boldsymbol{k_c}\uparrow} + v^2_{\boldsymbol{k_c}\uparrow}) \propto 1/(\epsilon^+_{\boldsymbol{k_c}\uparrow} + \epsilon^-_{\boldsymbol{k_c}\uparrow})$. However, the energies only go to zero in the thermodynamic limit and so they cannot be taken to zero without simultaneously taking the system size to infinity [26]. Inserting the Bogoliubov coherence

factors, separating the condensate density from the sums, and using Eq. (1.44b) to eliminate it from Eqs. (1.44a) and (1.45a), we get

$$A = S + 1/2 + \frac{1}{4N}\sum_{\boldsymbol{k}\sigma}(n^+_{\boldsymbol{k}\sigma} + n^-_{\boldsymbol{k}\bar{\sigma}} + 1)\left[\gamma_{\boldsymbol{k}}\sqrt{\left(\frac{2\zeta_\sigma + 2JZA}{\epsilon^+_{\boldsymbol{k}\sigma} + \epsilon^-_{\boldsymbol{k}\bar{\sigma}}}\right)^2 - 1} - \frac{2\zeta_\sigma + 2JZA}{\epsilon^+_{\boldsymbol{k}\sigma} + \epsilon^-_{\boldsymbol{k}\bar{\sigma}}}\right], \tag{1.46a}$$

$$L^z = S + 1/2 - \sum_{\boldsymbol{k}}(n^+_{\boldsymbol{k}\downarrow} + n^-_{\boldsymbol{k}\uparrow} + 1)\frac{\zeta_\sigma + JZA}{\epsilon^+_{\boldsymbol{k}\downarrow} + \epsilon^-_{\boldsymbol{k}\uparrow}}, \tag{1.46b}$$

where $\delta_{i,j}$ is the Kronecker delta. Eqs. (1.46a) and (1.46b) no longer contain contributions from the condensate terms, so the sums can now be converted to integrals in order to solve numerically. When $T \geq T_N$, we have $L^z = 0$ and $\mu(T)$ is no longer fixed.

Mean-field equations in the limit $K \ll J$

In the limit $K \ll J$ (e.g., in Cr_2O_3, $K \approx 7 \times 10^{-2} J$ [11]) the mean-field equations are:

$$A = S + C^A - (4N)^{-1}\sum_{\boldsymbol{k}\sigma}(n^+_{\boldsymbol{k}\sigma} + n^-_{\boldsymbol{k}\bar{\sigma}})\sqrt{1-\gamma^2_{\boldsymbol{k}}}, \tag{1.47a}$$

$$L^z = S - C^z - (2N)^{-1}\sum_{\boldsymbol{k}}(n^+_{\boldsymbol{k}\downarrow} + n^-_{\boldsymbol{k}\uparrow})/\sqrt{1-\gamma^2_{\boldsymbol{k}}}, \tag{1.47b}$$

where $C_A = 1/2 - (2N)^{-1}\sum_{\boldsymbol{k}}\sqrt{1-\gamma^2_{\boldsymbol{k}}} \approx 0.13$, $C_z = 1/2 - (N)^{-1}\sum_{\boldsymbol{k}} 1/\sqrt{1-\gamma^2_{\boldsymbol{k}}} \approx 0.25$, the contributions from the zero-energy modes vanish in Eq. (1.47a), and Eq. (1.47b) only contains finite-energy modes. At $T > T_N$: $L^z = 0$ and $\mu(T)$ is no longer fixed so the mean-field equations are:

$$A = (2N)^{-1}\sum_{\boldsymbol{k}\sigma}(n_{\boldsymbol{k}\sigma} + 1/2)\sqrt{(-\mu + JZA)^2/\epsilon^2_{\boldsymbol{k}\sigma} - 1}, \tag{1.48a}$$

$$S = -1/2 + (2N)^{-1}\sum_{\boldsymbol{k}\sigma}(n_{\boldsymbol{k}\sigma} + 1/2)(-\mu + JZA)/\epsilon_{\boldsymbol{k}\sigma}, \tag{1.48b}$$

where we took $n^+_{\boldsymbol{k}\sigma} \approx n^-_{\boldsymbol{k}\sigma} \equiv n_{\boldsymbol{k}\sigma}$, which is valid when $K \ll J$. For S^z we get

$$S^z = \frac{1}{2N} \sum_{\boldsymbol{k}\sigma} \sigma n_{\boldsymbol{k}\sigma}. \tag{1.49}$$

When $T \ll T_{C(N)}$, thermal equilibrium described by the Holstein-Primakoff picture is characterized by a dilute magnon gas with a single band for each sublattice [35], which slightly depolarizes the spin ordering. In SBMFT, there are twice as many bands as in HPA. However, e.g., in the axially-symmetric case, magnons in SBMFT are excitations from the condensed spinons to the thermal cloud. Here, generally, one spin species carries spin along the direction of the sublattice order parameter, while the opposite spin species then mimicks the magnon bands in HPA. In the FM ordered phase, the lowest-energy modes of the $\epsilon^-_\uparrow$ band condense and the two $\epsilon^\pm_\downarrow$ bands match the magnon bands from HPA, which reproduces the usual Bloch $T^{3/2}$ law for demagnetization at $T \ll T_C$ [27]. In the simple-cubic-lattice AF, the the lowest-energy modes of the $\epsilon^+_\uparrow$ and $\epsilon^-_\downarrow$ bands condense at T_N forming staggered ordering while the $\epsilon^+_\downarrow$ and $\epsilon^-_\uparrow$ bands qualitatively match the magnon bands from HPA. See Section 1.3 for a complete discussion. The complete numerical solutions of the MFT for $B = 0$ $S = 3/2$ for the AF, where $n_c \propto L^z$, are plotted in Fig. 1.7 ($T_N = 5.12J$ in units where the Boltzmann constant $k_B = 1$).

1.2.3 Curie-Weiss law in non-interacting paramagnets

In this section we consider the U(1) symmetric MF Hamiltonian with applied field $B\hat{\boldsymbol{z}}$ in the gaseous ($F = A = 0$) paramagnetic phase and self-consistently take the fields $C = D = 0$. The FM and AF mean-field equations have the same form: there are two energy levels which are split by magnetic field, and two mean-field parameters μ and S^z. The mean-field

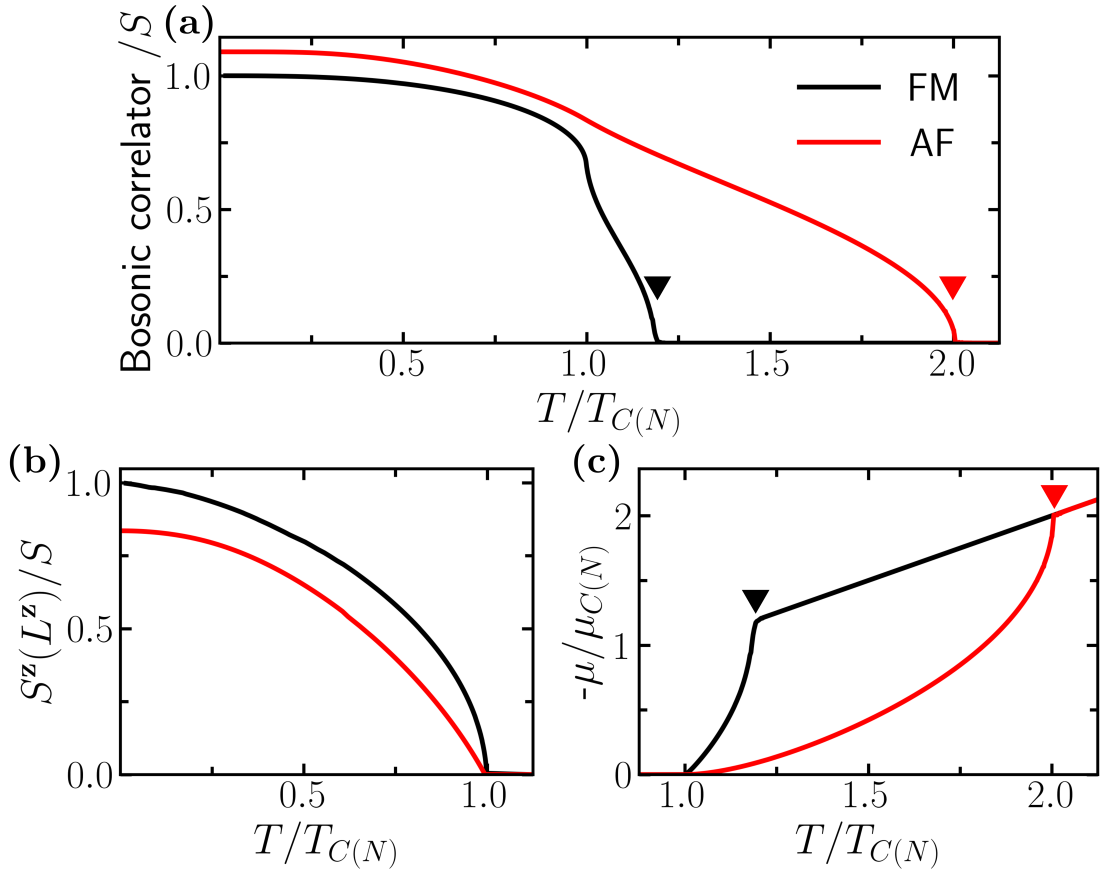

Figure 1.7: Mean-field solutions for the $S = 1/2$ FM on the diamond lattice and the $S = 3/2$ AF on the simple cubic lattice. For the FM (AF), (a) shows F (A), (b) shows S^z (L^z) and (c) shows $-\mu$ in units of $\mu_{C(N)} = -T_{C(N)} \ln(1/S + 1)$. Triangular markers denote the positions of the liquid-gas crossover.

equations are

$$S = (2)^{-1} \sum_{\sigma} n_{\sigma}, \tag{1.50a}$$

$$S^z = (2)^{-1} \sum_{\sigma} \sigma n_{\sigma}, \tag{1.50b}$$

where $\epsilon_{\sigma} = -(\mu + h\sigma/2)$ with $h \equiv \hbar\gamma B + JZ\langle S^z \rangle$, which includes the U(1) term from the mean-field decomposition of the Heisenberg Hamiltonian. At $h \ll T$ the solution (setting $k_B = 1$) is $\mu = -T \ln(1/S + 1) - h/2$ and $S^z/S = \chi B$ where $\chi = \mathcal{C}/(T - \Theta_{CW})$ is the spin-length normalized susceptibility with $\mathcal{C} = (S + 1)\hbar\gamma/2$ and $\Theta_{CW} = JZ\mathcal{C}$, where the

Curie constant $\mathcal{C}$ is a constant factor of 3/2 larger than the usual one.

1.3 Holstein-Primakoff approximation

The Holstein-Primakoff transformation [36] is an exact transformation from the spin ladder operators to magnonic field operators. Since the transformation contains a square root of the magnon number operators, it can only be performed by using a Taylor expansion in the magnon number relative to saturated spin densities. In this sense, it is an order-by-order perturbative expansion in the quantum and thermal fluctuations of a spin state about its fully polarized configuration. We define the Holstein-Primakoff approximation (HPA) as the transformation expanded to second order in the magnon over spin densities.

The purpose of this section is demonstrate agreement between the Holstein-Primakoff magnon dispersions and the SBMFT. In SBMFT, there are two spinon bands for each magnon band (e.g., in a cubic lattice FM there is one magnon band, in bipartite AFs and FMs there are two magnon bands). At $T \ll T_{C(N)}$, one (for the FM) or two (for the AF) of the spinon bands is nearly completely condensed (the condensate density $N_c/N \to 1$, corresponding to saturation of the sublattice spin polarizations). Thus, the dominate excitations which carry spin angular momentum involve annihilating a condensed spinon, and creating a thermal cloud spinon. These are magnons, and the thermal cloud bands whose spin polarization is opposite to the condensate are the ones which match the HPA magnon dispersions.

1.3.1 Heisenberg ferromagnet

For a step-by-step derivation of the spectrum of a Heisenberg ferromagnet under the HPA, see Ref. [37]. The magnon dispersion in HPA in the nearest-neighbor Heisenberg model with

isotropic exchange and applied field B is

$$\epsilon_{\boldsymbol{k}} = \hbar\gamma B + JSZ(1-\gamma_{\boldsymbol{k}}), \tag{1.51}$$

for Z nearest neighbors and spin structure factor $\gamma_{\boldsymbol{k}} \equiv Z^{-1}\sum_{\boldsymbol{\delta}} e^{i\boldsymbol{k}\cdot\boldsymbol{\delta}}$. This agrees with our $\epsilon_{\boldsymbol{k}\downarrow}$ band dispersion in the cubic FM SBMFT in the limit $F \to S$, which occurs when $T \ll T_C$. This agreement was also noted in Refs. [38, 27]. Similarly, in the diamond case, there are two magnon bands which match the $\epsilon^-_{\boldsymbol{k}\downarrow}$ and $\epsilon^+_{\boldsymbol{k}\downarrow}$ SBMFT bands in the same limit.

1.3.2 Easy-axis Heisenberg antiferromagnet below spin flop

For a step-by-step derivation of the spectrum of a Heisenberg antiferromagnet below and above spin flop under the HPA, see Ref. [39]. In this section, we consider the easy-axis Heisenberg AF below spin flop, in order to compare to our SBMFT results. The Bogoliubov transformation here is very similar to the usual Bogoliubov transformation for AF magnons in the Holstein-Primakoff approximation. When $\sigma =\downarrow$, our transformation matches the structure of the magnonic one that diagonalizes the AF Heisenberg Hamiltonian, as discussed in Sec. 1.2.2. The two agree precisely if the dispersions match, and the dispersions are closest when $T \ll T_N$. They are $\epsilon^+_{\boldsymbol{k}\downarrow}, \epsilon^-_{\boldsymbol{k}\uparrow} = \pm b + \epsilon_{\boldsymbol{k}}$, where $\epsilon_{\boldsymbol{k}} = \sqrt{\epsilon_0^2 + (JZA)^2(1-\gamma_{\boldsymbol{k}}^2)}$ with $\epsilon_0^2 = \epsilon_K(\epsilon_K + 2JZA)$ and $\epsilon_K = KL^z$. At $T \ll T_N$, the dispersive term $(JZA)^2(1-\gamma_{\boldsymbol{k}}^2)$ with $A/S = 1 + C_A/S$ differs by a constant factor from the HPA value, and the gap ϵ_0 is proportional to $\epsilon_K = K(S-1/2)$ in HPA while it is $\epsilon_K = K(S-1/2+C_z)$ in SBMFT. The constants are $C_A = 1/2 - (2N)^{-1}\sum_{\boldsymbol{k}}\sqrt{1-\gamma_{\boldsymbol{k}}^2} \approx 0.13$, $C_z = 1/2 - (N)^{-1}\sum_{\boldsymbol{k}} 1/\sqrt{1-\gamma_{\boldsymbol{k}}^2} \approx 0.25$.

Chapter 2

Interfacial spin currents in biased magnetic insulator/metal heterostructures

In this chapter, we derive the dynamical behavior of FMs, AFs, and PMs in linear response to a pertubation. While the static susceptibility encodes the systems response to a time-independent perturbation, the dynamic susceptibility encodes the response to a time-dependent perturbation, and is the central focus of this thesis. Since magnets break time-reversal symmetry in equilibrium, there are spin currents present in equilibrium due to thermal and quantum spin fluctuations. Here, we derive the relation between a magnet's bulk spin current (a linear combination of two-spin correlators), and the response of the system to a time-dependent pertubation in equilibrium. This is accomplished by the fluctuation-dissipation theorem. In this way, we can capture both the thermal and quantum fluctuations using a semiclassical relation. The dynamic susceptibilities that are input to the fluctuation-dissipation relation can be derived from a phenomenological, classical model for the low-energy, long-wavelength fluctuations which dominate the behavior of well-ordered

magnets.

This being said, the spin current in bulk magnets is not directly measurable. In the early 2000's, physicists discovered [40, 41] that attaching a metal to a magnet dramatically increases its resonance linewidths, which are a measure of the system's dissipation. This was theoretically established non-perturbatively [42] by analyzing the scattering matrix between the magnet and the metal. In solid crystalline insulating magnets, the main effect of adding a thin metallic film is to enhance the resonance linewidths [43]. It may be simply captured by treating the interfacial Hamiltonian to leading order in perturbation theory with respect to the bulk magnet's Hamiltonian. In this chapter, we consider interfacial spin currents generated by a temperature discontinuity or spin accumulation between the spin carriers in the magnet and the electrons in metal. In a fully quantum treatment of the magnet, the spin current can be evaluated as the rate of spin flow, minus the backflow, across the interface using Fermi's golden rule. One can then compare this result for the interfacial spin current to the semiclassical result for the bulk spin current. The two can be matched by taking the bulk, semiclassical result thermally averaged with respect to the temperature T_1 of the magnet, minus it averaged at the temperature T_2 of the metal, and multiplying this quantity by an overall phenomenological factor – the real (dissipative) part of the interfacial spin-mixing conductance $g^{\uparrow\downarrow}$. In order to match the two expressions for the interfacial spin current, we require $g^{\uparrow\downarrow} = 4\pi s|J|^2 D^2$, as derived in Ref. [44] for the case of a FM, where s is the spin density in the FM, D is the density of states at the Fermi level, and $|J|$ is the strength of the interfacial exchange coupling.

2.1 Generalized fluctuation dissipation relations

The total spin current flowing across the interface from left to right is $J_s = J_1(T_1, \mu_1) - J_2(T_2, \mu_2)$, assuming we can neglect cross-dependencies (i.e. the spin current on the left

depending on the temperature on the right). In equilibrium ($T_1 = T_2, \mu_1 = \mu_2$), $J_s = 0$, so $J_1 = J_2$. Then in linear response, $\mu_1 = \mu_2 + \delta\mu$ and $T_1 = T_2 + \delta T$, we get for the interfacial spin current

$$J_s(\mu, T) = \mathcal{R}\delta\mu + \mathcal{S}\delta T, \tag{2.1}$$

where $\mathcal{R} \equiv \partial_\mu J$ is the spin impedance, and $\mathcal{S} \equiv \partial_T J$ is the spin Seebeck coefficient. The main goal of this section is to derive semiclassical relations for $J(\mu, T)$ in terms of the relevant components of the dynamic susceptibility tensor χ_{ij}. In the following sections, we will then compute these components of χ_{ij} using classical theories for FMs (AFs), valid when the lowest energy, long-wavelength excitations dominate, at $T \ll T_{C(N)}$. Finally, the spin Seebeck coefficients due to these spin currents are derived in Chapter 3.

2.1.1 Ensemble-generic relations

We begin by considering the linear response of a system described by the Hamiltonian $H(t) = H_0 + H_\xi(t)$, where H_0 is time-invariant and $H_\xi(t) = \phi_j \xi_j(t)$ is a time-dependent perturbation. The density matrix ρ commutes with H_0, with bosonic operators $\phi(t)$. We will work in the interaction picture with time evolution operator $U = U_0 U_I$ where states evolve via $U_0 \equiv e^{\int dt H_0/i\hbar}$ and operators evolve via $U_I \equiv e^{\int dt H_\xi/i\hbar}$.

$$\langle \delta\phi_i(t) \rangle \equiv \langle \phi_i(t) \rangle - \langle \phi_i \rangle|_{\xi=0} \tag{2.2}$$

$$= -\frac{i}{\hbar} \int_{t_0}^{t} dt' \langle [\phi_i(t), \phi_j(t')] \rangle \xi_j(t) \tag{2.3}$$

$$= \frac{1}{\hbar} \int_{-\infty}^{\infty} dt' G^R_{ij}(t - t') \xi_j(t'), \tag{2.4}$$

where we have introduced the retarded Green's function $G^R_{ij}(\omega)$. *The Kubo relation is ensemble-independent*,

$$\langle \delta\phi_i(\omega) \rangle = \frac{1}{\hbar} G^R_{ij}(\omega)\xi_j(\omega) = \chi_{ij}(\omega)\xi_j(\omega), \tag{2.5}$$

which defines the dynamic susceptibility tensor $\chi_{ij}(\omega)$ (a.k.a. the linear-response function). Let us also define the time-ordered Green's function G_{ij},

$$G_{ij}(t,0) = -i\left[\Theta(t)\langle\phi_i(t)\phi_j(0)\rangle + \Theta(-t)\langle\phi_j(0)\phi_i(t)\rangle\right], \tag{2.6}$$

where $\Theta(t)$ is the step function.

2.1.2 From the CE to the GCE

In thermal equilibrium with temperature T, there can be additional quantities where are conserved over time scales which are much longer than the characteristic time scales of our system. Thus, when describing our system we can treat each as a conserved quantity parameterized by its chemical potential μ. We envision this as a generalized "greenhouse effect", as termed by Refs. [45, 46, 47], for quasi-conserved quantities. In our spin systems, for example, if there is U(1) rotational symmetry in spin space about an axis, the spin projected along this axis is conserved. Then, if the interface is a weak link coupling the spin system to a metal, this spin accumulation slowly relaxes into the metal. The interfacial spin current generated by this process can be calculated using the fluctuation-dissipation theorem, generalized for the grand-canonical ensemble.

FDT in the CE

In order to relate G^R_{ij} and G_{ij}, we need a relation between $\langle\phi_i(t)\phi_j(0)\rangle$ and $\langle\phi_j(0)\phi_i(t)\rangle$. These are in turn related by using the cyclic property of the trace, and then treating $e^{-\beta H}\phi e^{\beta H}$ as an imaginary time translation of ϕ with $t \to t - i\beta\hbar$. This yields

$$\int dt e^{i\omega t}\langle\phi_i(t)\phi_j(0)\rangle = e^{\beta\hbar\omega}\int dt e^{i\omega t}\langle\phi_j(0)\phi_i(t)\rangle, \tag{2.7}$$

in the CE where $\rho_c = e^{-\beta H}/\mathcal{Q}_c$. We define $\Im G_{ij}(\omega)$ (for any G)

$$\Im G_{ij}(\omega) \equiv \frac{1}{2i}\left[G_{ij}(\omega) - G^*_{j^\dagger i^\dagger}(\omega)\right], \tag{2.8}$$

where $i^\dagger$ represents $\phi_i^\dagger$.

The time-ordered Green's function contains the symmetrized correlators:

$$\begin{aligned}
\Im G_{ij}(\omega) &= \frac{1}{2i}\left[G_{ij}(\omega) - G^*_{j^\dagger i^\dagger}(\omega)\right] \\
&= -\int_{-\infty}^{\infty} dt e^{i\omega t}\,\mathrm{Re}\left[\Theta(t)\langle\phi_i(t)\phi_j(0)\rangle + \Theta(-t)\langle\phi_j(0)\phi_i(t)\rangle\right] \\
&= -\frac{1}{2}\int_{-\infty}^{\infty} dt e^{i\omega t}\langle\phi_i(t)\phi_j(0) + \phi_j(0)\phi_i(t)\rangle \equiv -\langle\phi_i\phi_j\rangle_\omega \\
&= \frac{1}{2i}\left[G^<_{ij}(\omega) + G^>_{ij}(\omega)\right] \equiv -\langle\phi_i\phi_j\rangle_\omega,
\end{aligned} \tag{2.9}$$

where in the second line we used $\langle\phi_i(t)\phi_j(t')\rangle^* = \langle\phi_j^\dagger(t')\phi_i^\dagger(t)\rangle = \langle\phi_j(t')\phi_i(t)\rangle$. Using Eqn. (2.7), after some algebraic manipulations (for additional, similar relations between Green's functions, see Yaroslav's 242 notes), we get for the FDT in the CE,

$$\Im G_{ij}(\omega) \equiv \frac{1}{2i}\left[G^<_{ij}(\omega) + G^>_{ij}(\omega)\right] = \Im G^R_{ij}(\omega)\coth(\beta\hbar\omega/2) = \Im G^R_{ij}(\omega)\left[n(\omega) + 1/2\right]. \tag{2.10}$$

Using the Kubo relation, we may write the spectral function $\Im G^R_{ij}(\omega)$ in terms of the dynamic

susceptibility tensor,

$$\Im G^R_{ij}(\omega) = \frac{\hbar}{2i}\left[\chi_{ij}(\omega) - \chi^*_{j^\dagger i^\dagger}(\omega)\right]. \tag{2.11}$$

Finally, the FDT may be reexpressed using Eqn. (2.9) (for spatially-homogeneous systems) as

$$\langle \phi_i \phi_j \rangle = -i\hbar \int \frac{d^3k}{(2\pi)^3} \int \frac{d\omega}{2\pi} \left[\chi_{ij}(\mathbf{k},\omega) - \chi^*_{j^\dagger i^\dagger}(\mathbf{k},\omega)\right] N(\omega), \tag{2.12}$$

where $N(\omega) \equiv n(\omega) + 1/2$ accounts for thermal fluctuations associated with occupied modes, according to the Bose-Einstein distribution function n, and the $1/2$ reflects zero-point motion. The components χ_{ij} and χ_{ji} are related by Onsager reciprocity:

$$\chi_{ij}(\mathbf{B}) = \pm\chi_{ji}(-\mathbf{B}), \tag{2.13}$$

where $\pm$ indicates an even (odd) product of the signs of ϕ_i and ϕ_j under time reversal, $\mathbf{B}$ is a magnetic field (or other quantity entering the Hamiltonian which is odd under time reversal). The time-reversibility of $\mathbf{B}$ enters when evaluating the thermal expectation value of χ_{ij} under the CE.

FDT in the GCE

In the GCE, however, the density matrix is weighted by the Hamiltonian and the chemical potential μ for conserved quantity n,

$$\rho_{gc} = e^{-\beta(H-\mu n)}/\mathcal{Q}_{gc}, \tag{2.14}$$

where $\mathcal{Q}_{gc}$ is the grand partition function. One way to obtain the modified version of Eqn. (2.10) is to shift the time evolution operator to match the new density matrix with the

following transformations (assuming $[H, n] = 0$):

$$H' \equiv H - \mu n, \tag{2.15a}$$

$$\rho_{gc}(H, \mu) = \rho_c(H'), \tag{2.15b}$$

$$\phi(\omega) \to \int dt e^{i\omega t} e^{iH't/\hbar} e^{-i\mu nt/\hbar} \phi e^{i\mu nt/\hbar} e^{-iH'} t/\hbar \equiv \int dt e^{i\omega t} e^{iH't/\hbar} \phi' e^{-iH't/\hbar}. \tag{2.15c}$$

The new Hamiltonian has its own response function, $\chi'_{ij}(\omega)$. The operators now evolve according to the new Hamiltonian, which redefines the Green's functions. Note that the new Hamiltonian satisfies the relation coming from the cyclic property of the trace, Eqn. (2.7), now with $\rho = \rho_{gc}(H) = \rho_c(H')$. Thus the factor of $\coth(\beta\hbar\omega/2)$ in Eqn. (2.10) remains unchanged when switching from the CE to the GCE and simultaneously to the new Hamiltonian. For the case $[\phi, n] = \eta\phi$, Eqn. (2.15) is solve by $\phi' \to \phi e^{-i\eta\mu t/\hbar}$.

For example, we will take $\eta = \pm 1$. First we will evaluate the dynamic susceptibility tensor using a set of phenomenological equations of motion for $\phi(t)$. Then we will switch to primed variables to calculate correlators in the GCE, and insert the transformation, Eqn. (2.15), to write the primed in terms of unprimed variables. Finally, we will apply the FDT in the CE along with the trivial shift in ω due to the transformation, giving us the correlators in the GCE.

The components χ_{ij} and χ_{ji} are related by Onsager reciprocity:

$$\chi_{ij}(\mathbf{B}, \mu) = \pm\chi_{ji}(-\mathbf{B}, -\mu), \tag{2.16}$$

where n is assumed to be odd under time reversal in the case of e.g. spin conservation (if n is even in the case of e.g. charge conservation, then $\chi_{ij}(\mathbf{B}, \mu) = \pm\chi_{ji}(-\mathbf{B}, +\mu)$). The time reversibility of n enters when evaluating the thermal expectation value of χ_{ij} under the GCE.

2.1.3 Form of the FDT for several types of operators

Hermitian operators in the CE

Consider Hermitian operators, $\phi_i = \phi_i^\dagger$ and $\phi_j = \phi_j^\dagger$. Then the FDT, Eqn. (2.12), reads

$$\langle \phi_i \phi_j \rangle = -i\hbar \int \frac{d^3k}{(2\pi)^3} \int \frac{d\omega}{2\pi} \left[\chi_{ij}(\mathbf{k},\omega) - \chi_{ji}^*(\mathbf{k},\omega) \right] N(\omega). \tag{2.17}$$

These susceptibility components follow the general property of retarded correlators, $\chi_{ij}(\omega)^* = \chi_{ij}(-\omega)$, since the spin operators ϕ_i and ϕ_j are Hermitian.

Hermitian conjugate operator pairs in the CE

Consider the conjugate pair, $\phi_i = \phi_i^\dagger$; e.g., ladder operators. In this case, for all G, $\Im G = \operatorname{Im} G$ and $\Re G = \operatorname{Re} G$. Then the FDT, Eqn. (2.12), reads

$$\left\langle \phi_i \phi_i^\dagger \right\rangle = -2\hbar \int \frac{d^3k}{(2\pi)^3} \int \frac{d\omega}{2\pi} \operatorname{Im} \chi_{ii^\dagger}(\mathbf{k},\omega) N(\omega). \tag{2.18}$$

Ladder operators in the GCE

Consider spin ladder operators $S_+ = S_x + iS_y, S_- = S_x - iS_y$ with Cartesian components $[S_i, S_j] = i\hbar\epsilon_{ijk}$, $[S_z, S_\pm] = \pm S_\pm$ and $n = S_z$. Evaluate the two point correlation function $\langle S_+ S_- \rangle_\omega$ in the GCE. Taking $\phi_i = S_\pm$, Eqn. (2.15)c becomes

$$S_\pm(\omega) \to \int dt e^{i\omega t} e^{iH't/\hbar} e^{-i\mu S_z t/\hbar} S_\pm e^{i\mu S_z t/\hbar} e^{-iH't/\hbar} = S_\pm(\omega \pm \mu/\hbar). \tag{2.19}$$

This transformation takes $\chi_{+-}(\omega) \to \chi_{+-}(\omega + \mu/\hbar)$ and $G_{+-}(\omega) \to G_{+-}(\omega + \mu/\hbar)$, while the factor of $N(\omega)$ is unaltered; and similarly for $\chi_{-+}(\omega)$. Shifting ω, the FDT in this case, Eqn.(2.18), is

$$\langle S_+ S_- \rangle = -2\hbar \int \frac{d^3k}{(2\pi)^3} \int \frac{d\omega}{2\pi} \, \mathrm{Im}\, \chi_{+-}(\mathbf{k}, \omega) N(\omega - \mu/\hbar), \tag{2.20a}$$

$$\langle S_- S_+ \rangle = -2\hbar \int \frac{d^3k}{(2\pi)^3} \int \frac{d\omega}{2\pi} \, \mathrm{Im}\, \chi_{-+}(\mathbf{k}, \omega) N(\omega + \mu/\hbar). \tag{2.20b}$$

2.2 Spin current in Heisenberg ferromagnets

In this section we derive the interfacial spin current between a FM insulator and a metal, where the interfacial coupling is treated as a weak link, using a semiclassical approach and SBMFT. In the former approach, the dynamic susceptibilities are evaluated in the classical, phenomenological theory for the FM (Landau-Lifshitz phenomenology), which is valid at $T \ll T_C$, and then inserted into semiclassical fluctuation-dissipation relations. When the interfacial coupling to the metal is turned on, the interfacial spin current is given by the bulk expression, evaluated at the temperature T_1 of the magnet, minus the back flow at the temperature T_2 of the metal, up to a phenomenological constant. This constant, the real part of the spin-mixing conductance, can be derived using Holstein-Primakoff, in the dilute magnon gas limit, as shown in Ref. [48]. Since our SBMFT result matches the Holstein-Primakoff result exactly in the limit $T \ll T_C$, SBMFT can also be used to perform the same matching.

Our SBMFT result can be taken to arbitrary temperature. We find that the spin current in a FM contains the usual magnon contribution, which arises from scattering between the condensate and the $\downarrow$ spinon bands, which mimick magnons. The SBMFT spin current in

FMs also contains a paramagnetic-like contribution that grows with T. It arises due to scattering between two continuous spinon bands. The physical picture for these processes is shown in Fig. 2.1.

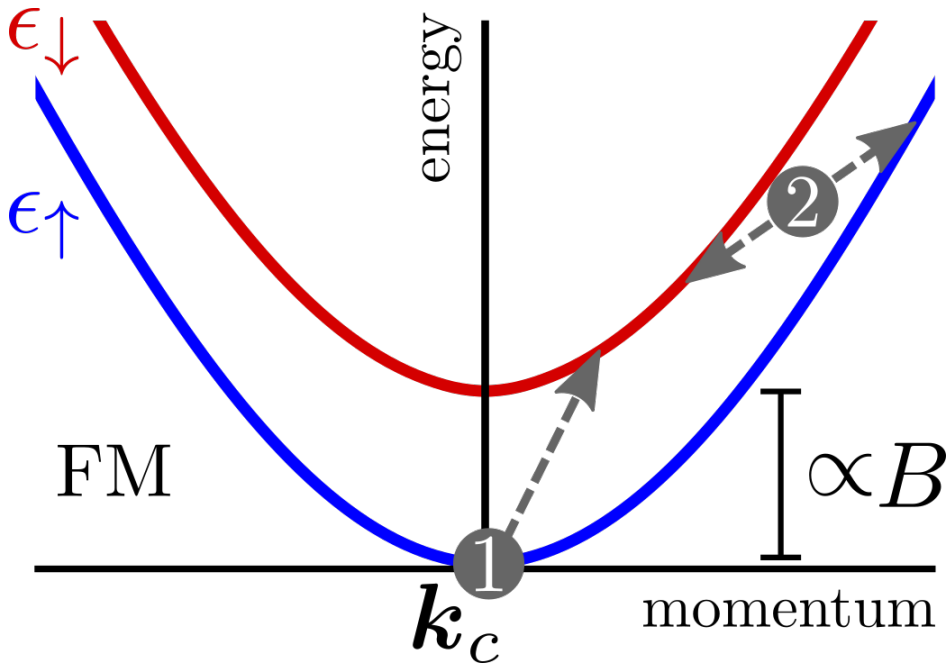

Figure 2.1: Schematic depiction of the magnonic (1) and paramagnetic-like (2) contributions to J_s. Colors specify the bands' lower-indexed spin polarization. In SBMFT for FMs, $\mu = 0$ at $T \leq T_C$, resulting in Bose-Einstein condensation at the lowest-energy modes with momentum $\boldsymbol{k_c}$. At $T > T_C$, the bands are gapped by $-\mu > 0$.

2.2.1 Semiclassical result

Consider a FM with magnon temperature T, conservation of the z-component of spin parameterized by μ, and directional order parameter $\boldsymbol{m}$ with constraint $\boldsymbol{m}^2 = 1$. The spin current density generated at the interface

$$\boldsymbol{J} = (\hbar g^{\uparrow\downarrow}/4\pi)\, \boldsymbol{m} \times \partial_t \boldsymbol{m}, \tag{2.21}$$

where $g^{\uparrow\downarrow}$ is the real part of the dimensionless interfacial spin-mixing conductance per unit area. Defining $m_\pm = m_x \pm i m_y$ (making the conjugate fields $h_\pm = (h_x \mp i h_y)/2$) and inserting

Eqn.(2.20), we get for the z-component

$$J_z(\omega,k) = -i\omega(\hbar g^{\uparrow\downarrow}/4\pi)\left[\langle m_x m_y\rangle - \langle m_y m_x\rangle\right] = \omega(\hbar g^{\uparrow\downarrow}/8\pi)\left[\langle m_+ m_-\rangle - \langle m_- m_+\rangle\right],$$
$$J_z = -\frac{\hbar^2 g^{\uparrow\downarrow}}{4\pi}\int\frac{d^3k}{(2\pi)^3}\int\frac{d\omega}{2\pi}\,\omega\left[\mathrm{Im}\,\chi_{+-}N(\omega-\mu/\hbar) - \mathrm{Im}\,\chi_{-+}N(\omega+\mu/\hbar)\right]. \tag{2.22}$$

From the equations of motion for the FM with spin density s and spin waves with resonance frequency $\omega_k = \omega_0 + Ak^2$, we get

$$\chi_{xy} = -\chi_{yx} = \frac{i}{2s}\left[\frac{1}{\omega-\omega_k+i\epsilon} + \frac{1}{\omega+\omega_k+i\epsilon}\right], \tag{2.23a}$$
$$\chi_{+-} = \frac{2}{s}\frac{1}{\omega-\omega_k+i\epsilon}, \quad \chi_{-+} = \frac{2}{s}\frac{1}{\omega+\omega_k+i\epsilon}, \tag{2.23b}$$

where ϵ is the resonance linewidth ($\chi_{xy} = -\chi_{yx}$ by axial symmetry). Note that under Onsager reciprocity the positive and negative poles interchange $+\omega_k \leftrightarrow -\omega_k$ since $\boldsymbol{m} \to -\boldsymbol{m}$ under Onsager reciprocity, which flips the direction of precession. After inserting Eqn. (2.23b) into Eqn. (2.22), splitting the pole into its real and imaginary parts, and integrating over ω, we get for the spin current in the GCE,

$$J_z(T,\mu) = \left(\frac{\hbar g^{\uparrow\downarrow}}{4\pi}\right)\frac{2\hbar}{s}\int\frac{d^3k}{(2\pi)^3}\omega_k N(\omega_k - \mu/\hbar). \tag{2.24}$$

In conclusion, our result shows that $J_z(T,\mu)$ in the GCE is equivalent to $J_z(T)$ in the CE (which may be calculated directly by inserting Eqn. (2.23b) into Eqn.(2.17)) with the magnon occupation numbers evolving from the Planck to the Bose-Einstein distribution functions.

2.2.2 Holstein-Primakoff result

For reference, see [44].

2.2.3 Schwinger boson result

At $T < T_C$, the sums are converted to integrals with the contributions from the condensate density separated explicitly: for an arbitrary function z and a single condensation point at momentum $\boldsymbol{k_c}$, $\sum_{\boldsymbol{k}} z_{\boldsymbol{k}}/N \approx z(\boldsymbol{k_c})N_c/N + \mathcal{V}\int_{\mathrm{BZ}} d^3\boldsymbol{k}\ z(\boldsymbol{k})$, where $n_c \equiv N_c/N$ and $\mathcal{V}$ is the unit cell volume. The interfacial spin current per unit area of the interface is given by $J_s = \hbar(\Gamma_{\uparrow\downarrow} - \Gamma_{\downarrow\uparrow})/\mathcal{A}$, where $\Gamma_{\uparrow\downarrow} - \Gamma_{\downarrow\uparrow}$ is the rate of spin relaxation in the magnet and $\mathcal{A}$ is the area of the interface. The interfacial Hamiltonian for a FM is

$$H_{\mathrm{int}}^{\mathcal{A}} = (V/N) \sum_{\boldsymbol{k},\boldsymbol{k'},q,q'} a^\dagger_{\boldsymbol{k}\uparrow} a_{\boldsymbol{k'}\downarrow} c^\dagger_{q\downarrow} c_{q'\uparrow} + \mathrm{H.c}, \tag{2.25}$$

$$H_{\mathrm{int}}^{\mathcal{B}} = (V/N) \sum_{k,k',q,q'} b^\dagger_{k\uparrow} b_{k'\downarrow} c^\dagger_{q\downarrow} c_{k'\uparrow} + \mathrm{H.c.} \tag{2.26}$$

The rates are evaluated to leading order in the interfacial relative to bulk Hamiltonian via Fermi's golden rule (FGR). The quartic correlators in FGR are decoupled via Wick's theorem.

Cubic lattices

In the cubic case, the interfacial Hamiltonian is $H_{\mathrm{int}} = (V/N)\sum_{\boldsymbol{k},\boldsymbol{k'},q,q'} a^\dagger_{\boldsymbol{k}\uparrow} a_{\boldsymbol{k'}\downarrow} c^\dagger_{q\downarrow} c_{q'\uparrow} + \mathrm{H.c}$, where N is the number of sites in the bulk magnet. After integrating over one of the Fermi gas energies with the δ-fnc, the FGR results for Fermi-Dirac distribution function $f(x)$ are

$$\begin{aligned}\Gamma_{\uparrow\downarrow} =& \frac{2\pi}{\hbar} V^2 D^2 \frac{N_c}{N^2} \int \frac{d^3\boldsymbol{k'}}{(2\pi)^3} \left[n(\beta_1 \epsilon_{\boldsymbol{k'}\downarrow}) + 1\right] \int d\epsilon f(\beta_2\epsilon + \beta_2 \epsilon_{\boldsymbol{k'}\downarrow}) \left[1 - f(\beta_2\epsilon)\right] + \\ & \frac{2\pi}{\hbar} V^2 D^2 \frac{1}{N^2} \int \frac{d^3\boldsymbol{k}}{(2\pi)^3} n(\beta_1 \epsilon_{\boldsymbol{k}\uparrow}) \int \frac{d^3\boldsymbol{k'}}{(2\pi)^3} \left[n(\beta_1 \epsilon_{\boldsymbol{k'}\downarrow}) + 1\right] \int d\epsilon f(\beta_2\epsilon - \beta_2\epsilon_{\boldsymbol{k}\uparrow} + \beta_2 \epsilon_{\boldsymbol{k'}\downarrow}) \left[1 - f(\beta_2\epsilon)\right],\end{aligned} \tag{2.27}$$

and

$$\Gamma_{\downarrow\uparrow} = \frac{2\pi}{\hbar} V^2 D^2 \frac{N_c}{N^2} \int \frac{d^3\boldsymbol{k'}}{(2\pi)^3} n(\beta_1 \epsilon_{\boldsymbol{k'}\downarrow}) \int d\epsilon f(\beta_2 \epsilon) \left[1 - f(\beta_2 \epsilon + \beta_2 \epsilon_{\boldsymbol{k'}\downarrow})\right] + \frac{2\pi}{\hbar} V^2 D^2 \frac{1}{N^2} \int \frac{d^3\boldsymbol{k}}{(2\pi)^3} \left[n(\beta_1 \epsilon_{\boldsymbol{k}\uparrow}) + 1\right] \int \frac{d^3\boldsymbol{k'}}{(2\pi)^3} n(\beta_1 \epsilon_{\boldsymbol{k'}\downarrow}) \int d\epsilon f(\beta_2 \epsilon) \left[1 - f(\beta_2 \epsilon - \beta_2 \epsilon_{\boldsymbol{k}\uparrow} + \beta_2 \epsilon_{\boldsymbol{k'}\downarrow})\right], \tag{2.28}$$

where D is the density of states at the Fermi level in units of (energy·volume)$^{-1}$. The net interfacial spin current density is

$$J_s = J^{\mathrm{FM}} + J^{\mathrm{PM}}, \tag{2.29a}$$

$$J^{\mathrm{FM}} = -\frac{2\pi V^2 D^2}{\mathcal{A}} \frac{N_0}{N} \int \frac{d^3\boldsymbol{k'}}{(2\pi)^3} \epsilon_{\boldsymbol{k'}\downarrow} \left[n_1(\epsilon_{\boldsymbol{k'}\downarrow}) - n_2(\epsilon_{\boldsymbol{k'}\downarrow})\right], \tag{2.29b}$$

$$J^{\mathrm{PM}} = -\frac{2\pi V^2 D^2}{\mathcal{A}} \int \frac{d^3\boldsymbol{k}}{(2\pi)^3} \int \frac{d^3\boldsymbol{k'}}{(2\pi)^3} \epsilon_{\boldsymbol{k}\boldsymbol{k'}\uparrow\downarrow} [n_2(-\epsilon_{\boldsymbol{k}\boldsymbol{k'}\uparrow\downarrow}) n_1(\epsilon_{\boldsymbol{k}\uparrow}) + n_2(\epsilon_{\boldsymbol{k}\boldsymbol{k'}\uparrow\downarrow}) n_1(\epsilon_{\boldsymbol{k'}\downarrow}) - n_1(\epsilon_{\boldsymbol{k}\uparrow}) n_1(\epsilon_{\boldsymbol{k'}\downarrow})], \tag{2.29c}$$

where $\epsilon_{\boldsymbol{k}\boldsymbol{k'}\uparrow\downarrow} \equiv \epsilon_{\boldsymbol{k}\uparrow} - \epsilon_{\boldsymbol{k'}\downarrow}$, $\mathcal{A}$ is the area of the interface per site, and we made use of the identity: $\int d\epsilon f(\epsilon) \left[1 - f(\epsilon - \delta)\right] = n(\delta)\delta$. J_s contains a contribution $J^{\mathrm{FM}} \propto N_c$ due to the thermal cloud scattering off the condensate (vanishing at $T \geq T_c$) and a contribution J^{PM} which is asymptotically smaller than J^{FM} when $T \to 0$ and is $\propto B$ at small B, but remains at $T > T_c$. Note that when $T_1 = T_2$, we clearly have $J^{\mathrm{FM}} = 0$ and using the identity $n(y-x)n(x) + n(x-y)n(y) = n(x)n(y)$ we also have $J^{\mathrm{PM}} = 0$.

We can simplify the form of J^{PM} by inserting the identities $n(y-x)n(x)+n(x-y)n(y) = n(x)n(y)$ and $n(y-x) + n(x-y) = -1$. Doing this, and writing J_s in terms of sums (with the condensate terms built-in), we have

$$J_s = \frac{g_{\uparrow\downarrow}}{2SN^2} \sum_{\boldsymbol{k},\boldsymbol{k'}} \epsilon_{\boldsymbol{k}\boldsymbol{k'}\uparrow\downarrow} \left[n_1(\epsilon_{\boldsymbol{k}\uparrow}) - n_1(\epsilon_{\boldsymbol{k'}\downarrow})\right] \left[n_1(\epsilon_{\boldsymbol{k}\boldsymbol{k'}\uparrow\downarrow}) - n_2(\epsilon_{\boldsymbol{k}\boldsymbol{k'}\uparrow\downarrow})\right], \tag{2.30}$$

where $g_{\uparrow\downarrow} \equiv 4\pi S D^2 V^2/\mathcal{A}$ [48] is in units of inverse area where D is the metal's density of states at the Fermi level in units of (energy·volume)$^{-1}$ and $\mathcal{A}$ the area per site of the interface. At low temperatures $T \ll T_C$ and low fields $\hbar\gamma B \ll J$, $J_s \approx J^{\rm FM}$. In this limit our result for $J^{\rm FM}$ identically matches the Holstein Primakoff result, with the same type of interfacial coupling, when it is expanded to leading order in the magnon over spin densities (the dilute magnon gas limit). See Ref. [48] for the published Holstein-Primakoff result in the dilute limit. It also matches our semi-classical result for the low-temperature FM spin current, (2.24) evaluated at T_1 minus the back flow at T_2, after inserting the phenomenological constants in the classical bulk FM Hamiltonian from those given by Holstein-Primakoff (which agree identically with SBMFT). The SBMFT solutions in this limit are $F \approx S$ and $S^z \approx S$.

Diamond lattice

For diamond, $J_s = J_s^{\mathcal{A}} + J_s^{\mathcal{B}}$, where $J_s^{\mathcal{A}}$ is generated by the coupling $H_{\rm int}^{\mathcal{A}}$, and $J_s^{\mathcal{B}}$ by $H_{\rm int}^{\mathcal{B}}$. After inserting the eigenvectors $v_{\boldsymbol{k}\sigma}^{\pm} = (1, \mp|\gamma_{\boldsymbol{k}}|/\gamma_{\boldsymbol{k}})/\sqrt{2}$ into the interfacial Hamiltonian and then evaluating the spin relaxation rate via FGR, we find $J_s^{\mathcal{A}} = J_s^{\mathcal{B}} = J_s/2$, and we get

$$J_s = \frac{g_{\uparrow\downarrow}}{2SN^2} \sum_{\nu,\nu',\boldsymbol{k},\boldsymbol{k'}} \epsilon_{\boldsymbol{k}\boldsymbol{k'}\uparrow\downarrow}^{\nu\nu'} \left[n_1(\epsilon_{\boldsymbol{k}\uparrow}^{\nu}) - n_1(\epsilon_{\boldsymbol{k'}\downarrow}^{\nu'}) \right] \left[n_1(\epsilon_{\boldsymbol{k}\boldsymbol{k'}\uparrow\downarrow}^{\nu\nu'}) - n_2(\epsilon_{\boldsymbol{k}\boldsymbol{k'}\uparrow\downarrow}^{\nu\nu'}) \right], \tag{2.31}$$

where $\epsilon_{\boldsymbol{k}\boldsymbol{k'}\uparrow\downarrow}^{\nu\nu'} \equiv \epsilon_{\boldsymbol{k}\uparrow}^{\nu} - \epsilon_{\boldsymbol{k'}\downarrow}^{\nu'}$ and the sums run over the pseudospin indices $\nu, \nu' = +, -$. Note that J_s only contains scattering between $\uparrow$ and $\downarrow$ bands. Scattering between two bands with the same σ would not transfer spin anguler momentum across the interface, and thus does not contribute to spin transport. Again, at low temperatures $T \ll T_C$ and low fields $\hbar\gamma B \ll J$, $J_s \approx J^{\rm FM}$. In this limit our result for $J^{\rm FM}$ identically matches the Holstein Primakoff result (there are two magnon bands on diamond), with the same type of interfacial coupling, when it is expanded to leading order in the magnon over spin densities (the dilute magnon gas

limit). At arbitrary temperatures in the FM on diamond, J_s contains both intraband and interband scattering, as shown in Fig. 2.2. This does not violate our constraint since, note that the SBMFT constraint fixed the expectation value of the number of $\uparrow$ and $\downarrow$ SBs on each sublattice. However, the diagonal basis of the Hamiltonian is in terms of spinon operators α_σ and β_σ, whose number operators are each given by an equal mixture of those for the two sublattices. Thus, the SBMFT constraints for each sublattice actually fixes the expectation value of the total number of α_σ and β_σ modes. Therefore, a scattering process which creates α spinons and annihilates β spinons (or vice versa) does not violate the constraints. See Chapter 3 for a quantitative comparison of the SBMFT and Holstein-Primakoff spin Seebeck coefficients (interfacial spin current divided by the temperature discontinuity $T_1 - T_2$) on diamond.

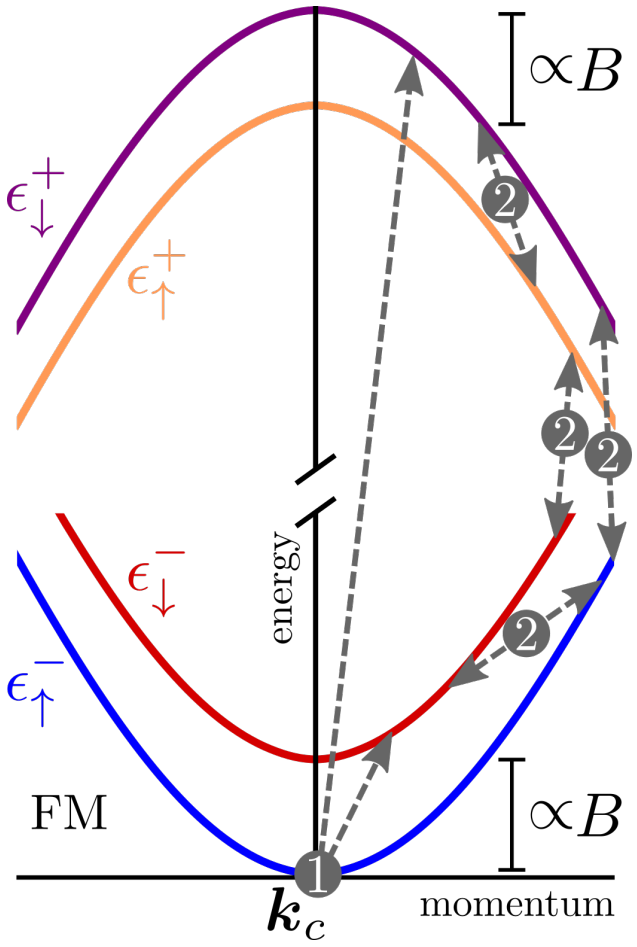

Figure 2.2: Schematic depiction of the scattering processes which make up J_s in the FM SBMFT on diamond. At $T > T_C$, all bands are gapped by μ. As $T \to T_C$, $\mu \to 0$, and the lowest energy mode of the $\epsilon^-_\uparrow$ band condenses, as shown here. Near the condensation point $\boldsymbol{k_c}$, the + bands are maximal. Processes labeled by (1) are magnonic excitations, which dominate J_s at $T \ll T_C$; while (2) result in a paramagnetic-like contribution to J_s, which vanishes as $B \to 0$.

2.3 Spin current in Heisenberg antiferromagnets with easy-axis anisotropy

In this section we derive the interfacial spin current between an AF insulator and a metal, where the interfacial coupling is treated as a weak link, using a semiclassical approach and SBMFT. In the former approach, the dynamic susceptibilities are evaluated in the classical,

phenomenological theory for the AF (the nonlinear σ model), which is valid at $T \ll T_N$, and then inserted into semiclassical fluctuation-dissipation relations. When the interfacial coupling to the metal is turned on, the interfacial spin current is given by the bulk expression, evaluated at the temperature T_1 of the magnet, minus the back flow at the temperature T_2 of the metal, up to a phenomenological constant. This constant, the real part of the spin-mixing conductance, has both a Néel and magnetic part [49, 50]. Our SBMFT result reproduces the semiclassical Néel spin current in the limit $T \ll T_N$.

Like the FM, we find that the SBMFT spin current in an AF contains the usual magnon-like contributions. In the AF, BEC occurs when the lowest-energy modes of $\epsilon_{\uparrow}^{+}$ and $\epsilon_{\downarrow}^{-}$ simultaneously become gapless at T_N, forming staggered ordering. Then, excitations between the $+$ $(-)$ condensate and the $\epsilon_{\downarrow}^{+}$ $(\epsilon_{\uparrow}^{-})$ bands qualitatively match the magnon bands from HPA. The SBMFT spin current in easy-axis AFs also contains a paramagnetic-like contribution that grows with T, and has the opposite sign to the low-field magnon-like contribution. It arises due to scattering between two continuous spinon bands. The physical picture for these processes is shown in Fig. 2.3.

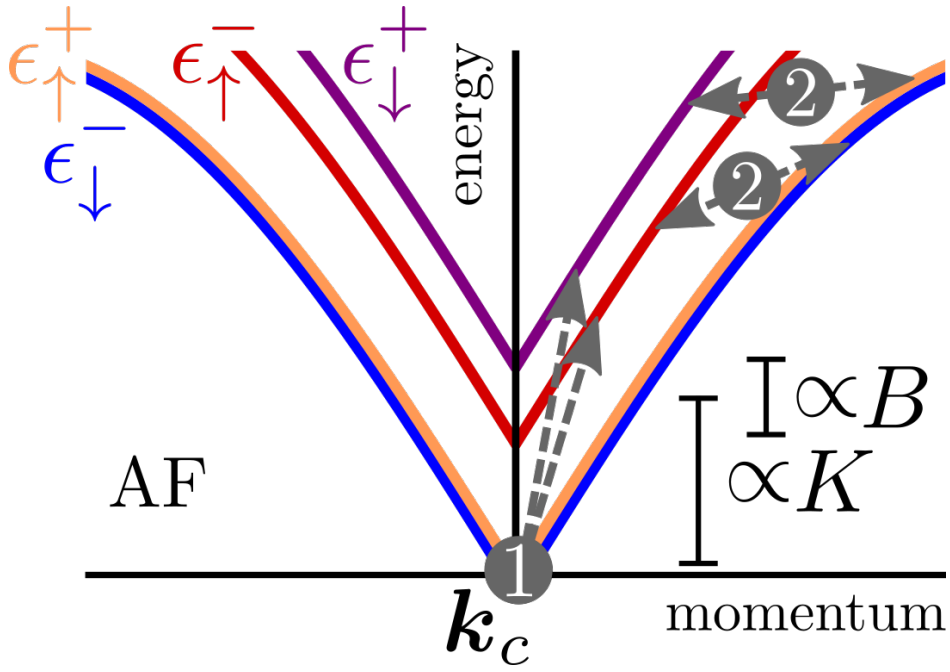

Figure 2.3: Schematic depiction of the magnonic (1) and paramagnetic-like (2) contributions to J_s. Colors specify the bands' lower-indexed spin polarization and upper-indexed pseudospin. In SBMFT for AFs, $\mu = 0$ at $T \leq T_N$, resulting in Bose-Einstein condensation at the lowest-energy modes with momentum $\boldsymbol{k_c}$ At $T > T_N$, all the bands are gapped by $-\mu > 0$..

2.3.1 Semiclassical GCE result below spin flop

Consider a U(1)-symmetric AF below spin flop with applied field $\mathbf{B} = B\hat{\mathbf{z}}$ along the easy-axis. There is directional Néel order $\boldsymbol{l}$ with nonlinear σ-model constraint $\boldsymbol{l}^2 = 1$ and net spin density $\boldsymbol{m}$ normalized by the saturated spin density, and sublattice symmetry making $\boldsymbol{l} \cdot \boldsymbol{m} = 0$. U(1) symmetry implies conservation of $\boldsymbol{m}_z$, to which we assign chemical potential μ. The spin current consists of Néel, $\boldsymbol{J}_l$, and magnetic, $\boldsymbol{J}_m$, contributions:

$$\boldsymbol{J}_l = (\hbar g_l^{\uparrow\downarrow}/4\pi)\, \boldsymbol{l} \times \partial_t \boldsymbol{l}, \quad \boldsymbol{J}_m = (\hbar g_m^{\uparrow\downarrow}/4\pi)\, \boldsymbol{m} \times \partial_t \boldsymbol{m}, \tag{2.32}$$

which may be written in terms of ladder operators $\boldsymbol{l}_\pm$ and $\boldsymbol{m}_\pm$ analogously to Eqn. (2.22), with $[m_z, m_\pm] = \pm m_\pm$ and $[m_z, l_\pm] = \pm l_\pm$. Since below spin flop $J_m \sim (T/T_N)^2 J_l$, we will focus on the Néel dynamics here. The main difference between the AF and the FM is that

in the AF there are two modes, $\omega_{1k} = -B + \omega_{0k}$ and $\omega_{2k} = B + \omega_{0k}$ with $\omega_{0k} = \sqrt{\omega_0^2 + (ck)^2}$, associated with magnons which carry angular momentum, along $\hat{z}$, $+\hbar$ and $-\hbar$, respectively; whereas the FM has a single mode that carries $-\hbar$. We will see that this difference between the AF modes will be reflected in the sign of μ that appears in their associated Bose-Einstein distribution functions, as borne out by the particular poles which appear in χ_{+-} and χ_{-+}.

From the equations of motion, we derive the off-diagonal components of the Néel dynamic susceptibilities,

$$\chi_{xy}^{(l)} = -\chi_{yx}^{(l)} = -\frac{i}{4s^2\chi\omega_{0k}}\left(\frac{1}{\omega-\omega_{1k}+i\epsilon}+\frac{1}{\omega+\omega_{1k}+i\epsilon}-\frac{1}{\omega-\omega_{2k}+i\epsilon}-\frac{1}{\omega+\omega_{2k}+i\epsilon}\right), \tag{2.33a}$$

$$\chi_{+-}^{(l)} = -\frac{1}{\chi s^2\omega_{0k}}\left[\frac{1}{\omega-\omega_{1k}+i\epsilon}-\frac{1}{\omega+\omega_{2k}+i\epsilon}\right], \quad \chi_{-+}^{(l)} = \frac{1}{\chi s^2\omega_{0k}}\left[\frac{1}{\omega+\omega_{1k}+i\epsilon}-\frac{1}{\omega-\omega_{2k}+i\epsilon}\right], \tag{2.33b}$$

where again under Onsager reciprocity the positive pole and negative poles of the same type interchange $+\omega_{ik} \leftrightarrow -\omega_{ik}$. Splitting the poles into their real and imaginary parts and inserting Eqn. (2.33b) into Eqn. (2.22), we get for the Néel spin current,

$$\begin{aligned} J_z(T,\mu) &= -\frac{\hbar^2 g_l^{\uparrow\downarrow}}{4\pi}\int\frac{d^3k}{(2\pi)^3}\int\frac{d\omega}{2\pi}\,\omega\left[\mathrm{Im}\,\chi_{+-}N(\omega-\mu/\hbar)-\mathrm{Im}\,\chi_{-+}N(\omega+\mu/\hbar)\right], \\ &= -\left(\frac{\hbar g_l^{\uparrow\downarrow}}{4\pi}\right)\frac{\hbar}{s^2\chi}\int\frac{d^3k}{(2\pi)^3}\frac{1}{\omega_{0k}}\left[\omega_{1k}N(\omega_{1k}-\mu/\hbar)-\omega_{2k}N(\omega_{2k}+\mu/\hbar)\right]. \end{aligned} \tag{2.34}$$

In conclusion, our result shows that $J_z(T,\mu)$ in the GCE is equivalent to $J_z(T)$ in the CE (which may be calculated directly by inserting Eqn. (2.33a) into Eqn. (2.17)) with the magnon occupation numbers evolving from the Planck to the Bose-Einstein distribution functions. Here, m_z is conserved and is parameterized by chemical potential μ; the $\omega_{1(2)}$ mode is a magnon excitation which increases (decreases) m_z by $\hbar$ so it has chemical potential $\pm\mu$. This agrees with the results derived using the HPA in Ref. [12]. According to Eq. (2.34), the

fluctuations transverse to $\boldsymbol{l}_{0,\mathrm{I}} = \hat{\mathbf{z}}$ at ω_{1k} and ω_{2k} produce opposite-sign contributions to the spin currents.

2.3.2 Semiclassical CE result below and above spin flop

Below spin flop

The components $\chi_{ij}^{(l)}$ contributing to $J_s^{(l)}$ are shown above, with $\mu = 0$ for the CE. The components $\chi_{ij}^{(m)}$ contributing to $J_s^{(m)}$ are

$$\chi_{xy}^{(m)} = -\chi_{yx}^{(m)} = (\chi s \omega_{0k})^2 \chi_{xy}^{(l)}, \tag{2.35}$$

where $\omega_{0k} = \sqrt{(\gamma B_c)^2 + (ck)^2}$. For thermal magnons, the ratio $\chi_{xy}^{(m)}/\chi_{xy}^{(l)} \sim (T/T_N)^2$, so J_m can be neglected in I in the limit $T \ll T_N$. We get for the magnetic spin current,

$$J_z(T) = -\left(\frac{\hbar g_m^{\uparrow\downarrow}}{4\pi}\right)\frac{\hbar}{s^2\chi}\int \frac{d^3\boldsymbol{q}}{(2\pi)^3}(\chi s)^2\omega_{0k})\left[\omega_{1k}N(\omega_{1k} - \mu/\hbar) - \omega_{2k}N(\omega_{2k} + \mu/\hbar)\right]. \tag{2.36}$$

Above spin flop

$\delta\boldsymbol{m}$ is elliptically polarized in the ω_{4k} mode, with magnetic fluctuations producing a spin current according to

$$\chi_{xy}^{(m)} = -\chi_{yx}^{(m)} = \frac{i\gamma\chi B}{2}\left(\frac{1}{\omega - \omega_{4k} + i\epsilon} + \frac{1}{\omega + \omega_{4k} + i\epsilon}\right). \tag{2.37}$$

The relation $\chi_{xy}^{(m)} = -\chi_{yx}^{(m)}$ is guaranteed by: Onsager reciprocity, $\chi_{xy}^{(m)}(B) = \chi_{yx}^{(m)}(-B)$, combined with either $\boldsymbol{xz}$ mirror symmetry or π-rotational symmetry about $\hat{\boldsymbol{x}}$ to give $\chi_{yx}^{(m)}(-B) =$

$-\chi_{xy}^{(m)}(B)$ (for $\boldsymbol{B}$ in the plane of the interface). We get for the magnetic spin current,

$$J_z(T) = -\left(\frac{\hbar g_m^{\uparrow\downarrow}}{4\pi}\right) 2\hbar\chi\gamma B \int \frac{d^3k}{(2\pi)^3}\omega_{4k}N(\omega_{4k}). \tag{2.38}$$

2.3.3 Holstein-Primakoff result

The Holstein-Primakoff approximation (defined as the Holstein-Primakoff transformation expanded to second order in the magnon over spin densities) results are obtained analogously to the SBMFT. The HPA spin current is $J_s = J_s^{\mathcal{A}} + J_s^{\mathcal{B}}$, where $J_s^{\mathcal{A}}$ is generated by the coupling $H_{\rm int}^{\mathcal{A}} = (V/\sqrt{N})\sum_{\boldsymbol{k},q,q'} \tilde{a}_{\boldsymbol{k}} c_{q\uparrow} c_{q'\downarrow}^{\dagger}$+H.c, and $J_s^{\mathcal{B}}$ by $H_{\rm int}^{\mathcal{B}} = (V/\sqrt{N})\sum_{\boldsymbol{k},q,q'} \tilde{b}_{\boldsymbol{k}} c_{q\uparrow} c_{q'\downarrow}^{\dagger}$+H.c, where $\tilde{a}, \tilde{b}$ are the magnon operators on the $\mathcal{A}, \mathcal{B}$ sublattices, respectively. These results are a special case of the more general Holstein-Primakoff results derived in Ref.[51], where the interfacial Hamiltonian is treated as the sum of interfacial exchange coupling to each sublattice with separate exchange constants. Our Holstein-Primakoff spin current can be obtained from their general result as follows: $J_s^{\mathcal{A}}$ is obtained by taking their exchange constant for the $\mathcal{B}$ lattice to be zero, and $J_s^{\mathcal{B}}$ by taking their exchange constant for the $\mathcal{A}$ lattice to be zero; then J_s is the sum of these two incoherent contributions weighted by the same exchange constant.

2.3.4 Schwinger boson result

The following section will be published in Ref. [31]. In the AF, the SBs on each sublattice split into mixtures of the bogoliubons parameterized by momentum-dependent coherence

factors. For the AF on the simple cubic lattice $J_s^{\mathcal{A}} \neq J_s^{\mathcal{B}}$, and we get

$$J_s^{\mathcal{A}} = \frac{g_{\uparrow\downarrow}}{2SN^2} \sum_{\boldsymbol{k},\boldsymbol{k'}} \left\{ \sum_{\nu} \epsilon^{\nu\nu}_{\boldsymbol{k}\boldsymbol{k'}\uparrow\downarrow} \left[n_1(\epsilon^{\nu}_{\boldsymbol{k}\uparrow}) - n_1(\epsilon^{\nu}_{\boldsymbol{k'}\downarrow}) \right] \left[n_1(\nu\epsilon^{\nu\nu}_{\boldsymbol{k}\boldsymbol{k'}\uparrow\downarrow}) - n_2(\nu\epsilon^{\nu\nu}_{\boldsymbol{k}\boldsymbol{k'}\uparrow\downarrow}) \right] \left(\delta_{\nu,+} u^2_{\boldsymbol{k}\uparrow} u^2_{\boldsymbol{k'}\downarrow} + \delta_{\nu,-} v^2_{\boldsymbol{k}\uparrow} v^2_{\boldsymbol{k'}\downarrow} \right) \right.$$
$$\left. \sum_{\sigma} \widetilde{\epsilon}^{+-}_{\boldsymbol{k}\boldsymbol{k'}\sigma\sigma} \left[n_1(\epsilon^{+}_{\boldsymbol{k}\sigma}) + n_1(\epsilon^{-}_{\boldsymbol{k'}\sigma}) + 1 \right] \left[n_1(\widetilde{\epsilon}^{+-}_{\boldsymbol{k}\boldsymbol{k'}\sigma\sigma}) - n_2(\widetilde{\epsilon}^{+-}_{\boldsymbol{k}\boldsymbol{k'}\sigma\sigma}) \right] \left(\delta_{\sigma,\uparrow} u^2_{\boldsymbol{k}\sigma} v^2_{\boldsymbol{k'}\overline{\sigma}} - \delta_{\sigma,\downarrow} u^2_{\boldsymbol{k'}\sigma} v^2_{\boldsymbol{k}\overline{\sigma}} \right) \right\}, \tag{2.39}$$

where $\widetilde{\epsilon}^{+-}_{\boldsymbol{k}\boldsymbol{k'}\uparrow\uparrow} \equiv \epsilon^{+}_{\boldsymbol{k}\uparrow} + \epsilon^{-}_{\boldsymbol{k'}\uparrow}$, $\widetilde{\epsilon}^{+-}_{\boldsymbol{k}\boldsymbol{k'}\downarrow\downarrow} \equiv \epsilon^{+}_{\boldsymbol{k'}\downarrow} + \epsilon^{-}_{\boldsymbol{k}\downarrow}$, and $\overline{\nu} = -\nu$, the sum over ν runs over pseudospin indices, and the sum over σ runs over spin indices. Similarly, we get

$$J_s^{\mathcal{B}} = \frac{g_{\uparrow\downarrow}}{2SN^2} \sum_{\boldsymbol{k},\boldsymbol{k'}} \left\{ \sum_{\nu} \epsilon^{\nu\nu}_{\boldsymbol{k}\boldsymbol{k'}\uparrow\downarrow} \left[n_1(\epsilon^{\nu}_{\boldsymbol{k}\uparrow}) - n_1(\epsilon^{\nu}_{\boldsymbol{k'}\downarrow}) \right] \left[n_1(\nu\epsilon^{\nu\nu}_{\boldsymbol{k}\boldsymbol{k'}\uparrow\downarrow}) - n_2(\nu\epsilon^{\nu\nu}_{\boldsymbol{k}\boldsymbol{k'}\uparrow\downarrow}) \right] \left(\delta_{\nu,-} u^2_{\boldsymbol{k}\uparrow} u^2_{\boldsymbol{k'}\downarrow} + \delta_{\nu,+} v^2_{\boldsymbol{k}\uparrow} v^2_{\boldsymbol{k'}\downarrow} \right) \right.$$
$$\left. \sum_{\sigma} \widetilde{\epsilon}^{+-}_{\boldsymbol{k}\boldsymbol{k'}\sigma\sigma} \left[n_1(\epsilon^{+}_{\boldsymbol{k}\sigma}) + n_1(\epsilon^{-}_{\boldsymbol{k'}\sigma}) + 1 \right] \left[n_1(\widetilde{\epsilon}^{+-}_{\boldsymbol{k}\boldsymbol{k'}\sigma\sigma}) - n_2(\widetilde{\epsilon}^{+-}_{\boldsymbol{k}\boldsymbol{k'}\sigma\sigma}) \right] \left(\delta_{\sigma,\uparrow} u^2_{\boldsymbol{k'}\overline{\sigma}} v^2_{\boldsymbol{k}\sigma} - \delta_{\sigma,\downarrow} u^2_{\boldsymbol{k}\overline{\sigma}} v^2_{\boldsymbol{k'}\sigma} \right) \right\}. \tag{2.40}$$

Note that the terms in the second lines of Eqs. (2.39) and (2.40), once combined in the sum $J_s \equiv J_s^{\mathcal{A}} + J_s^{\mathcal{B}}$, vanish quadratically in B so they are negligibly small in the limit $B \ll \sqrt{JK}/\hbar\gamma$ (the spin-flop field). Thus, to linear order in B we have

$$J_s = \frac{g_{\uparrow\downarrow}}{2SN^2} \sum_{\nu,\boldsymbol{k},\boldsymbol{k'}} \epsilon^{\nu\nu}_{\boldsymbol{k}\boldsymbol{k'}\uparrow\downarrow} \left[n_1(\epsilon^{\nu}_{\boldsymbol{k}\uparrow}) - n_1(\epsilon^{\nu}_{\boldsymbol{k'}\downarrow}) \right] \left[n_1(\nu\epsilon^{\nu\nu}_{\boldsymbol{k}\boldsymbol{k'}\uparrow\downarrow}) - n_2(\nu\epsilon^{\nu\nu}_{\boldsymbol{k}\boldsymbol{k'}\uparrow\downarrow}) \right] (u^2_{\boldsymbol{k}\uparrow} u^2_{\boldsymbol{k'}\downarrow} + v^2_{\boldsymbol{k}\uparrow} v^2_{\boldsymbol{k'}\downarrow}). \tag{2.41}$$

The condensate contribution to the spin current comes from separating $n(\epsilon^{+}_{\uparrow})$ ($n(\epsilon^{-}_{\downarrow})$) at the points in the BZ where $\epsilon^{+}_{\uparrow} = 0$ ($\epsilon^{-}_{\downarrow} = 0$). The sums are converted to integrals with the contributions from the condensate density separated explicitly: for an arbitrary function z and a single condensation point at momentum $\boldsymbol{k_c}$, $\sum_{\boldsymbol{k}} z_{\boldsymbol{k}}/N \approx z(\boldsymbol{k_c}) n_c + \mathcal{V} \int_{\mathrm{BZ}} d^3\boldsymbol{k}\ z(\boldsymbol{k})$, where $n_c \equiv N_c/N$ and $\mathcal{V}$ is the unit cell volume. Then, the contribution to the AF J_s due

to the condensate density $n_c \propto L^z$ is

$$J_s^{\rm AF} = \frac{g_{\uparrow\downarrow}}{2s} L^z \int \frac{d^3\boldsymbol{k}}{(2\pi)^3} \frac{2JZA}{\epsilon^+_{\boldsymbol{k}\downarrow} + \epsilon^-_{\boldsymbol{k}\uparrow}} \{\epsilon^+_{\boldsymbol{k}\downarrow} \left[n_1(\epsilon^+_{\boldsymbol{k}\downarrow}) - n_2(\epsilon^+_{\boldsymbol{k}\downarrow})\right] - \epsilon^-_{\boldsymbol{k}\uparrow} \left[n_1(\epsilon^-_{\boldsymbol{k}\uparrow}) - n_2(\epsilon^-_{\boldsymbol{k}\uparrow})\right]\}, \quad (2.42)$$

where $s \equiv S/\mathcal{V}$ is the bulk (saturated) spin density, with spin in units of $\hbar$. The AF J_s has contributions at the two magnon energies, $\epsilon^+_{\boldsymbol{k}\downarrow}$ and $\epsilon^-_{\boldsymbol{k}\uparrow}$, which come with opposite signs since they carry oppositely-oriented spin-angular momentum, as discussed in Ref. [52]. The SBMFT J_s reproduces the semiclassical Néel spin current, Eq. (2.34), evaluated at temperature T_1 minus the backflow at T_2, in the limit $T_1 \ll T_N$.

2.4 Semiclassical spin current in Heisenberg antiferromagnets with easy-plane anisotropy

In the easy-plane AF (somewhat analogous to the easy-axis AF above spin flop), the high-energy mode ω_2 associated with rotation of the Néel order out of the easy plane is a linearly-polarized mode in the nonlinear-σ model. Therefore, in this model it does not yield a spin current. In the canonical ensemble, the spin-spin susceptibilities which contribute to J_s are

$$\chi^{(m)}_{yz} = -\chi^{(m)}_{zy} = \frac{i\gamma\chi B}{2} \left(\frac{1}{\omega - \omega_{1k} + i\epsilon} + \frac{1}{\omega + \omega_{1k} + i\epsilon} \right). \quad (2.43)$$

The magnetic spin current for the easy-plane AF is

$$J_x(T) = -\left(\frac{\hbar g_m^{\uparrow\downarrow}}{4\pi} \right) 2\hbar\chi\gamma B \int \frac{d^3k}{(2\pi)^3} \omega_{1k} N(\omega_{1k}). \quad (2.44)$$

2.5 Dynamic susceptibilities from beyond the nonlinear-σ model

In the semiclassical treatment of the Heisenberg FM, we found a single circularly-polarized eigenmode. In the easy-axis AF below spin flop, we also found two circularly-polarized eigenmodes, which carry opposite spin angular momentum. However, in the easy-axis AF above spin flop and in the easy-plane AF we found linearly-polarized eigenmodes. These do not produce a spin current in the nonlinear-σ model. This is because in that model only transverse fluctuations are allowed, while the spin current requires two perpendicular fluctuating components. In this case, there may still be small longitudinal Néel fluctuations which are not captured by the model. One contribution arises if we relax the nonlinear constraint $\delta \boldsymbol{l}^2 = 1$, allowing for an additional term $\boldsymbol{m} \times \delta E/\delta \boldsymbol{l}$ in the equation of motion for $\boldsymbol{l}$. Explicitly, the equations of motion now are

$$s\frac{\partial \boldsymbol{l}}{\partial t} = -\boldsymbol{H}_m \times \boldsymbol{l} - \boldsymbol{H}_l \times \boldsymbol{m}, \tag{2.45a}$$

$$s\frac{\partial \boldsymbol{m}}{\partial t} = -\boldsymbol{H}_m \times \boldsymbol{m} - \boldsymbol{H}_l \times \boldsymbol{l}, \tag{2.45b}$$

where $\boldsymbol{H}_l \equiv -\delta E/\delta \boldsymbol{l}$ and $\boldsymbol{H}_m \equiv -\delta E/\delta \boldsymbol{m}$ are the effective fields. When we consider linear excitations about the same ground states as before, we now find a Néel spin current that is of order $\sim (\hbar\omega_k/J)^2$, where ω_k is the magnon frequency and J is the AF exchange constant, smaller than the typical Néel spin currents in the nonlinear-σ model. This arises due to the new dynamical term, $\boldsymbol{H}_l \times \boldsymbol{m}$, which generated new (linear) source terms proportional to m_0. Note that Eqs. (2.45) still conserved the individual sublattice spin lengths. We use this model below to compute the dynamic susceptibility components which contribute to J_s.

2.5.1 Easy-axis antiferromagnet above spin flop

Here, the ω_{3k} is associated with linearly polarized eigenvectors for $\delta\boldsymbol{l}$ and $\delta\boldsymbol{m}$, so it does not produce spin currents in the nonlinear-σ model. Solving Eqs. (2.45) linearly about the same ground states as before, we now obtain small elliptical polarization in $\boldsymbol{\delta l}$. This produces a Néel spin current parallel to the field with similar magnitude to the ω_{4k} magnetic spin current,

$$\chi^{(l)}_{xy} = -\chi^{(l)}_{yx} = \frac{i\gamma\chi B}{2}\left(\frac{1}{\omega-\omega_{3k}+i\epsilon}+\frac{1}{\omega+\omega_{3k}+i\epsilon}\right). \tag{2.46}$$

In the case of Cr_2O_3 it pumps at $g_l^{\uparrow\downarrow} \lesssim g_m^{\uparrow\downarrow}$, so we later discard this contribution to SSE from our Cr_2O_3 analysis in Chapter 4.

2.5.2 Easy-plane antiferromagnet

Here, the ω_{2k} is associated with linearly polarized eigenvectors for $\delta\boldsymbol{l}$ and $\delta\boldsymbol{m}$, so it does not produce spin currents in the nonlinear-σ model. Solving Eqs. (2.45) linearly about the same ground states as before, we now obtain small elliptical polarization in $\boldsymbol{\delta l}$. This produces a Néel spin current parallel to the field which, at low fields, is smaller than the magnetic spin current due to the ω_{1k} mode. The high frequency mode's Neel-Neel susceptibility is

$$\chi^{(l)}_{xy} = -\chi^{(l)}_{yx} = \frac{i\gamma\chi B}{2}\left(\frac{1}{\omega-\omega_{2k}+i\epsilon}+\frac{1}{\omega+\omega_{2k}+i\epsilon}\right). \tag{2.47}$$

In the nuclear AF, this yields a Néel spin current at the high frequency mode, ω_{2k}. This mode's nuclear hybridization is weaker, with the hybridized nuclear frequency being the same after replacement $\omega_{1k} \to \omega_{2k}$. Generally, however, this spin current may modify results quantitatively.

2.6 Spin current due to nuclear-magnon-hybridization in antiferromagnets

When nuclear spins and magnons hybridize, there is anti-crossing of the nuclear and magnon bands, as discussed in Chapter 1. In this section our goal is to compute the spin current due to the lowest-energy, long-wavelength nuclear-magnon hybridized spin excitations. With hybridization, the AF spin current has an off-resonance contribution associated with the adiabatic motion of the electrons in the AF at the nuclear frequency. In this section, we use $\boldsymbol{L}$, $\boldsymbol{M}$ for the electronic Néel order and normalized spin density, and $\boldsymbol{l}$, $\boldsymbol{m}$ for the nuclear counterparts.

In this section, we consider nuclear-magnon-hybridization in an easy-plane AF, treated semiclassically. Our system is driven according to the energy density $E(B,t) = E(B) - \boldsymbol{M}\cdot\boldsymbol{H}(t) - \boldsymbol{m}\cdot\boldsymbol{h}(t)$, where $\boldsymbol{H}$ and $\boldsymbol{h}$ are conjugate to $\boldsymbol{M}$ and $\boldsymbol{m}$, respectively. These source terms allow us to calculate nuclear spin-spin susceptibilities. We know that when the nuclear and electronic branches become decoupled, the susceptibilities should also return to their decoupled forms. This occurs in the high temperature limit, when the nuclear spins are totally depolarized, and in the large field limit, when the electronic gap is much larger than the nuclear frequency. When nuclear-magnon coupling is turned on, both the nuclear and electronic dynamic susceptibilities acquire poles at both coupled resonance frequencies. In the limit where coupling vanishes, the other system's pole must be canceled. Thus, in the decoupled limit, each susceptibility should have a root at the other's decoupled frequency. This form appears after explicit calculation.

We analyze the electronic and nuclear spin currents with poles at the nuclear resonance, C_{en} and C_{nn}. Generally, $\omega_1 \gg \omega_n$, so this will be the remaining contribution to the spin Seebeck effect when the electronic mode is frozen out. On the other hand, this freezing

out may not be as sharp as one naively expects, because of the band linewidth. To get a quantitative estimate for the strength of this Lorentzian tail contribution, one can use AFMR data to obtain the magnon linewidths. The classical limit for the nuclear frequency, $\beta\hbar\omega_n \ll 1$, is valid down to 100's of milli Kelvin, and it is therefore a good approximation to replace the Bose-Einstein distribution for the nuclear resonance frequency as Rayleigh-Jeans.

The components of electronic and nuclear χ_{ij} contributing to spin currents are, respectively,

$$\chi_{yz}^{(M)} = i\chi\gamma_m B\omega \frac{\omega^2 - \omega_n^2}{\omega_{mk}^2 - \omega_{nk}^2}\left[\frac{1}{\omega^2 - \omega_{mk}^2} - \frac{1}{\omega^2 - \omega_{nk}^2}\right], \tag{2.48}$$

$$\chi_{yz}^{(m)} = i\chi\gamma_m B\frac{\hbar\omega_n}{k_B T}\omega \frac{\omega^2 - \omega_{1k}^2}{\omega_{mk}^2 - \omega_{nk}^2}\left[\frac{1}{\omega^2 - \omega_{mk}^2} - \frac{1}{\omega^2 - \omega_{nk}^2}\right]. \tag{2.49}$$

Eq. 2.48 tells us how the electronic and nuclear spins are dynamically coupled. Note that the electronic part $\chi_{yz}^{(M)}$ now has a pole at the nuclear frequency, and vice versa for the nuclear part. Note that the decoupled limit, $\omega_{mk} \to \omega_{1k}$ and $\omega_{nk} \to \omega_n$, yields results consistent with our expectations since the pole at the nuclear frequency in $\chi_{yz}^{(M)}$ vanishes in this case, and vice versa. Finally, using the dynamic susceptibilities and fluctuation dissipation theorem [50], we can calculate the semi-classical spin currents. Our formalism does not take into account electronic-nuclear cross correlations such as $\langle L_i l_j \rangle$, $\langle M_i m_j \rangle$, which may warrant future investigation, but whose physical meaning is unclear.

Coupled electronic spin current

In $\chi_{yz}^{(M)}$, there are poles at ω_{mk} and ω_{nk}. The coefficients at the poles, C_{ee} and C_{en}, respectively, are

$$C_{ee}(B,T,k) = \frac{i\chi\gamma_m B}{2}\frac{\omega_{mk}^2-\omega_n^2}{\omega_{mk}^2-\omega_{nk}^2} \approx \frac{i\chi\gamma_m B}{2} \tag{2.50a}$$

$$C_{en}(B,T,k) = \frac{i\chi\gamma_m B}{2}\frac{\omega_n^2\gamma_m^2 B_\Delta^2}{(\omega_{mk}^2-\omega_{nk}^2)\omega_{mk}^2} \ll C_{ee} \tag{2.50b}$$

The on-resonance pole at the electronic frequency has a greater relative weight than at the off-resonance, nuclear frequency. As discussed before, nuclear hybridization does not modify the electronic resonance frequencies much, so the on-resonance response has approximately the same coefficient as the decoupled one. The main effect is the new off-resonance (at the nuclear frequency) contribution to the electronic spin current:

$$J_{x,en} = -\left(\frac{\hbar g_m^{\uparrow\downarrow}}{4\pi}\right) 2\hbar\chi\gamma_m^3 B B_\Delta^2 \int \frac{d^3k}{(2\pi)^3}\frac{\omega_{nk}N(\omega_{nk})}{\omega_{mk}^2}\frac{\omega_n^2}{\omega_{mk}^2}. \tag{2.51}$$

Coupled nuclear spin current

In $\chi_{yz}^{(m)}$, there are poles at ω_{mk} and ω_{nk}. The coefficients at the poles, C_{ne} and C_{nn}, respectively, are

$$C_{ne}(B,T,k) = i\chi\gamma_m B\frac{\hbar\omega_n}{k_B T}\frac{\gamma_m^2 B_\Delta^2}{\omega_{mk}^2-\omega_{nk}^2} \ll C_{nn}, \tag{2.52a}$$

$$C_{nn}(B,T,k) = i\chi\gamma_m B\frac{\hbar\omega_n}{k_B T}\frac{\omega_{1k}^2-\omega_{nk}^2}{\omega_{mk}^2-\omega_{nk}^2} \approx i\chi\gamma_m B\frac{\hbar\omega_n}{k_B T}. \tag{2.52b}$$

and the nuclear spin current and Seebeck coefficient at nuclear resonance is

$$J_{x,nn} - J_{x,n} = \left(\frac{\hbar g_n^{\uparrow\downarrow}}{4\pi}\right) 2\hbar\chi\gamma_m^3 B B_\Delta^2 \frac{\hbar\omega_n}{k_B T} \int \frac{d^3k}{(2\pi)^3} \frac{\omega_{nk} N(\omega_{nk})}{\omega_{mk}^2}, \tag{2.53}$$

where $J_{x,n}$ is the decoupled nuclear spin current.

2.7 Direct nuclear spin current

The following section is published in the theoretical methods Supplementary Material of Ref. [53]. When nuclei are excited in a metal, the dominant relaxation mechanism into the Fermi sea is via spin-conserving flip-flops. Korringa originally described this phenomenon in bulk metals subject to NMR excitation; similarly, nuclei excited by a thermal bias may relax by the same mechanism into an adjacent metal. The result is a thermally-induced spin current which is purely two-dimensional by virtue of the HFI's locality. In this context, we investigate nuclear spin pumping across an interface between an antiferromagnet and a metal. Nuclear spins in the AF interact with the electronic spins in the AF and metal through the dipole interaction. We consider the contact term, which is described by a Heisenberg model. In equilibrium, the strongly fluctuating nuclear spins weakly anti-align to the Néel order, which acts as a field of tens-hundreds of Tesla. Each nuclear spin aligns antiparallel to the electronic spin on the same site, and the net spin current across two adjacent sites cancels unless there is canting of the electronic spins with angle χb. We calculate the nuclear spin current transferred into the metal due to Korringa-like relaxation [1]. As depicted in Fig. 2.4, Korringa determined the spin relaxation rate via Fermi's Golden Rule [1] and got $\tau_k^{-1} \propto a^2 T_e$, where T_e is the temperature of the metal. The factor of T_e arises from the density of particles and holes which may accept the tiny (on the scale of the Fermi energy)

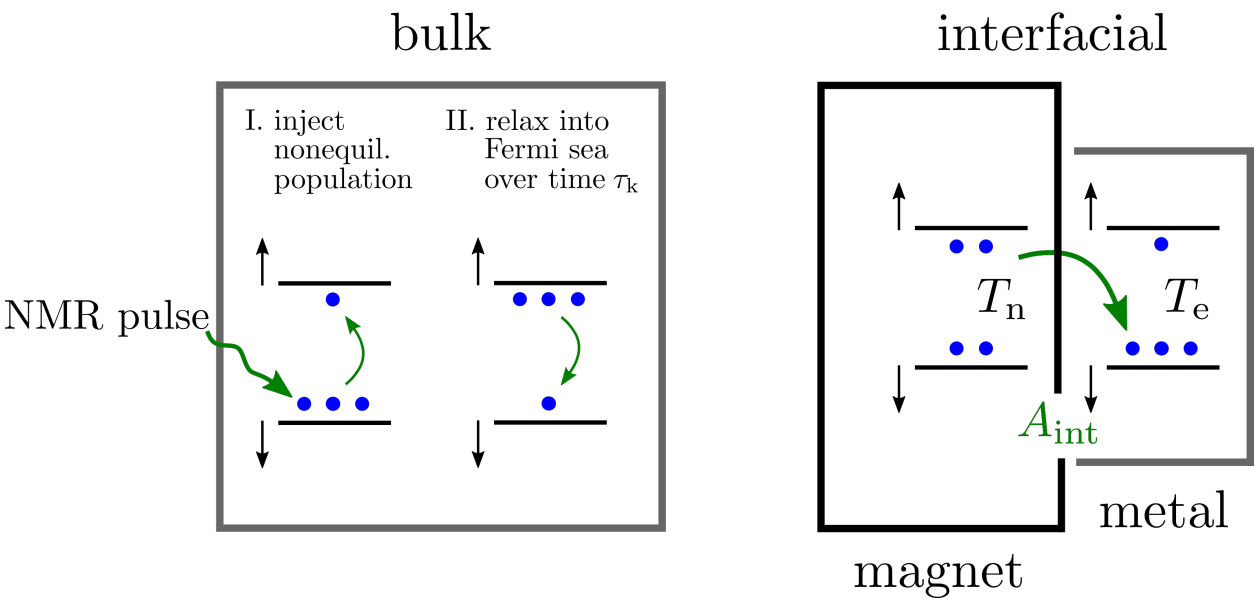

Figure 2.4: On the left, the usual bulk Korringa relaxation [1], where nuclear spins excited by an NMR pulse relax into the Fermi sea. On the right, the similar process of interfacial Korringa relaxation via the interfacial hyperfine interaction A_{int}. In our theory, nuclear spins which are out of equilibrium with an adjacent metal due to their temperature discontinuity $T_n - T_e$, interfacial Korringa relaxation results in a purely 2D interfacial spin current.

nuclear splitting. by Fermi's Golden rule in the limit $k_B T \gg \hbar\omega_n$:

$$J_n = \chi b J_{ne} = \rho(\epsilon_F)^2 a^2 \pi \chi b \hbar\omega_n (T_n - T_e)/T_n, \tag{2.54}$$

here J_{ne} is the spin current per site and J_n is the average over a pair of sites, $\rho(\epsilon_F)$ is the density of states at the Fermi level in units of (energy $\cdot$ volume)$^{-1}$, and a is the interfacial hyperfine interaction constant between nuclei and the spin density in the metal. The temperature dependence in J_{ne} differs from the usual Korringa spin-relaxation rate, $\tau_k^{-1} \propto T$, since J_{ne} is due to the spin flow, minus the backflow, into the Fermi gas. We define the nuclear spin-mixing conductance per unit area as $g_n^{\uparrow\downarrow} \equiv 4\pi s_n \rho(\epsilon_F)^2 a^2$ for saturated nuclear spin density s_n ($s_n \equiv I/\mathcal{A}$, calculated for spin $I = 1/2$ and interfacial area $\mathcal{A}$ per site), in analogy with the electronic result in Ref. [44].

2.8 Spin current in strongly-disordered paramagnets

In Sections 2.2 and 2.3, we derived the interfacial spin currents in insulating magnet/metal heterostructures at arbitrary temperatures in Heisenberg FMs and AFs using SBMFT. We found a paramagnetic-like contribution, $J^{\rm PM}$, that persists into the paramagnetic phase. When we derived the solution to the SBMFT in Chapter 1, we found a liquid PM phase at temperatures between the Curie-Weiss and Curie (Néel) temperature, $\Theta > T > T_{C(N)}$, which then crosses over into a gaseous PM phase. In this section, we compare the SBMFT spin current in the gaseous phase, to the Korringa-like [1] spin current from the previous section, Eq. (2.54). Here, we consider electronic, rather than nuclear spins, but the result is the same up to a change of the gyromagnetic ratio from the nuclear to the electronic one.

2.8.1 Korringa-like result for a single spin

Consider a single spin with $S = 1/2$, at temperature T_1 coupled to an adjacent metal at T_2, in a magnetic field whose Zeeman splitting is $b = \hbar\gamma B$. We compute the transition rates Γ by Fermi's golden rule, which treats the interfacial Hamiltonian as a weak link. We get

$$\Gamma_{\uparrow\downarrow}(T_2) = \frac{2\pi}{\hbar} D^2 V^2 n_2(-b) b, \tag{2.55a}$$

$$\Gamma_{\downarrow\uparrow}(T_2) = -\frac{2\pi}{\hbar} D^2 V^2 n_2(b) b, \tag{2.55b}$$

where V is the strength of interfacial exchange coupling and D is the electronic density of states at the Fermi level. The spin current density is then $J = \hbar(P_\uparrow(T_1)\Gamma_{\uparrow\downarrow}(T_2) - P_\downarrow(T_1)\Gamma_{\downarrow\uparrow}T_2)/\mathcal{A}$, where $\mathcal{A}$ is the area per site of the interface. In terms of the spin-mixing conductance $g_{\uparrow\downarrow} \equiv 4\pi S D^2 V^2/\mathcal{A}$, we get for the interfacial spin current density

$$J_s^{\rm PM} = -\frac{g_{\uparrow\downarrow}}{S} b S^z \left[n_1(b) - n_2(b)\right], \tag{2.56}$$

where S^z is the spin polarization due to the external field $B\hat{\boldsymbol{z}}$. Since we are considering the spin pumping from a single isolated spin, the field splitting does not contain the Curie-Weiss effective field from neighboring spins.

2.8.2 Schwinger boson result

In the gaseous phase the spin Seebeck coefficient in linear response is

$$J_s^{\mathrm{PM}} = \frac{g_{\uparrow\downarrow}}{2S} h \left[n_1(\epsilon_\uparrow) - n_1(\epsilon_\downarrow) \right] \left[n_1(h) - n_2(h) \right] = -\frac{g_{\uparrow\downarrow}}{S} h S^z(h) \left[n_1(h) - n_2(h) \right], \tag{2.57}$$

where $\epsilon_{\uparrow\downarrow} \equiv \epsilon_\uparrow - \epsilon_\downarrow$. This agrees with Eq. (2.56) in the limit where $h = b + JZS^z \approx b$ is the self-consistent Curie-Weiss effective field for Z nearest neighbors. They agree when the Curie-Weiss correction is negligible – the limit where $J \ll T$.

Chapter 3

The spin Seebeck effect in magnetic insulators

The longitudinal spin Seebeck effect is the generation of a spin current J_s along the direction of a thermal flux J_{th} [54, 55, 56], depicted in Fig. 3.1. This can be done with an attached heater, or simply by heating the metal directly with an alternating current. Since spin currents cannot be measured directly, we measure them indirectly by an adjacent metal. Additionally, the symmetry in spin space must be broken in order for a particular direction of the spin current polarization to be selected. This is done by the spontaneously-broken magnetization in FMs, or by applied magnetic fields in AFs and PMs (in AFs, there is a spontaneous Néel ordering, but the contributions from the two sublattices cancel one another identically without an applied field). In ordinary metals, the magnitude of conversion between spin and charge current, θ_{SH}, is on the order of a few percent [57]. While the energy losses due to dissipation in bulk insulating magnet can be quite small (e.g., in ferrimagnetic YIG the magnon diffusion length [58, 59] can be as long as 10 μm, and the length scale of the nonlocal spin Seebeck effect can be around 1μm [60]), the spin-to-charge conversion is a significant bottleneck in the overall efficiency of SSE devices. One route is to engineer

or discover novel materials with larger spin hall angles, such as topological insulators [61]. Another route is to use the thermally-generated spin currents to perform useful work within a spintronic circuit [62].

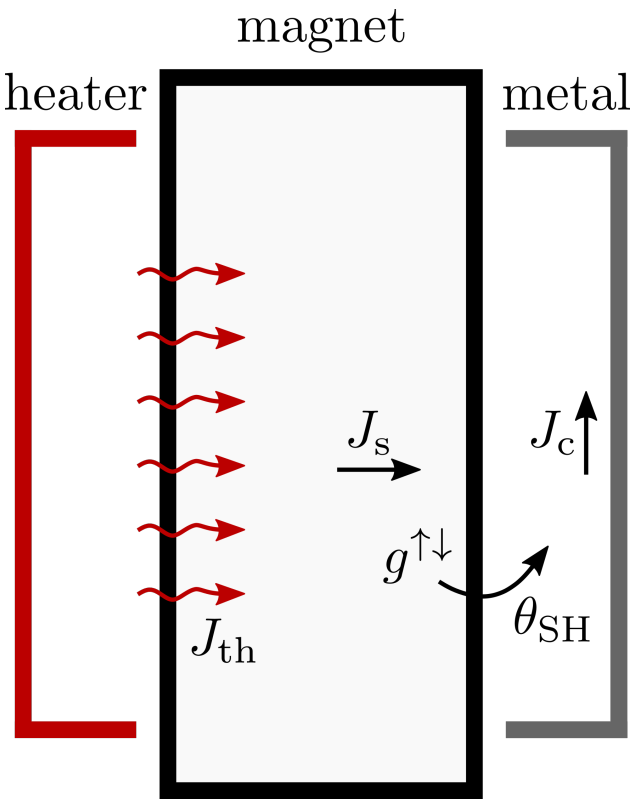

Figure 3.1: The spin Seebeck effect involves the conversion of heat into a spin current in a magnet, which is pumped across the interface with magnitude proportional to the (real part of the) interfacial spin-mixing conductance $g^{\uparrow\downarrow}$. By the inverse spin Hall effect, the spin current in the metal results in a transverse charge current with magnitude proportional to the spin-Hall angle $\theta_{\rm SH}$. This charge current is ultimately measured as a voltage drop in the metal.

SSE has been studied in ferromagnets [63, 64], ferrimagnets [65, 66, 67], paramagnets [2, 68, 69, 70], and recently in antiferromagnets [71, 72, 73, 34, 74] as well as noncollinear magnets [75, 76]. Our theory specializes to SSE from spin currents produced by an interfacial thermal bias. The formalism may be extended to account for bulk thermal gradients, which produce nonequilibrium interfacial spin accumulation μ. The interfacial spin pumping due to μ, could then be evaluated using the generalized fluctuation-dissipation theorem for the grand-

canonical ensemble (derived in Sec. 2.1.2). However, determining μ requires complimenting the interfacial transport with coupled spin and heat transport in the bulk [77], which would go beyond our work. The purely local SSE studied in this thesis should quantitatively model SSE for interfaces with large interfacial thermal resistances and weak interfacial spin coupling. In this regime, SSE would provide a noninvasive probe of the magnet's transverse components of χ_{ij}, much like scanning tunneling microscopy is an interfacial probe of an electron density of states [78].

3.1 Phenomenlogical theory for the SSE in strongly ordered magnets

Deep in the ordered phase of FMs (AFs) at $T \ll T_{C(N)}$, longitudinal fluctuations are frozen out, such that the order parameter may be described by a rigid vector with small transverse fluctuations. The low-energy excitation spectra of these systems was described using a classical, phenomenological framework in Chapter 1. In chapter 2, we leveraged the fact that since magnets break time-reversal symmetry in equilibrium, the are spin currents in equilibrium; and therefore, may be calculated using the fluctuation-dissipation theorem. The semiclassical fluctuation-dissipation theorem related the spin correlators relevant to the spin current in terms of the components of the dynamic susceptibility tensor which are transverse to the order parameter. We computed these components χ_{ij} by adding infinitesimal source terms for magnetic dynamics in the equations of motion. We now turn to an application of this theoretical framework: the spin current generated at the interface between an insulating magnet and a metal subject to a thermal bias. When the interfacial coupling to the adjacent metal may be treated perturbatively to leading order with respect to the bulk magnet's Hamiltonian, this spin current is given by the bulk magnet's spin current evaluated at the temperature of the magnet, minus the same evaluated at the temperature of the metal.

Besides the phenomenological parameters in the bulk magnet's Hamiltonian such as the spin stiffness and strength of anisotropies, there is an overall phenomenological parameter which scales the magnitude of the interfacial spin current. This parameter is the real part of the spin-mixing conductance [42], which describes the dissipative component of spin transfer [49], and is a property of the interface, proportional to the square of the interfacial exchange constant times the metallic density of states at the Fermi level [48]. The interfacial exchange constant is determined by the strength of wavefunction overlap between itinerant electrons in the metal and the localized orbitals in the magnet. In ordinary materials for example the interfacial exchange constant is the following: in FM/metal heterostructures it is the $s-d$ type [79]; for AF/metal heterostructures there are two components [49], which may be assigned to the magnetic part of the spin current and the other to the Néel spin current [50]; and for nuclear spins in a magnet to an adjacent metal it is the interfacial hyperfine interaction [80].

Lastly, a general note about evaluating the integrals over the Brilluoin zone (BZ) in the expressions for the spin Seebeck coefficients. Since this theory is only valid when $T \ll T_{C(N)}$, it will be generally consistent to assume the magnon bandwidths $\Delta E \propto J \propto k_B T_{C(N)} \gg k_B T$, where J is the exchange constant. Each spin Seebeck coefficient contains a factor $\epsilon_k \partial_T n(\epsilon_k)$, where ϵ_k is the magnon dispersion. Thus, when performing these integrals over the BZ, we may evaluate them analytically by formally extending the BZ boundary to infinity. This extension contributes negligibly to the final answer because it is cutoff by the exponential tail of the Bose-Einstein distribution functions.

3.1.1 Phenomenological ferromagnetic SSE at $T \ll T_C$

The dispersion relation for the Heisenberg FM with spin stiffness A, uniaxial easy axis anisotropy constant K, and collinear applied field B is $\omega_k = B + K + Ak^2$, and the spin

current is given by Eq. (2.24). The FM spin Seebeck coefficient is:

$$\mathcal{S} = \frac{\hbar g^{\uparrow\downarrow}}{4\pi s} 2\hbar \int_{BZ} \frac{d^3k}{(2\pi)^3} \omega_k \partial_T n(\omega_k). \tag{3.1}$$

In the limit $k_B T \gg A/a^2 \gg \omega_0$ for lattice spacing a (thermally populated magnons whose band width is much larger than the band gap), we get

$$\mathcal{S}/k_B \approx \frac{\hbar g^{\uparrow\downarrow}}{4\pi s} \left(\frac{k_B T}{\hbar A}\right)^{3/2} \int_0^\infty dx\ x^{5/2} e^x n^2(x) \sim g^{\uparrow\downarrow} \left(\frac{T}{T_C}\right)^{3/2}. \tag{3.2}$$

which agrees with the temperature dependence in Ref. [81].

3.1.2 Phenomenological antiferromagnetic SSE at $T \ll T_N$

Easy-plane antiferromagnet

We consider a Heisenberg AF with spin stiffness A, easy plane anisotropy constant K_1, and within the easy plane mutually-perpendicular easy axis anisotropy constant K_2 and applied field B. The low-energy dispersion is $\omega_{1k} = \sqrt{\gamma^2(B^2 + B_{c2}^2) + c^2k^2}$, with magnetic spin current given by Eq. (2.44), resulting in a magnetic contribution to the spin Seebeck coefficient:

$$\mathcal{S}^{(m)} = \frac{\hbar g_m^{\uparrow\downarrow}}{4\pi} 2\hbar\chi\gamma B \int_{BZ} \frac{d^3k}{(2\pi)^3} \omega_{1k} \partial_T n(\omega_{1k}). \tag{3.3}$$

In the limit $k_B T \gg \gamma\sqrt{B^2 + B_{c2}^2}$ for lattice spacing a (thermally populated magnons whose band width is much larger than the band gap), we get

$$\mathcal{S}^{(m)}/k_B \approx \frac{\hbar g_m^{\uparrow\downarrow}}{4\pi} \gamma\chi B \left(\frac{k_B T}{c\hbar}\right)^3 \frac{1}{\pi^2} \int_0^\infty dx\ x^4 e^x n^2(x) \sim g_m^{\uparrow\downarrow} \frac{\hbar\gamma B}{k_B T_N} \left(\frac{T}{T_N}\right)^3. \tag{3.4}$$

The high-energy dispersion is $\omega_{2k} = \sqrt{\gamma^2 B_c^2 + c^2 k^2}$, with Néel spin current given by Eq. (2.47), resulting in a Néel contribution to the spin Seebeck coefficient:

$$\mathcal{S}^{(l)} = \frac{\hbar g_m^{\uparrow\downarrow}}{4\pi} 2\hbar\chi\gamma B \int_{BZ} \frac{d^3k}{(2\pi)^3} \omega_{2k} \partial_T n(\omega_{2k}). \tag{3.5}$$

Easy-axis antiferromagnet

The following section will be published in Ref. [50]. We consider a Heisenberg AF with spin stiffness A, easy plane anisotropy constant K, and collinear applied field B.

Below spin flop

The dispersions are $\omega_{1k}, \omega_{2k} = \mp\gamma B + \sqrt{(\gamma B_c)^2 + (ck)^2}$. The Néel spin current is given by Eq. (2.34), resulting in a Néel contribution to the spin Seebeck coefficient:

$$\mathcal{S}_{\mathrm{I}}^{(l)} = -\frac{g_l^{\uparrow\downarrow}\hbar^2}{2\pi\chi s^2} \int \frac{d^3k}{(2\pi)^3} \frac{\omega_{1k}\partial_T n(\omega_{1k}) - \omega_{2k}\partial_T n(\omega_{2k})}{\omega_{1k} + \omega_{2k}}. \tag{3.6}$$

In the limit $k_B T \gg \gamma B_{c2}$ for lattice spacing a (thermally populated magnons whose band width is much larger than the band gap), we get

$$\mathcal{S}_{\mathrm{I}}^{(l)}/k_B \approx -\frac{g_l^{\uparrow\downarrow}\gamma B k_B T}{4\pi^3 c^3 \chi s^2} \int_0^\infty dx\ x^2 e^x n^2(x) \sim g_l^{\uparrow\downarrow} \frac{\hbar\gamma B}{k_B T_N} \frac{T}{T_N}. \tag{3.7}$$

The magnetic spin current is given by Eq. (2.36), resulting in a magnetic contribution to the spin Seebeck coefficient:

$$\mathcal{S}_{\mathrm{I}}^{(m)} = -\frac{g_l^{\uparrow\downarrow}\hbar^2\chi}{8\pi} \int \frac{d^3k}{(2\pi)^3} (\omega_{1k} + \omega_{2k}) \left(\omega_{1k}\partial_T n(\omega_{1k}) - \omega_{2k}\partial_T n(\omega_{2k})\right), \tag{3.8}$$

and in the limit $k_BT \gg \gamma B_{c2}$ we get

$$\mathcal{S}_{\mathrm{I}}^{(m)}/k_B \approx -\frac{g_m^{\uparrow\downarrow}\gamma B(k_BT)^3\chi}{4\pi^3c^3}\int_0^\infty dx\ x^4e^x n^2(x) \sim g_m^{\uparrow\downarrow}\frac{\hbar\gamma B}{k_BT_N}\left(\frac{T}{T_N}\right)^3. \tag{3.9}$$

Above spin flop

The dispersions are $\omega_{3k} = ck, \quad \omega_{4k} = \sqrt{\gamma^2B^2 - \gamma^2B_c^2 + (ck)^2}$. The magnetic spin current is given by Eq. (2.38), resulting in a magnetic contribution to the spin Seebeck coefficient:

$$S_{\mathrm{II}}^{(m)} = \frac{g_m^{\uparrow\downarrow}\hbar^2\chi\gamma B}{2\pi}\int\frac{d^3k}{(2\pi)^3}\omega_{4k}\partial_T n(\omega_{4k}), \tag{3.10}$$

In the limit $k_BT \gg \gamma B$ for lattice spacing a (thermally populated magnons whose band width is much larger than the band gap), we get

$$S_{\mathrm{II}}^{(m)} \approx \frac{g_m^{\uparrow\downarrow}\gamma\chi Bk_B^4T^3}{4\pi^3c^3\hbar^2}\int_0^\infty dx\ x^4e^x n^2(x) \sim g_m^{\uparrow\downarrow}\frac{\hbar\gamma B}{k_BT_N}\left(\frac{T}{T_N}\right)^3. \tag{3.11}$$

The Néel spin current is given by Eq. (2.38), resulting in a Néel contribution to the spin Seebeck coefficient:

$$S_{\mathrm{II}}^{(l)} = \frac{g_l^{\uparrow\downarrow}\hbar^2\chi\gamma B}{2\pi}\int\frac{d^3k}{(2\pi)^3}\omega_{3k}\partial_T n(\omega_{3k}), \tag{3.12}$$

In the limit $k_BT \gg \gamma B$ we get

$$S_{\mathrm{II}}^{(l)} \approx \frac{g_l^{\uparrow\downarrow}\gamma\chi Bk_B^4T^3}{4\pi^3c^3\hbar^2}\int_0^\infty dx\ x^4e^x n^2(x) \sim g_l^{\uparrow\downarrow}\frac{\hbar\gamma B}{k_BT_N}\left(\frac{T}{T_N}\right)^3. \tag{3.13}$$

3.2 Schwinger boson theory for the SSE in ferromagnets and antiferromagnets

In the ordered phases, the condensates grow macrospically large and must be separated from the sums over the BZ. The condensate-cloud scattering describes magnonic excitations as shown in Figs. 2.1, 2.2, and 2.3, and dominates J_s at $T \ll T_{C(N)}$, where it reproduces the usual Holstein-Primakoff results, as shown in Fig. 3.2.

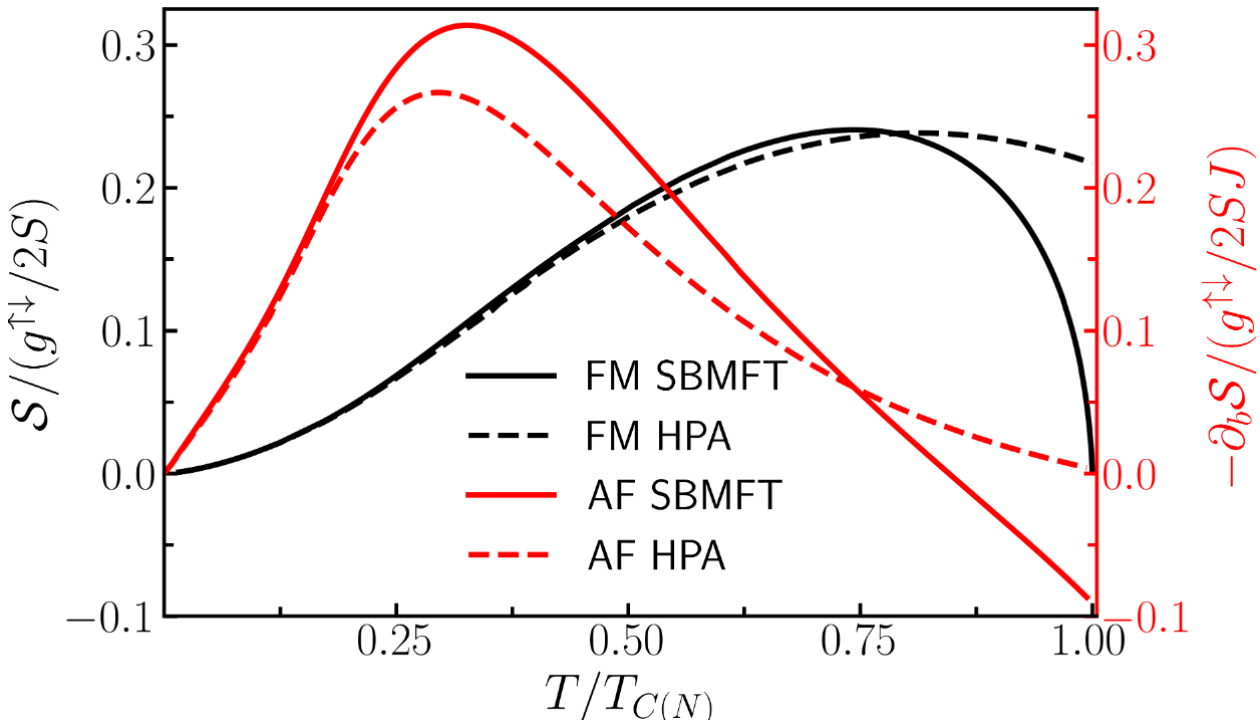

Figure 3.2: The spin Seebeck coefficients for the $S = 1/2$ FM on the diamond lattice and the negative field derivative $-\partial_b\mathcal{S}$ (with $b = \hbar\gamma B$ in units of J) for the $S = 3/2$ AF on the simple cubic lattice computed in the limit $B \to 0$ using SBMFT and HPA. The paramagnetic-like contribution to the SSE is linear in field at $b \ll T$ and therefore only enters in the AF curves plotted here. It has the opposite sign to the magnonic AF SSE, resulting in a zero-crossing at $T^* = 0.85T_N$.

3.2.1 Heisenberg ferromagnet

Cubic lattice

The contribution to the FM spin Seebeck coefficient on a cubic lattice due to the condensate density $n_c \propto S^z$ is

$$\mathcal{S}^{\mathrm{FM}} = \frac{g_{\uparrow\downarrow}}{2s} S^z \int \frac{d^3\boldsymbol{k}}{(2\pi)^3} \partial_T \epsilon_{\boldsymbol{k}\downarrow} n(\epsilon_{\boldsymbol{k}\downarrow}), \tag{3.14}$$

where $s \equiv S/\mathcal{V}$, and $\epsilon_{\boldsymbol{k}\downarrow}$ is the magnon energy. In addition, there is a paramagnetic-like contribution due to scattering between the two continuous spinon bands. For the cubic lattice FM, we get

$$\mathcal{S}^{\mathrm{PM}} = \frac{g_{\uparrow\downarrow}}{2s} \mathcal{V} \int_{\mathrm{BZ}} \frac{d^3\boldsymbol{k}}{(2\pi)^3} \int_{\mathrm{BZ}} \frac{d^3\boldsymbol{k'}}{(2\pi)^3} \epsilon_{\boldsymbol{k}\boldsymbol{k'}\uparrow\downarrow} \left[n(\epsilon_{\boldsymbol{k}\uparrow}) - n(\epsilon_{\boldsymbol{k'}\downarrow}) \right] \partial_T n(\epsilon_{\boldsymbol{k}\boldsymbol{k'}\uparrow\downarrow}), \tag{3.15}$$

where $\epsilon_{\boldsymbol{k}\boldsymbol{k'}\uparrow\downarrow} \equiv \epsilon_{\boldsymbol{k}\uparrow} - \epsilon_{\boldsymbol{k'}\downarrow}$ and $\mathcal{V}$ is the unit cell volume.

Diamond lattice

The contribution to the FM spin Seebeck coefficient on diamond due to the condensate density $n_c \propto S^z$ is

$$\mathcal{S}^{\mathrm{FM}} = \frac{g_{\uparrow\downarrow}}{2s} S^z \int \frac{d^3\boldsymbol{k}}{(2\pi)^3} \partial_T \left[\epsilon^+_{\boldsymbol{k}\downarrow} n(\epsilon^+_{\boldsymbol{k}\downarrow}) + \epsilon^-_{\boldsymbol{k}\downarrow} n(\epsilon^-_{\boldsymbol{k}\downarrow}) \right], \tag{3.16}$$

where $s \equiv S/\mathcal{V}$, and $\epsilon^{\pm}_{\boldsymbol{k}\downarrow}$ are the magnon energies. In addition, there is a paramagnetic-like contribution due to scattering between continuous spinon bands, with scattering between

pseudospin bands also allowed. For the diamond lattice FM, we get

$$\mathcal{S}^{\mathrm{PM}} = \frac{g_{\uparrow\downarrow}}{2s} \sum_{\nu,\nu'} \mathcal{V} \int_{\mathrm{BZ}} \frac{d^3\boldsymbol{k}}{(2\pi)^3} \int_{\mathrm{BZ}} \frac{d^3\boldsymbol{k'}}{(2\pi)^3} \left[n(\epsilon^{\nu}_{\boldsymbol{k}\uparrow}) - n(\epsilon^{\nu'}_{\boldsymbol{k'}\downarrow}) \right] \partial_T n(\epsilon^{\nu\nu'}_{\boldsymbol{k}\boldsymbol{k'}\uparrow\downarrow}), \tag{3.17}$$

where $\epsilon^{\nu\nu'}_{\boldsymbol{k}\boldsymbol{k'}\uparrow\downarrow} \equiv \epsilon^{\nu}_{\boldsymbol{k}\uparrow} - \epsilon^{\nu'}_{\boldsymbol{k'}\downarrow}$, and the sums run over the pseudospin indices $\nu, \nu' = +, -$.

3.2.2 Easy-axis antiferromagnet below spin flop

The AF SBMFT spin Seebeck coefficient is evaluated using Eq. (2.41) in linear response. The contribution to the AF spin Seebeck coefficient due to the condensate density $n_c \propto L^z$ is

$$\mathcal{S}^{\mathrm{AF}} = \frac{g_{\uparrow\downarrow}}{2s} L^z \int \frac{d^3\boldsymbol{k}}{(2\pi)^3} \frac{2JZA}{\epsilon^{+}_{\boldsymbol{k}\downarrow} + \epsilon^{-}_{\boldsymbol{k}\uparrow}} \times \partial_T \left[\epsilon^{+}_{\boldsymbol{k}\downarrow} n(\epsilon^{+}_{\boldsymbol{k}\downarrow}) - \epsilon^{-}_{\boldsymbol{k}\uparrow} n(\epsilon^{-}_{\boldsymbol{k}\uparrow}) \right]. \tag{3.18}$$

In addition, there is a paramagnetic-like contribution due to scattering between continuous spinon bands, with the same pseudospin. For the AF, we get

$$\mathcal{S}^{\mathrm{PM}} = \frac{g_{\uparrow\downarrow}}{2s} \sum_{\nu} \mathcal{V} \int_{\mathrm{BZ}} \frac{d^3\boldsymbol{k}}{(2\pi)^3} \int_{\mathrm{BZ}} \frac{d^3\boldsymbol{k'}}{(2\pi)^3} \epsilon^{\nu\nu}_{\boldsymbol{k}\boldsymbol{k'}\uparrow\downarrow} \left[n(\epsilon^{\nu}_{\boldsymbol{k}\uparrow}) - n(\epsilon^{\nu}_{\boldsymbol{k'}\downarrow}) \right] \partial_T n(\nu \epsilon^{\nu\nu}_{\boldsymbol{k}\boldsymbol{k'}\uparrow\downarrow}) (u^2_{\boldsymbol{k}\uparrow} u^2_{\boldsymbol{k'}\downarrow} + v^2_{\boldsymbol{k}\uparrow} v^2_{\boldsymbol{k'}\downarrow}). \tag{3.19}$$

We call this "paramagnetic-like" because it is linear in field at $b \ll T$, decays exponentially at $b \gg T$, and persists at $T > T_{C(N)}$. In order to carry out the two sets of integrals numerically in $\mathcal{S}^{\mathrm{PM}}$, we approximate the band structure with the low-energy, long-wavelength dispersion: $\epsilon^{\pm}_{\boldsymbol{k}\sigma} \approx \pm(1-\sigma)b/2 + \sqrt{\zeta^2_\sigma - 2Z(JAk)^2}$ for the AF. The SBMFT spin Seebeck coefficients are compared to those computed in the same fashion using the Holstein-Primakoff transformation [48], expanded to second order in the magnon over spin densities (defined as the Holstein-

Primakoff approximation, HPA), and plotted as a function of temperature in Fig. 4.3.

3.2.3 Paramagnetic SSE near $T_{C(N)}$

At arbitrary temperature, J_s also contains a contribution from scattering between bands in the thermal cloud. We call this "paramagnetic-like" because it is linear in field at $b \ll T$, decays exponentially at $b \gg T$, and persists at $T > T_{C(N)}$. In order to carry out the two sets of integrals numerically in $\mathcal{S}^{\mathrm{PM}}$, we approximate the band structure with the low-energy, long-wavelength dispersion: $\epsilon^{\pm}_{\boldsymbol{k}\sigma} \approx JFk^2 - (\mu + b\sigma/2)$ for the FM and $\epsilon^{\pm}_{\boldsymbol{k}\sigma} \approx \pm(1-\sigma)b/2 + \sqrt{\zeta_\sigma^2 - 2Z(JAk)^2}$ for the AF. The SBMFT spin Seebeck coefficients are compared to those computed in the same fashion using the Holstein-Primakoff transformation [48], expanded to second order in the magnon over spin densities (defined as the Holstein-Primakoff approximation, HPA), and plotted as a function of temperature in Fig. 4.3.

In strongly disordered spin systems, spin correlations decay on the scale of the lattice spacing. In SBMFT, this corresponds to JF, $JA \ll T$ and is described by the gaseous phase of the theory (discussed in the next section). In the gaseous phase at $b \ll T$, we get $\partial_B \mathcal{S}^{\mathrm{PM}} = \chi g^{\uparrow\downarrow}$ where χ is the spin susceptibility, normalized by the spin length, defined as $\partial_B S^z/S$. As T decreases below Θ_{CW} in the SBMFT, there is a continuous liquid-gas phase transition and spin correlations start to become significant. When JF or $JA \sim T$, $\partial_B \mathcal{S}^{\mathrm{PM}}$ deviates from χ. Based on this analysis of the Heisenberg model in SBMFT, we introduce a new frustration parameter $p(T) \equiv \partial_B \mathcal{S}/\chi$, whose temperature-dependence is an indicator for short-ranged spin correlations as shown in Fig. 3.3 (for comparison purposes, χ is also computed in the same fashion as $\mathcal{S}^{\mathrm{PM}}$ discussed above).

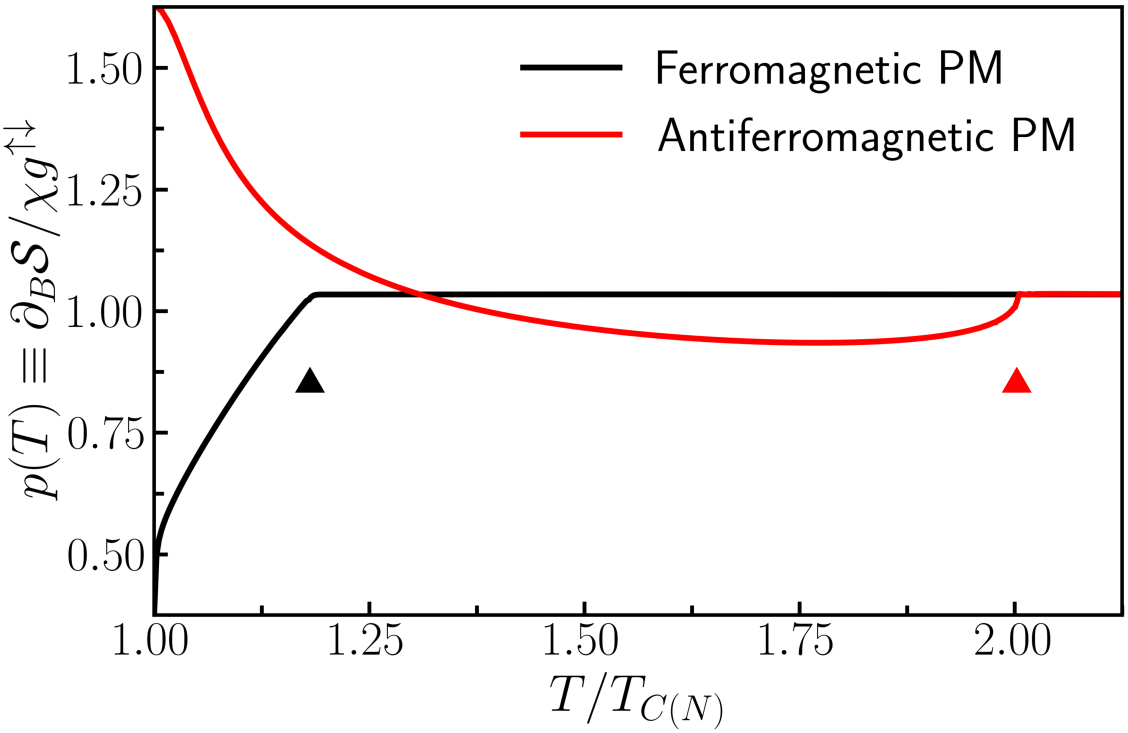

Figure 3.3: Field derivative of the paramagnetic SSE relative to the spin susceptibility in FMs and AFs. $\partial_B \mathcal{S}/g^{\uparrow\downarrow}$ begins to deviate from χ at the liquid-gas crossovers denoted by triangular markers.

3.3 Strongly disordered paramagnetic SSE

In this section we compare the SSE in the completely disordered (gaseous) phase of the SBMFT to the SSE due to an incoherent set of non-interacting spins.

3.3.1 Non-interacting paramagnet

The spin Seebeck coefficient for a single spin is given by Eq. (2.56) in linear response:

$$S^{\mathrm{PM}} = -\frac{g_{\uparrow\downarrow}}{S} S^z b \partial_T n(b), \tag{3.20}$$

where $S^z(b)$ is the spin polarization due to the external field $B\hat{\boldsymbol{z}}$.

3.3.2 Schwinger boson result

In the gaseous phase the spin Seebeck coefficient in linear response is

$$\mathcal{S}^{\mathrm{PM}} = -\frac{g_{\uparrow\downarrow}}{2S} \left[n(\epsilon_\uparrow) - n(\epsilon_\downarrow) \right] \epsilon_{\uparrow\downarrow} \partial_T n(\epsilon_{\uparrow\downarrow}) = -\frac{g_{\uparrow\downarrow} S^z}{S} h \partial_T n(h), \tag{3.21}$$

where $\epsilon_{\uparrow\downarrow} \equiv \epsilon_\uparrow - \epsilon_\downarrow$. The full numerical results with $J = 0$ are plotted in Fig.3.4; when $J > 0$ or $J < 0$ the curve is shifted left and right, respectively, such that the peak in $\mathcal{S}^{\mathrm{PM}}(B)$ occurs at $b \approx T - \Theta_{CW}$.

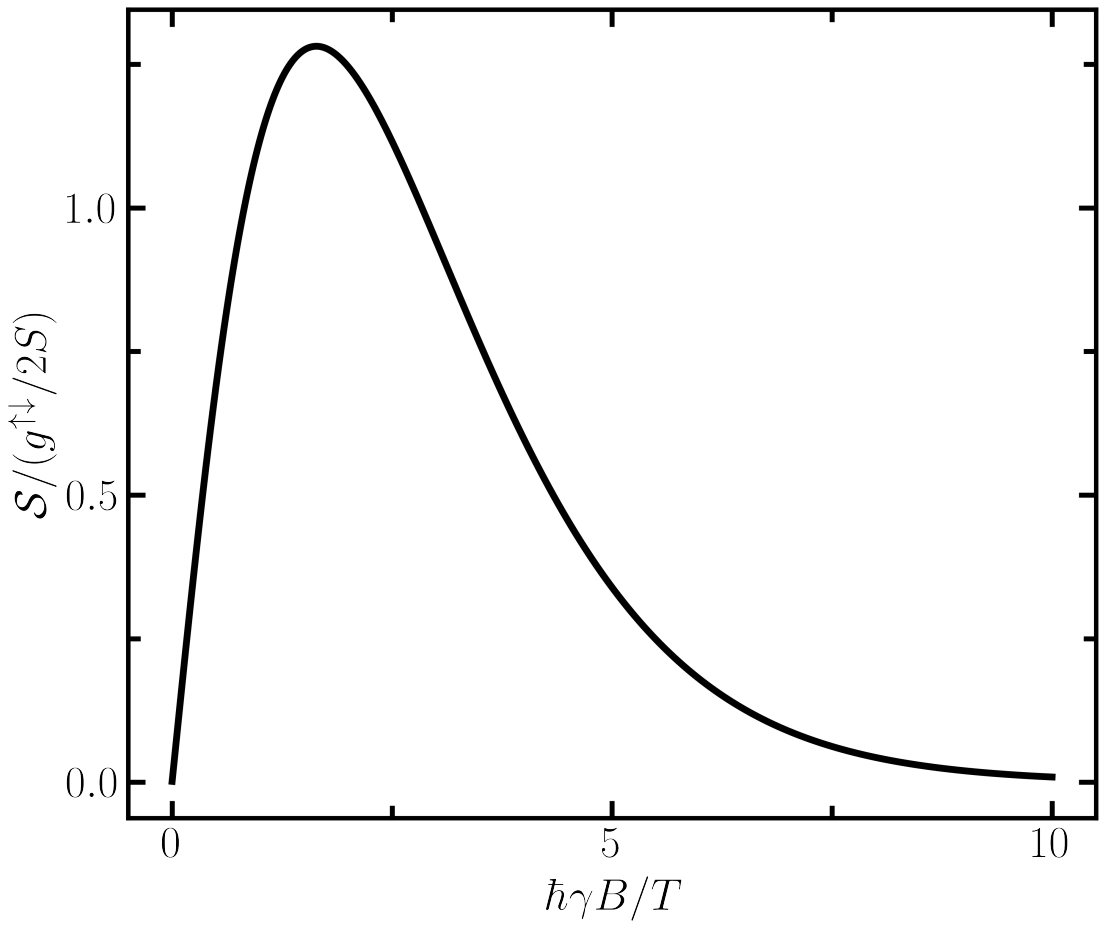

Figure 3.4: The gaseous paramagnetic spin Seebeck coefficient, Eq. (3.21), with $\Theta_{CW} = 0$ as a function of b/T.

3.4 Nuclear SSE

While the electronic spin excitations in magnetically-ordered materials freeze out at low temperatures, nuclear spins remain thermally active. In general, there are three requirements to produce the nuclear SSE: splitting of the spin states, spin coupling to the heat bath, and spin coupling across the interface. This is accomplished by the Heisenberg-like contact

hyperfine interaction (HFI) of the nuclear spin (referred to simply as the nuclei with subscript n) with magnons (with subscript m) which are coupled to phonons (with subscript p), and electrons in an adjacent metal (with subscript e). The full Hamiltonian with a single nuclear spin, modeled as spin-1/2 [1], is

$$\mathcal{H} = -A\boldsymbol{S}_n \cdot \boldsymbol{S}_m - a\boldsymbol{S}_n \cdot \boldsymbol{S}_e(\boldsymbol{r}) + \mathcal{H}_m + \mathcal{H}_p + \mathcal{H}_{mp}, \tag{3.22}$$

where all spins are in units of $\hbar$, $\boldsymbol{S}_n$ and $\boldsymbol{S}_m$ are the nuclear and localized electronic spins on the same site, $\boldsymbol{S}_e(\boldsymbol{r})$ is the metallic spin density evaluated at the nuclear site, A is the bulk HFI constant in units of energy and the nuclear splitting is $\hbar\omega_n = AS_m$, a is the interfacial HFI constant in units of energy times volume, and $\mathcal{H}_m$, $\mathcal{H}_p$ and $\mathcal{H}_{mp}$ are the magnon, phonon, and magnon-phonon interaction Hamiltonians [83]. We suppose that $\mathcal{H}_{mp}$ contains linear coupling between the magnon and phonon field operators.

When nuclei are excited in a metal, the dominant relaxation mechanism into the Fermi sea is via spin-conserving flip-flops. Korringa originally described this phenomenon in bulk metals subject to NMR excitation [1]; similarly, nuclei excited by a thermal bias may relax by the same mechanism into an adjacent metal. The result is a thermally-induced spin current which is purely two-dimensional by virtue of the HFI's locality. In addition, there are nuclear-magnon hybridized, long-wavelength spin excitations in the bulk which also contribute to the SSE. With hybridization, the AF spin current has an off-resonance contribution associated with the adiabatic motion of the electrons in the AF at the nuclear frequency. Our results indicate that at low temperatures, the hybridized contribution dominates the magnonic SSE while the Korringa contribution dominates the nuclear SSE, with the two possibly being comparable to one another depending on system parameters. The two contributions are depicted in Fig. 3.5.

[1] The Gorter relation may be used to describe the relaxation of larger nuclear spin [82] in detailed balance, although we do not expect this to modify our theory qualitatively.

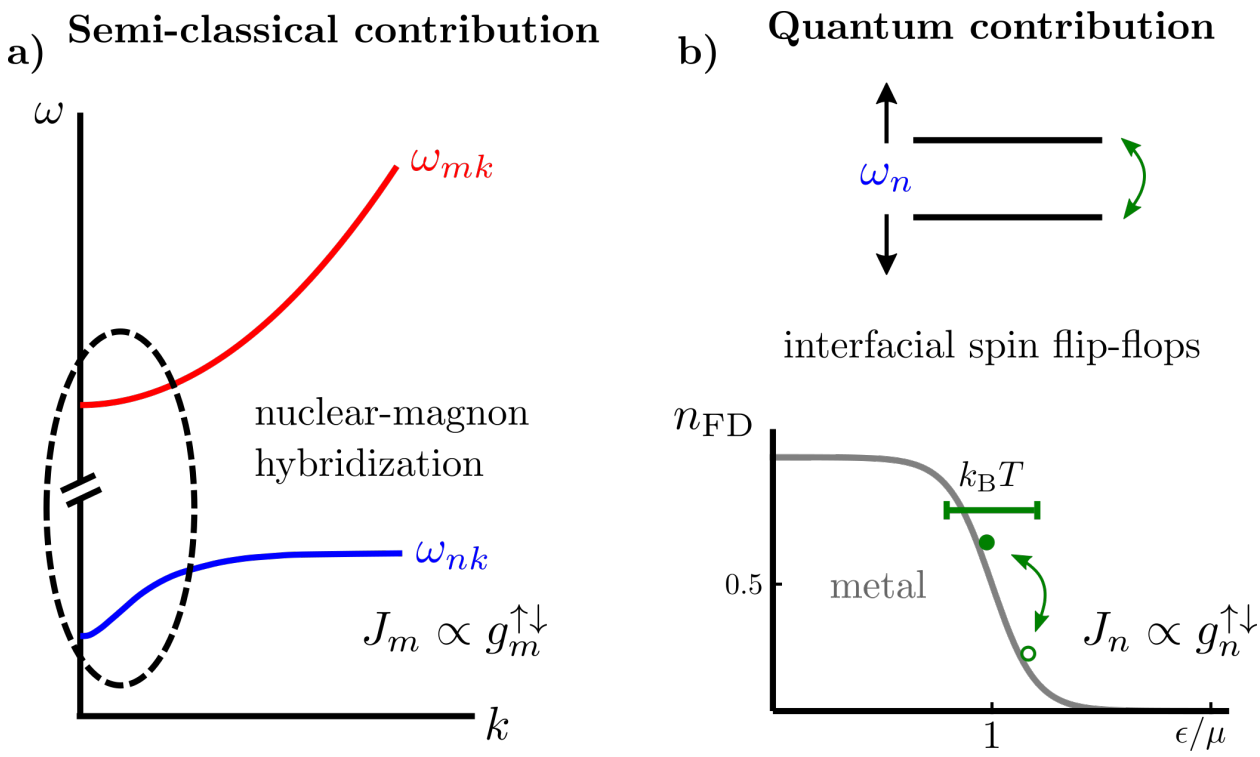

Figure 3.5: The two contributions to the local SSE at low temperatures.

3.4.1 Hybridized nuclear-magnon contributions to the SSE

Since the magnon frequency disperses rapidly on the scale of the nuclear frequency, hybridization is strongest when the magnon gap is small and for long-wavelength magnons near the Gamma point. To capture the SSE due to the lowest-energy spin excitations, we expand the Hamiltonian (Eq. (3.22)) linearly about the uniform, canted (for applied field $B > 0$), Néel ground state, and calculate the semi-classical spin current densities,

$$J_s = \frac{\hbar g_m^{\uparrow\downarrow}}{4\pi} \boldsymbol{M} \times \partial_t \boldsymbol{M}, \tag{3.23}$$

$$J_n^{sc} = \frac{\hbar g_n^{\uparrow\downarrow}}{4\pi} \boldsymbol{m} \times \partial_t \boldsymbol{m}, \tag{3.24}$$

by averaging over thermal fluctuations in the magnet and the metal of the magnetic variables where $g_n^{\uparrow\downarrow}$ and $g_m^{\uparrow\downarrow}$ [49, 50] are the (real part of the dimensionless) nuclear and electronic, respectively, interfacial spin-mixing conductances per unit area. We use the fluctuation-

dissipation theorem, along the lines of Reitz et al. [50], to relate the spin currents to dynamic susceptibilities, thereby converting magnetic response into thermal noise [84].

There are two spin wave modes associated with rotation of Néel order either out of or within the easy-plane. Since we are interested in the SSE at low temperatures here, we discard the higher-energy out-of-plane mode (e.g., in bulk $MnCO_3$ the out-of-plane gap is $B_c \approx 3$ T [85]). The lower-energy mode has elliptically-precessing spin density in the plane perpendicular to the Néel order with frequency gap $\omega_1 = \gamma_m \sqrt{B_{c2}^2 + B^2}$, where B_{c2} is the gap due to anisotropies within the easy-plane (e.g., $B_{c2} \approx 0.2$ T in bulk $MnCO_3$ [86], but may be larger for thin films). For this reason, we have neglected the portion of the electronic spin current due to Néel dynamics in Eq. (3.23), and here $g_m^{\uparrow\downarrow}$ refers to the magnetic (rather than Néel) spin-mixing conductance [49, 50]. Furthermore, we consider low enough temperatures and/or large enough fields so that $\hbar\omega_1 \lesssim k_B T$ and the usual magnonic contribution to SSE is suppressed [81, 50].

At first order in the HFI, the nuclei are polarized by the local electronic magnetization; at second order the nuclei slightly shift the electronic dispersion; and at third order there is effective nuclear-nuclear coupling (nuclear spin waves). The resulting anti-crossing of magnon and nuclear dispersions has been well studied, e.g. [13, 14, 15], and is derived in Chapter 1. We then determined the effects of hybridization on dynamic response which are exhibited in the spin-spin susceptibilities, derived in Chapter 2. In particular, hybridization results in a contribution to the electronic spin current due to its dynamic susceptibility having a second pole, off of its natural resonance at ω_{nk}. The spin Seebeck coefficient arising from this hyrbidization is discussed below. The four contributions to the spin Seebeck effect in a nuclear-magnon hybridized magnet are depicted in Fig. 3.6, since we are interested in the SSE arising at temperatures below the magnon gap we focus on $\mathcal{S}_{mn}$ and $\mathcal{S}_{nn}$ here.

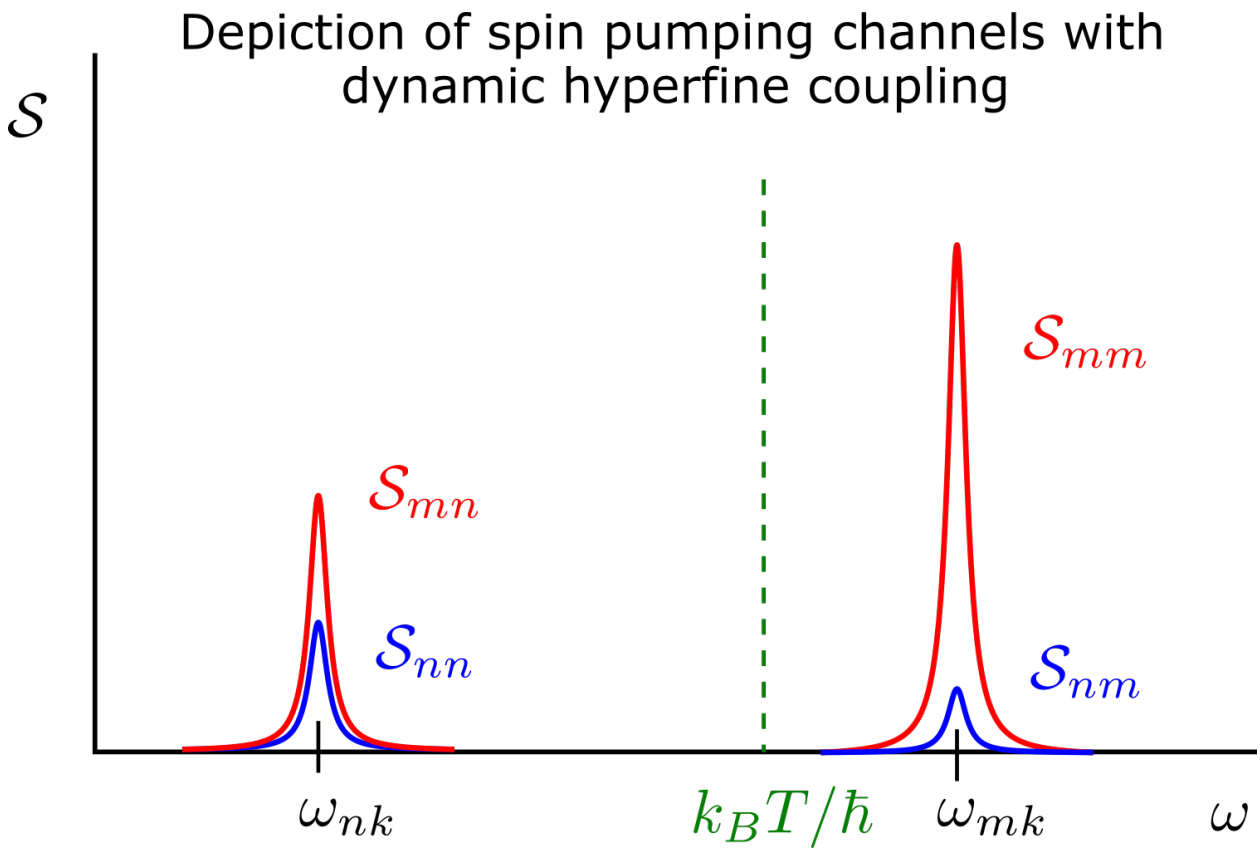

Figure 3.6: Qualitative depiction (not to scale) of the two semiclassical contributions to the magnonic and nuclear Seebeck channels. The magnonic spin Seebeck channel has contributions $\mathcal{S}_{mn}$ and $\mathcal{S}_{mm}$ from spin currents with nuclear and magnonic frequencies, respectively. The nuclear spin Seebeck channel has contributions $\mathcal{S}_{nn}$ and $\mathcal{S}_{nm}$ from spin currents with nuclear and magnonic frequencies, respectively (and also direct nuclear spin currents, discussed in the next section).

Due to the larger mass of nuclei and consequently smaller nuclear gyromagnetic ratio, the nuclear frequency is practically guaranteed to be below k_BT (e.g., $\hbar\omega_n/k_B \sim 80$ mK in $MnCO_3$). With hybridization, the nuclear frequency is pulled downwards to form a nuclear magnon branch, ω_{nk}, with a continuum of thermally-populated modes (for the complete hybridized dispersions, see Eq. 1.28). In this section, we assume the nuclear magnons are internally-equilibrated to a common temperature and take it to be equal to the phonon temperature (mediated by the direct coupling to magnons, which are in turn coupled to phonons by spin-orbit coupling). As derived in Chapter 2, the magnonic spin current has

a pole at the nuclear frequency due to hybridization resulting in a finite spin current at temperatures well below the gap, Eq. 2.51. The resulting contribution to the magnonic spin Seebeck coefficient due to nuclear hybridization is

$$\mathcal{S}_{mn} = -\frac{\hbar g_m^{\uparrow\downarrow}}{4\pi} 2\chi\gamma_m^3 B\omega_n^2 k_B \int \frac{d^3k}{(2\pi)^3} \partial_T \left[\frac{B_\Delta^2 T}{\omega_{mk}^4}\right], \tag{3.25}$$

The nuclear spin current is also modified by hybridization, as shown in Eq. 2.53, resulting in a new contribution to the nuclear spin Seebeck coefficient:

$$\mathcal{S}_{nn} - \mathcal{S}_n = \frac{\hbar g_n^{\uparrow\downarrow}}{4\pi} 2\chi\gamma_m^3 B B_\Delta^2 \hbar\omega_n \int \frac{d^3k}{(2\pi)^3} \partial_T \left[\frac{1}{\omega_{mk}^2}\right], \tag{3.26}$$

where $\mathcal{S}_n$ is the decoupled nuclear spin Seebeck coefficient. Note that both $\mathcal{S}_{nn}$ and $\mathcal{S}_{mn}$ are enhanced at small fields where the magnon gap is small (closer to the nuclear frequency), and at low temperatures due to a larger nuclear spin polarization from the Curie-law [2]. The integrands are also weighted towards the long-wavelength portion of the BZ, where hybridization is strongest.

In order to evaluate $\mathcal{S}_n$, we must generalize the semi-classical theory which is not expected to be quantitatively-precise at short wavelengths. Instead, we should treat the process of nuclear spin relaxation into the metal quantum mechanically, in order to properly evaluate the net spin current as the flow, minus the backflow from the Fermi gas. This is discussed in the next section.

3.4.2 Direct nuclear SSE

The spin Seebeck coefficient relates the spin current pumped across the magnet/metal interface due to a thermal bias between them. In the magnet, the temperature is set by the

[2] At very low temperatures on the order of $\hbar\omega_n$ there are corrections to the inverse-T Curie law; we neglect them here.

phonons at temperature T_p, and in the metal, by the electrons at temperature T_e, so that the spin Seebeck coefficient (in units of inverse area) is defined as

$$\mathcal{S} \equiv J/k_B(T_p - T_e). \tag{3.27}$$

In Chapter 2, we calculated the direct spin current between nuclear spins in a magnet and an adjacent metal by Fermi's golden rule, J_{ne}, given by Eq. 2.54. The nuclear-electron thermalization is parameterized by the nuclear-electron Seebeck coefficient per site, Γ_{ne}, defined by $J_{ne} \equiv \Gamma_{ne} k_B(T_n - T_e)$. Our next step is relate the nuclear spin temperature T_n to the phonon temperature T_p.

3.4.3 Thermal equilibration between nuclear spins and phonons

In thermal equilibrium, the rate of heat flowing into the metal from the spin carriers must be balanced by heat flowing into the carriers from phonons. Throughout this process, we will assume that for magnons, when the temperature is well above their gap, they internally equilibrate to a common temperature. Then, due to strong magnon-phonon coupling the magnon temperature may be taken to be equal to the phonon temperature [81]. For nuclei, there are multiple phonon-thermalization mechanisms. At temperatures well above the magnon gap, magnons can directly transfer the small energy $\hbar\omega_n$ to the nuclei by two-magnon (Raman absorption and remission) and higher-order scattering processes in the magnon continuum [87]. In this limit thermalization with magnons/phonons is much faster than with electrons, so we have $T_n = T_p$. On the other hand, when the temperature is smaller than the magnon gap, virtual magnons can mediate nuclear coupling to phonons. As the temperature decreases relative to the gap, slow thermal equilibration of nuclei to phonons may limit the rate at which spin transport in Eq. (2.54) occurs.

Thermal equilibrium is expressed by balancing the nuclear-electronic spin current J_{ne}

and nuclear-phonon spin current $J_{np} \equiv \Gamma_{np}(T_p - T_n)$ in linear response, where Γ_{ne} and Γ_{np} are the nuclear-electron and nuclear-phonon spin Seebeck coefficients, which are kinetic rate coefficients for the nuclei. In steady state the rates are equal [82], giving us $(T_n - T_e)/(T_p - T_e) = \Gamma_{np}/(\Gamma_{np} + \Gamma_{ne})$. This allows us to construct the empirical spin Seebeck coefficient, Eq. (3.27), by eliminating T_n from Eq. (2.54). The final expression for the nuclear spin Seebeck coefficient becomes

$$\mathcal{S}_n = \frac{g_n^{\uparrow\downarrow}}{4\pi S_n} \pi \chi b \frac{\hbar\omega_n}{k_B T} \left[\frac{\Gamma_{np}}{\Gamma_{np} + \Gamma_{ne}} \right]; \tag{3.28}$$

here, $\chi b \hbar\omega_n \; k_B T$ is the canting angle times the nuclear spin polarization. We may read off $\Gamma_{ne} \propto 1/T$ from Eq. (2.54). When $\Gamma_{ne} \ll \Gamma_{np}$ (corresponding to the high-temperature regime of the previous paragraph), the bracketed expression on the RHS of Eq. (3.28) is unity. Thus we need only calculate Γ_{np} in the low-temperature regime in order to have an asymptotically-precise expression for $\mathcal{S}_n$.

The Hamiltonian allows for indirect coupling between the nuclei and phonons via magnons. Let us define the matrix elements in Eq. (3.22) which linearly couple the dimensionless operators of nuclear spin to the magnon fields, $\mathcal{V}_{mn}$, and magnon fields to phonon fields, $\mathcal{V}_{mp}$. Then to first order in $\mathcal{V}_{mn}$ and $\mathcal{V}_{mp}$, we transition to the high-energy subspace of magnon excitations. We can eliminate these transitions to first order by the Schrieffer-Wolff transformation (SWT) [88, 89], which allows us to construct the effective low-energy Hamiltonian: $\mathcal{H} = \hbar\omega_n \boldsymbol{S}_n \cdot \hat{\boldsymbol{n}} + \mathcal{H}_{np}$ where $\hat{\boldsymbol{n}}$ is the direction of the ground state electronic sublattice magnetization. $\mathcal{H}_{np}$ now contains second-order linear coupling between the nuclear spin and phonon field operators, where the matrix element $\mathcal{V}_{np} \propto \mathcal{V}_{nm}\mathcal{V}_{mp}$.

We may now evaluate Γ_{np} to leading order in perturbation theory for nuclear spin-phonon thermalization via virtual magnons. At temperatures well below the magnon gap ω_1, the mechanism driving J_{np} involves an elastic virtual magnon process (analogous to electronic

elastic cotunneling through quantum dots [90]) which mediates a nuclear spin flip by transmitting energy $\hbar\omega_n$ from phonons. The process occurs near the Gamma point since the energy exchanged is small on the scale of the phonon dispersion. We get the rate from Fermi's Golden rule for the direct coupling $\mathcal{V}_{np}$, averaged over thermal fluctuations. The result is $\Gamma_{np} \propto [n(\omega_1) + 1/2]^2 / T\omega_1^2$, where $n(\omega) = (e^{\hbar\omega/k_B T} - 1)^{-1}$ is the Bose-Einstein distribution function; $n(\omega_1)$ comes from the magnons' thermal occupation number, the 1/2 term from virtual magnons, and ω_1^{-1} from the energy cost to connect nuclei and phonons. We will take the remaining constant in the ratio Γ_{np}/Γ_{ne} from experiment.

3.4.4 Conclusion and outlook for the nuclear SSE

We have investigated the nuclear and electronic contributions to the local SSE at low temperatures. We calculated the contributions due to long-wavelength excitations semi-classically in the presence of nuclear-magnon hyperfine coupling. With hybridization, there is spin pumping via the localized electronic spins in the AF (with spin-mixing conductance $g_m^{\uparrow\downarrow}$) at both the magnonic and nuclear resonance frequencies. We find that the additional contributions to the magnonic Seebeck coefficient due to hybridization are second order in the nuclear Curie-law polarization. In general, contributions due to hybridization have the greatest spectral weight near the Gamma point and are enhanced by a smaller magnon gap and softer dispersion. One significant assumption we have made, in the semiclassical calculation, is that the the hybridized nuclear spin waves thermally equilibrate faster with phonons than with electrons in the metal at all temperatures and fields. This is likely an oversimplification, and a finite phonon thermalization rate should be incorporated into the SSE, as was done for the direct nuclear SSE in Section 3.4.3.

The semi-classical theory for nuclear hybridization developed here is relevant for the SSE at low temperatures in other magnetic systems such as Heisenberg ferromagnets and

antiferromagnets, easy-axis antiferromagnets above spin-flop, and other easy-plane antiferromagnets (e.g. $RbMnF_3$, $CsMnF_3$, $CsMnCl_3$ [91, 92]). In terms of intrinsic parameters, $\mathcal{S}_{mn} \propto g_m^{\uparrow\downarrow}(\gamma_m B/\omega_x)(\delta\omega_n)^4\omega_1/\omega_n^2\omega_x^3$, where $\delta\omega_n$ is the magnitude of the nuclear frequency pulling, and $\omega_x = (\chi s_m)^{-1}$. In AFs, the field exerted on the localized electronic spins by the nuclei are exchange enhanced so $\delta\omega_n$ is larger by a factor ω_x/ω_1 relative to FMs. Thereby we expect that the magnitude of the electronic dynamic susceptibility at the nuclear frequency is smaller in FMs, leading to smaller S_{mn}. For a precise comparison, one must also take into account the changes in the magnon dispersion.

We also identified Korringa-like relaxation of thermally-biased nuclear spins into an adjacent metal as a mechanism for purely two-dimensional interfacial spin transport. Since nuclei have weak spin-orbit coupling, a theory for the nuclear SSE is incomplete without a means for thermal equilibration of the nuclei with phonons. At high temperatures this may be accomplished by Raman-like processes which equilibrate the nuclei directly with the magnon continuum. When magnons are frozen out, virtual magnons mediate thermal equilibration with phonons. Comparing our theory to experiment in the nuclear magnet $MnCO_3$ [80], we are able to rule out the magnonic contributions as inconsistent with the data in this case, while the Korringa-like contribution with thermalization to phonons quantitatively reproduces the data. The latter relies on a single B, T-independent parameter representing the crossover of rate limiting from thermal equilibration with electrons to with phonons. This is discussed in detail in Chapter 4.

Acrosss magnetic systems, the relative magnitude of $\mathcal{S}_{mn}$ and $\mathcal{S}_n$ may vary due to differences in $g_m^{\uparrow\downarrow}$, $g_n^{\uparrow\downarrow}$, and the magnon-phonon coupling strength which affects the position of the field-dependence crossover in $\mathcal{S}_n$. $\mathcal{S}_{mn}$ and $\mathcal{S}_n$ may be distinguished from one another by the temperature-dependence of their crossover fields B_c and $\mathcal{S}(B)$ at $B \gg B_c$. The system parameters in $\mathcal{S}_n$ should not differ significantly between FMs and AFs while S_{mn} is likely smaller in FMs. Therefore it is possibel that $\mathcal{S}_n$ dominates in FMs at low

temperatures. Its contribution to SSE should be observable in any FM with nuclear hyperfine coupling, such as cobalt [93]. At the same time, in this comparison one must also consider that the interfacial spin coupling of the nuclei is much weaker than the electrons: $g_n^{\uparrow\downarrow}/g_m^{\uparrow\downarrow} \sim a^2/j^2 \sim (\omega_n/\omega_x)^2 \ll 1$ (e.g. in $MnCo_3$ $\omega_n/\omega_x \approx 1/1000$), where a and j are the interfacial hyperfine and exchange constants.

This work sets the stage for investigating nonlocal spin transport via nuclear spin waves with dispersion ω_{nk}. Many of the aspects discussed in our theory for local SSE will be relevant to transport, such as nuclear-phonon thermalization and ultimately interfacial spin transport into the metal. Due to the low frequency of ω_{nk} we expect a large nuclear magnon lifetime, which when combined with its small group velocity, may result in a more modest transport length scale. In this regard, we hypothesize that in the Bloch equation for nuclear spin dynamics, the T_1 longitudinal relaxation time is more relevant to SSE than the T_2 dephasing time, since the measured SSE voltage aggregates incoherent contributions.

3.5 Spin Seebeck devices

In this section we discuss a relation for the measured voltage due to the local SSE. The following section was published in Ref. [50]. In a conventional measurement scheme, the (longitudinal) SSE is revealed in a Nernst geometry as a lateral voltage induced perpendicular to the magnetic field applied in the plane of the magnetic interface [64]. This voltage is understood to arise from the inverse spin Hall effect associated with the thermally injected spin current. Normalizing the SSE voltage by the input thermal power P_{in}, this gives

$$\frac{V_{\text{SSE}}}{P_{\text{in}}} = S(B,T)\frac{2e}{\hbar}\frac{\lambda^*}{wt}\frac{\rho(T)}{\kappa^*(T)}, \tag{3.29}$$

where the materials-dependent interfacial spin-to-charge conversion length scale λ^* can be loosely broken down into a product of an effective spin-decay length $\lambda_{\rm sd}$ in the (heavy) normal metal and the effective spin Hall angle $\theta_{\rm SH}$, which converts the spin-current density $J_{\rm s}$ injected into the normal metal into the lateral charge-current density $J_c = (2e/\hbar)\theta_{\rm SH}J_s$. The total charge current is $I_c = w\lambda_{\rm sd}J_c$ when $\lambda_{\rm sd} \ll t$, the thickness of the metal film, where w is the heterostructure width transverse to the injected charge current. In the open circuit, the underlying spin Hall motive force [94] is balanced by the detectable voltage $V_{\rm SSE} = \rho l I_c/wt$, along the length l, where ρ is the normal-metal resistivity. Putting everything together and expressing the spin current in terms of the Seebeck coefficient (3.27), we get the SSE voltage (3.29) normalized by the input power $P_{\rm in} = \kappa(T_p - T_{\rm e})lw$. $\kappa^* = \kappa(T_p - T_e)/(T_a - T_e)$ is an effective Kapitza conductance, which can be reduced relative to κ, if the length scale for the magnon-phonon equilibration that controls the temperature mismatch $T_a - T_p$ in the AF is long compared to σ/κ. Kapitza conductances for metal-insulator interfaces have been investigated in Refs. [95, 96, 97, 98], yielding nontrivial temperature dependences.

Chapter 4

Comparison between theory and experiment

In this chapter we develop quantitative comparisons between experimental data and our theories for the AF SSE and the nuclear SSE at low temperatures, and the paramagnetic SSE at high temperatures. In each case, our goal was to develop a basic understanding of the relevant physics, while minimizing the number of undetermined parameters in our final results. In the words of Von Neumann *"With four parameters I can fit an elephant, and with five I can make him wiggle his trunk [99]."* In other words, a theory with four independent fitting parameters that reproduces data doesn't provide much in the way of establishing credibility. Along these lines, after having developed a theory subject to a certain set of approximations, we should be encouraged to find that our theory becomes inaccurate as we approach the physical regimes where these approximations become invalidated. In this sense, the precise scenario where our theory fails is, equally well, evidence for the integrity of our scientific program.

In the nuclear SSE, we find that as we approach higher temperatures at large magnetic

fields, our theoretical results begins to deviate from the data. In the context of our theory, at large magnetic fields the nuclear SSE is rate-limited by its thermalization with phonons in the magnet, rather than the electrons in the metal. Our theory for nuclear-phonon thermalization contains indirect coupling via virtual magnons, which reproduces the data well at low temperatures where magnons are frozen out. At high temperatures, the nuclei can directly thermalize to the magnon temperature by more complex two-magnon processes, which are not contained in our theory. Thus, we expect this additional effect to enhance the SSE relative to our theory's result in a particular region of parameter space, which indeed is present in the data.

In the final section, we use our Schwinger boson mean-field theory to develop novel quantitative predictions for several SSE experiments, which have yet to be observed. By analyzing our theoretical results, we identify generic signatures of the underlying physics which do not require fine tuning to particular materials, or depend qualitatively on undetermined parameters. The first prediction is a sign change in the SSE as a function of temperature below spin flop in easy-axis AFs, whose location occurs near but below the Néel temperature. The sign of the SSE encodes (up to the sign of the spin Hall angle, an intrinsic property of the adjacent metal), the projection of spin-angular momentum (SAM) along the magnetic field that's carried by the spin current in the magnet. The SAM carried by a spin current at $T \ll T_N$ below spin flop is along the field, while the spin current due to paramagnetic fluctuations, which grow with increasing temperature, carry oppositely-oriented SAM. The fact that this occurs before the phase transition to a paramagnetic phase is a direct prediction of our theory, which captures both contributions to the SSE on equal footing.

4.1 Nuclear SSE in $MnCO_3$

In this section, we compare our theory for the nuclear SSE to ultra-low temperature SSE data [80] at $T < 1$K in $MnCO_3$, a well known nuclear magnet [85, 100, 101]. We evaluate the voltage which arises due to the local SSE, whose Seebeck coefficient has contributions, in principle, from both nuclei and electrons. *A priori* we would expect the magnonic contribution to be larger than the nuclear contribution since electronic exchange provides greater interfacial spin coupling than the HFI. However, at large fields and low temperatures the magnons are frozen out. While this directly affects the magnonic SSE, the nuclei are only indirectly affected through their thermalization with phonons which is mediated by magnons. Since the magnetic field controls the magnon gap, and the nuclei couple to phonons through magnons, it will be the primary comparative tool of the measured SSE signal to theory. The effect of temperature will be to shift the overall profile of the signals' field dependence.

The magnonic and nuclear Seebeck coefficients both have non-monotonic field dependencies which are superficially similar to the experimental data, shown in Fig. 4.1, from E. Saitoh's group Ref. [80]. They both have a linear-in-B factor since the spin currents require canting of the two oppositely-oriented spin sublattices. The magnonic contribution $\mathcal{S}_{mn}$, which is due to hybridization of the magnon dispersion with nuclei, decreases monotonically with field above the small gap B_{c2} within the easy plane. On the other hand, $\mathcal{S}_n$ looks much differently in the asymptotic limit of large fields. As discussed above Eq. (3.28), $\mathcal{S}_n$ is linear in B up to a crossover field $B_c^{(n)}$ marked by Γ_{np} falling below Γ_{ne}; equating Γ_{np} and Γ_{ne} shows that $B_c^{(n)}$ is approximately temperature-independent. In the asymptotic limit $B \gg B_c^{(n)}$, we get $\mathcal{S}_n \propto 1/B$ which further differentiates it from $\mathcal{S}_m$ and $\mathcal{S}_{mn}$.

Experiment shows disagreement with $\mathcal{S}_{mn}$, while most aspects can be reproduced quantitatively by $\mathcal{S}_n$. To start, the data is linear in B over a large range of fields (which rules out $\mathcal{S}_{mn}$ dominating the signal at $B \gg B_{a'}$), so we use the low-field slope $f(T)$ to fit the overall

common factors in Eq. (3.29). It goes as $f(T) \propto 1/(a + bT^c)$ where $a = 8.4$, $b = 2.2$, and $c = 1.6$. Since at small fields $\mathcal{S}_m \propto BT^3$ and $\mathcal{S}_n \propto B/T$, for the magnonic SSE we would need $\kappa_e^*(T) \propto 1/T^3(a + bT^c)$ and for the nuclear SSE we would need $\kappa_n^*(T) \propto T/(a + bT^c)$. These predicted behaviors for $\kappa^*(T)$ do not rule out $\mathcal{S}_m$ because little is known about $\kappa^*(T)$ at low temperatures, but we would not expect higher-order inverse T-dependence. Strong evidence for $\mathcal{S}_n$ comes from the T-*in*dependence of the experimental crossover field B_c, and the slow B-dependence at large fields. For $B \gg B_c^{(m)}$, $\mathcal{S}_m$ is exponentially suppressed by a factor roughly $e^{-B/T}$ where the argument is in units of Tesla / Kelvin. To the contrary, the experimental signal is only decreasing by a factor of $1/B$ there. Furthermore, the behavior of the data at large fields is consistent with $\mathcal{S}_n$.

Having obtained the prefactors in Eq. (3.29) from the experimental field-slope at small B and ruled out the magnonic SSE, we now compare $\mathcal{S}_n$ quantitatively to the entirety of experimental data. As discussed, we expected the bracketed factor in Eq. (3.28) to go to unity in the $B \ll B_c^{(n)}$ limit (which our lower bound for Γ_{np} successfully reproduces), and to $\Gamma_{np}/\Gamma_{ne} \approx C[n(\omega_1) + 1/2]^2/B^2$ in the $B \gg B_c^{(n)}$ limit. We fit the B, T-independent constant C by aligning the theoretical and experimental crossover fields. We now have low and high-field asymptotically-precise expressions for $\mathcal{S}_n$, while our theory is still expected to be imprecise in the crossover region around B_c. In order to predict the exact shape of the crossover we would need a high-temperature theory for nuclear thermalization to the phonon or magnon temperature. However, such a theory would not change the asymptotic limits and only affects a small subset of the data near B_c, so we do not develop it here. One discrepancy, however, is that our theory underestimates the measured signal at large fields relative to the small field data. This might be explained by additional contributions to Γ_{np} such as direct nuclear-phonon coupling through crystalline anisotropies, indirect nuclear-phonon coupling via impurities, and/or the same magnon cotunneling mechanism we have considered but via the second magnon branch associated with spin excitations out of the easy plane. Our theoretically-calculated contribution to Γ_{np} would then give a lower bound on $\mathcal{S}_n$ at large

fields, which is consistent with experiment.

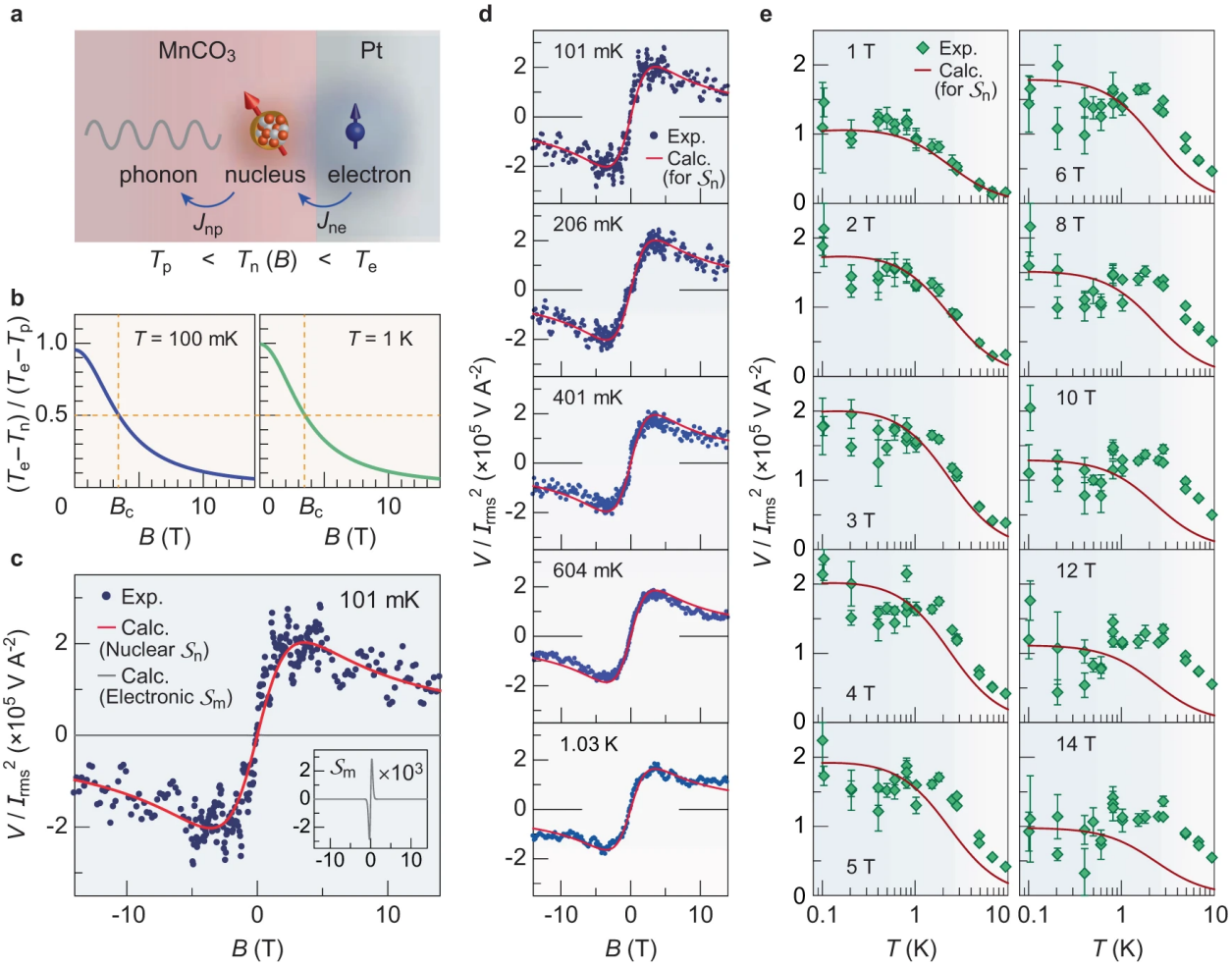

Figure 4.1: Interfacial nuclear-spin current and thermal equilibration of nuclear spins in $MnCO_3$. An interfacial spin current, J_{ne}, is mediated by the Korringa process through the hyperfine interaction between nuclear spins of 55Mn and electron spins in the metal at the Pt/$MnCO_3$ interface. J_{ne} arises in proportion to the effective temperature difference between the electrons in Pt (T_e) and nuclei in $MnCO_3$ (T_n): $J_{ne} = \Gamma_{ne} k_B (T_e - T_n)$. Here, the difference $T_e - T_n$ may be triggered by the interfacial temperature drop $T_e - T_p$ between the Pt and $MnCO_3$ (T_p: phonon temperature in $MnCO_3$ close to the interface) and the thermalization between nuclei and phonons in $MnCO_3$, whose rate is given by $J_{np} = \Gamma_{np} k_B (T_n - T_p)$. b) B dependence of the calculated temperature difference $T_e T_n$, normalized by the interfacial temperature drop $T_e - T_p$ at T=100mK and 1K. In the steady state, $J_{ne} = J_{np}$. B_c indicates the crossover field, where $\Gamma_{ne} = \Gamma_{np}$. c) Comparison between the B dependence of the experimental $V/I^2_{\rm rms}$ (blue plots) for the Pt/$MnCO_3$ Device 2 and the calculated $V/I^2_{\rm rms}$ for the nuclear SSE $\mathcal{S}_n$ (red solid curve) and for the magnonic SSE $\mathcal{S}_m$ (gray solid curve) at T=101mk. The inset shows a blowup of the calculated $V/I^2_{\rm rms}$ for the magnonic SSE (multiplied by 10^3). d) Comparison between the B dependence of the experimental $V/I^2_{\rm rms}$ (blue plots) and the calculated $V/I^2_{\rm rms}$ for the nuclear SSE $\mathcal{S}_n$ (red solid line) at 100mK<T<1K. e) Comparison between the T dependence of the experimental $V/I^2_{\rm rms}$ (green rhombus) and the calculated $V/I^2_{\rm rms}$ for the nuclear SSE $\mathcal{S}_n$ (red solid curve). The error bar represents the standard deviation.

4.2 Antiferromagnetic SSE in Cr_2O_3

In this section we compare our low-energy, long-wavelength phenomenological theory for the SSE in easy-axis AFs to SSE data on Cr_2O_3 [73]. Our key contribution to developing a quantitative comparison between theory and experiment on the AF SSE was to leverage the changing behavior of the magnetic dynamics across the spin flop transition, which is a metamagnetic phase transition. The overall temperature dependence of the measured SSE is convoluted with thermal and charge conductivities (Eq. 3.29) and slower temperature dependencies in parameters such as $\chi(T)$ [11], which can complicate a detailed analysis. By looking at the slope ratio of the SSE below to above spin flop $v(T)$, however, we can eliminate the common prefactor associated with the heat-to-spin-to-charge conversions, if the signal is dominated by the interfacial thermal bias. The experimental $v(T)$ for a bulk Cr_2O_3/Pt sample is plotted in Fig. 4.2 along with theoretical curves. The experimental data points for $v(T)$ are obtained by fitting a linear-in-field line to $V_{\rm SSE}$ in I and II and taking the slope ratio; the theoretical curves are discussed below. It should be safe to suppose that ρ, κ^*, and $g^{\uparrow\downarrow}$ are largely field independent, so that the field dependence in $V_{\rm SSE}/P_{\rm in}$ comes from S. The relative value of $S(B)$ across SF is determined theoretically up to the ratio $g_m^{\uparrow\downarrow}/g_l^{\uparrow\downarrow}$ [1], which is a property of the interfaces.

Our theory contains two contributions each to the spin Seebeck coefficients in I (Eqs. (3.7) and (3.9)) and II (Eqs. (3.13) and (3.11)) for $b \equiv \hbar\gamma B$: $\partial_b S_{\rm I}^{(l)} \sim -g_l^{\uparrow\downarrow} T/T_N^2$, $\partial_b S_{\rm I}^{(m)} \sim -g_m^{\uparrow\downarrow} T^3/T_N^4$, $\partial_b S_{\rm II}^{(l)} \sim g_l^{\uparrow\downarrow} T^3/T_N^4$, $\partial_b S_{\rm II}^{(m)} \sim g_m^{\uparrow\downarrow} T^3/T_N^4$. The $T \ll T_N$ data on Cr_2O_3 was explained using $S_{\rm I} \approx S_{\rm I}^{(l)}$ and $S_{\rm II} \approx S_{\rm II}^{(m)}$, assuming $g_m^{\uparrow\downarrow} \gg g_l^{\uparrow\downarrow}$. However, we see that at intermediate temperatures when $g_m^{\uparrow\downarrow} \gg g_l^{\uparrow\downarrow}$, $S_{\rm I}^{(m)}$ can become significant compared to $S_{\rm I}^{(l)}$.

The ratio of the Néel to magnetic spin Seebeck coefficients is $S_{\rm I}^{(l)}/S_{\rm I}^{(m)} = C_x(g_l^{\uparrow\downarrow}/g_m^{\uparrow\downarrow})(T_A/T)^2$,

[1] Takei *et al.* [49] concluded within their model that the two spin-mixing conductances may be of similar order of magnitude, with $g_m^{\uparrow\downarrow} \gtrsim g_l^{\uparrow\downarrow}$, and $g_l^{\uparrow\downarrow}$ approaching $g_m^{\uparrow\downarrow}$ with increasing disorder of interfacial exchange coupling [102].

where the numerical constant $C_x \approx \int_0^\infty dx\ x^2 e^x n_{\rm BE}^2(x) / \int_0^\infty dx\ x^4 e^x n_{\rm BE}^2(x) \approx 0.1$ and $T_A = \hbar c/a \sim T_N$. Thus, when $(g_m^{\uparrow\downarrow}/g_l^{\uparrow\downarrow})(T/T_N)^2 \sim 0.1$, the two SSE coefficients become comparable. The ratio of the field derivatives of the SSE in I to II, up to intermediate temperatures, is then $-v(T) \sim (g_l^{\uparrow\downarrow}/g_m^{\uparrow\downarrow})(T_N/T)^2 + C_0$, where $C_0 = 1$. The best fit to the experimental $v(T)$, using a fit function which is a constant plus a coefficient times T^{-2}, gives $C_0 = 0.7$ for the constant, which lies reasonably within our expectations. In conclusion, we are able to explain the data up to intermediate temperatures in our theory with the T-independent parameter $g_m^{\uparrow\downarrow}/g_l^{\uparrow\downarrow} \approx 300$. The parameters for Cr_2O_3 are: $\sqrt{A}/a = (\chi\gamma s)^{-1} \approx 500$ T, $B_c \approx 6$ T, $\gamma \approx \gamma_e$ [73] (where γ_e is the free-electron value), $K_2 \approx 0$ [11], $T_n \approx 300$ K.

While we see agreement, there may be additional spin Seebeck contribution(s) not captured by our formalism. The latter can stem from a bulk SSE in state I [103], since thermal magnons polarized along the Néel order can diffuse over long distances [77]. In particular, an additional linear in T contribution to $S_{\rm I}$ would affect the estimate of $g_m^{\uparrow\downarrow}/g_l^{\uparrow\downarrow}$ from the low-T data, while a cubic contribution would shift the constant offset in $v(T)$ at larger temperatures. Although the order-of-magnitude estimate for the mixing conductance ratio and the trend in $v(T)$ as a function of temperature are captured by our simple model, a more complete theory (accounting for the bulk spin transport as well as possibly for disorder-induced mesoscopic effects at the interface) may be needed for developing a complete, detailed understanding.

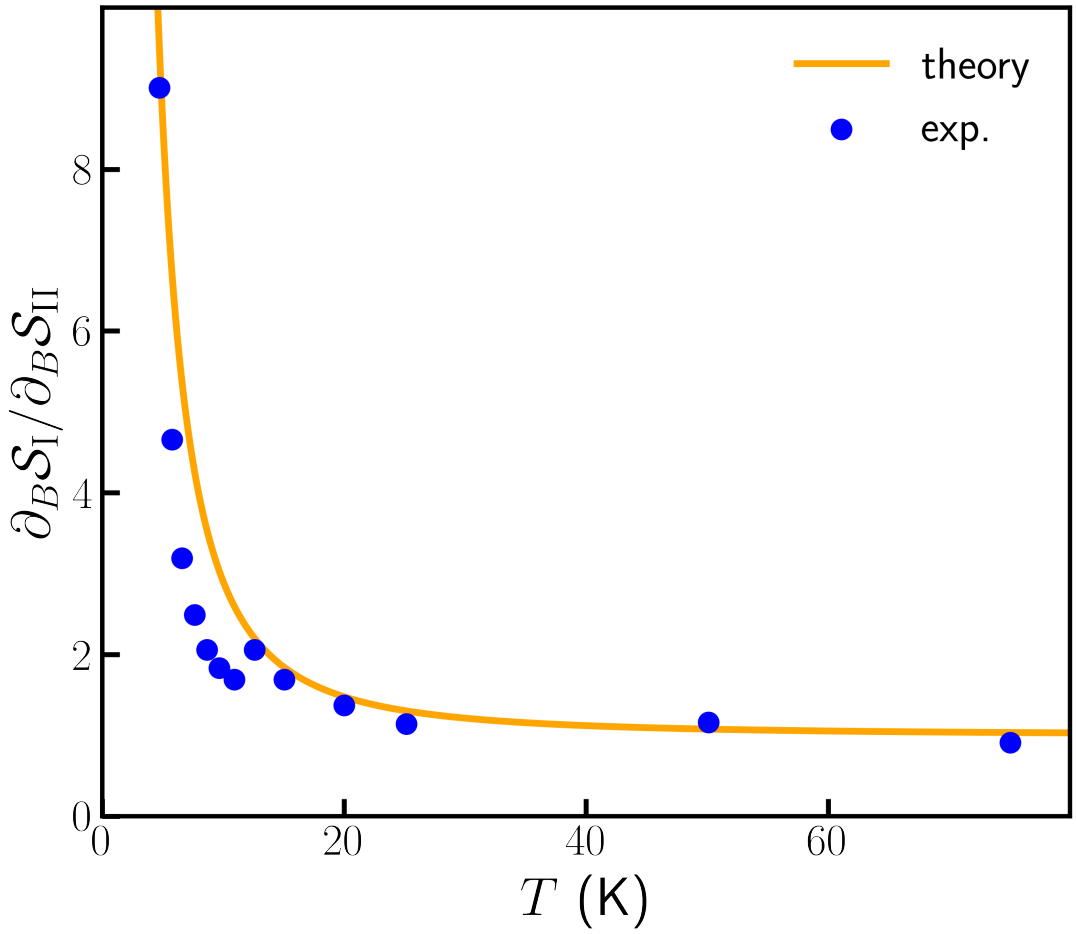

Figure 4.2: The ratio of the spin Seebeck coefficient field slopes $v(T)$. Experimental data is from the same device as in Fig. 4.3(a) and is obtained from the slopes of linear-in-field fit lines. The theoretical curves are based on Eqs. (3.7) and (3.9) below spin flop and Eq. (3.11) above spin flop.

Since our theory succeeded in quantitatively explaining the low temperature SSE data on Cr_2O_3, it was used as a baseline for investigating more complex phenomenon with subtler characteristics. In Ref. [104], magnon polaron coupling was observed in the uniaxial antiferromagnetic insulator by subtracting the our baseline theoretical SSE from the observed SSE at $T < 5$K. At low temperatures $T < 7$ K, the theoretical curves start becoming nonlinear in B, so that $S_{\rm I}, S_{\rm II}$ must be evaluated numerically using the full expressions for the spin

Seebeck coefficients.

4.3 Paramagnetic SSE in GGG

The following two sections will be published in Ref. [31]. In this section we reproduce the temperature evolution of the non-monotonic field dependent SSE observed in gadolinium gallium garnet (GGG) by S. Wu, C. Liu, et al. [2, 3]. The measured spin Seebeck voltage $V(B,T) = \mathcal{S}(B,T)f(T)$ contains additional temperature-dependent factors parameterized by $f(T)$ [52]. Since V is linear in B at $B \ll T$, we can fit to $f(T)$ using $\partial_B V$ evaluated at $B = 0$ as a function of temperature. This procedure was performed in Ref. [2] giving $V \propto T^{-3.38}$, and we use the three $T = 2, 3, 4$K datasets from Ref. [3] to get $V \propto T^{-2.45}$ for that device. After also absorbing $g_{\uparrow\downarrow}/2S$ into $f(T)$, the normalized spin Seebeck voltage in the gaseous phase of the SBMFT is $\partial_B V/f = \chi$, where J is the only undetermined parameter in χ. The magnetic susceptibility of GGG is well known and from the theory we have the relation $\Theta_{CW}/\mathcal{C} = JZ$ where the Curie-Weiss temperature of $\Theta_{CW} = 2.10$K is taken from Ref. [105]. This allows us to plot the theoretical curves shown in Fig. 4.3a,b. We can also extract the field $B^*(T)$ where V is maximized as a function of field, a quantity that is independent of $f(T)$, as a quantitative comparison to our theory shown in Fig. 4.3c. From our theory's point of view, application of the gaseous phase SSE results to this data is consistent until near $T = |\Theta_{CW}|$, where the theory's liquid-gas phase transition occurs. At T somewhat lower than $|\Theta_{CW}|$ there may be enhancements to spin transport resulting in $\partial_B V/f \neq \chi$.

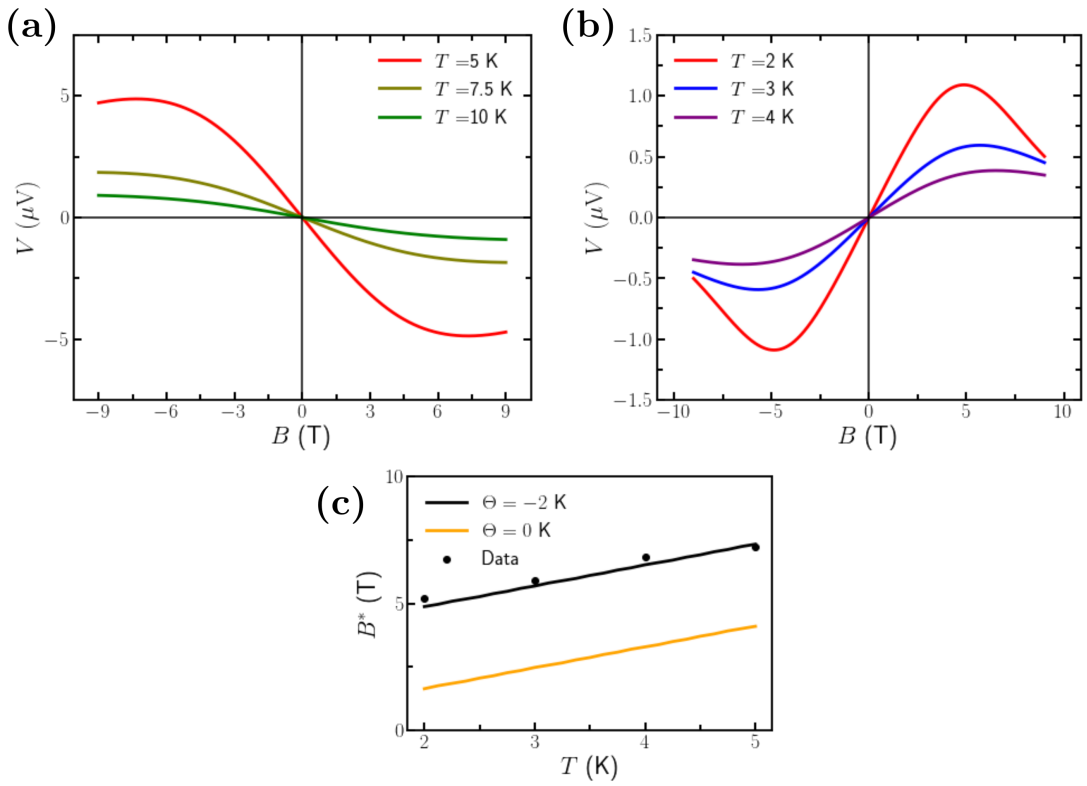

Figure 4.3: Applied field-dependent spin Seebeck voltage data from Refs. [2] in a) and [3] in b), is reproduced by the gaseous phase spin Seebeck coefficient, Eq. (3.21), times a temperature dependent factor taken from the data where $\Theta_{CW} = -2K$ is used. In c) the magnetic field where the SSE is maximized is plotted ($T = 2, 3, 4$K from Ref. [3] and $T = 5$K from Ref. [2]) which depends only on the spin Seebeck coefficient. Fig. c) gives $\Theta_{CW} = -2K$ (antiferromagnetic J) as the best fit, which agrees with independent magnetic susceptibility measurements on GGG.

4.4 Predictions for future experiments

In the paramagnetic phase, across the liquid-gas crossover, the quantity $p(T) \equiv \partial_B \mathcal{S}/\chi$ gains temperature-dependence before T reaches $T_{C(N)}$. However, analysis of experimental $p(T)$ is complicated by the fact that the measured spin Seebeck voltage $V(B,T) = \mathcal{S}(B,T)f(T)$ contains additional temperature-dependent factors in $f(T)$ such as the interfacial thermal conductivity, metallic resistivity and spin diffusion length (see, e.g., Refs. [52, 70]). Starting

at $b \ll T$ and $T \gg T_{C(N)}$, we have $\partial_B \mathcal{S} = g^{\uparrow\downarrow}\chi$, so with an independent measurement of $\chi(T)$ we can accurately determine $f(T)$ from $\partial_B V(T)$. The large-B dependence of $V(B,T)$ then provides a test of our theory, which quantitatively reproduces data at $T \geq 2\text{K} \approx \Theta_{CW}$ in GGG [2, 3]. Furthermore, our theory quantitatively reproduces the field $B^*(T)$ where V is maximized as a function of field, a quantity that is independent of $f(T)$. Going forward, if $f(T)$ remains valid at $T < \Theta_{CW}$, then for devices where $f(T)$ has been measured using the program above, we could compute $\partial_B V/\chi f(T)$ from SSE measurements at lower temperatures. When this quantity is T-dependent at $T < \Theta_{CW}$, it would indicate short-ranged spin correlations are substantially affecting spin transport.

The sign change of the AF spin Seebeck coefficient as a function of temperature below SF at $T^* \approx 0.85T_N$ is another feature which is insensitive to $f(T)$ because it is unlikely to change sign in the same region of T. The spin Seebeck coefficient in a Landau theory for the Néel transition has the paramagnetic sign [69], which is consistent with the SBMFT result in that the latter finds T^* lies appreciably to the left of the critical fluctuation range. While SBMFT is a useful starting point since it contains the basic ingredients needed for a sign change, the interfacial coupling in devices may differ from the type considered here [106, 51]. Additionally, while a bulk thermal gradient can drive an interfacial spin accumulation with the same sign as Eq. (3.18) [34], this accumulation may be reduced and possibly invert in sign when Umklapp scattering becomes significant. Umklapp scattering reduces the diffusion length and occurs when the temperature becomes comparable to the energy of magnons at the Brilluoin zone boundary. This occurs for the lower energy branch before the higher energy branch (with the two carrying oppositely polarized spin angular momentum). If it is significant, then the combined bulk and local SSE may have a lower value for T^*. To give a more quantitative estimate for T^*, a spin transport theory for SBs must be developed.

Bibliography

[1] J. Korringa, Physica **16**, 601 (1950).

[2] S. M. Wu, J. E. Pearson, and A. Bhattacharya, Phys. Rev. Lett. **114**, 186602 (2015).

[3] C. Liu, S. M. Wu, J. E. Pearson, J. S. Jiang, N. d'Ambrumenil, and A. Bhattacharya, Phys. Rev. B **98**, 060415 (2018).

[4] B. Halperin and P. Hohenberg, Physical Review **188**, 898 (1969).

[5] D. P. Arovas and A. Auerbach, Phys. Rev. B **38**, 316 (1988).

[6] S.-S. Zhang, E. A. Ghioldi, L. O. Manuel, A. E. Trumper, and C. D. Batista, Phys. Rev. B **105**, 224404 (2022).

[7] E. Gol'dshtein and V. Tsukernik, Zh. Eksp. Teor. Fiz **87**, 1330 (1984).

[8] X. Liu, W. Zhang, M. J. Carter, and G. Xiao, Journal of Applied Physics **110**, 10.1063/1.3615961 (2011), 033910, https://pubs.aip.org/aip/jap/article-pdf/doi/10.1063/1.3615961/14061663/033910_1_online.pdf .

[9] A. F. Andreev and V. I. Marchenko, Soviet Physics Uspekhi **23**, 21 (1980).

[10] P. Nordblad, L. Lundgren, E. Figueroa, U. Gäfvert, and O. Beckman, Physica Scripta **20**, 105 (1979).

[11] S. Foner, Phys. Rev. **130**, 183 (1963).

[12] B. Flebus, Phys. Rev. B **100**, 064410 (2019).

[13] H. Suhl, Phys. Rev. **109**, 606 (1958).

[14] T. Nakamura, Progress of Theoretical Physics **20**, 542 (1958).

[15] P. G. de Gennes, P. A. Pincus, F. Hartmann-Boutron, and J. M. Winter, Phys. Rev. **129**, 1105 (1963).

[16] L. Abdurakhimov, M. Borich, Y. M. Bunkov, R. Gazizulin, D. Konstantinov, M. Kurkin, and A. Tankeyev, Physical Review B **97**, 024425 (2018).

[17] F. Bloch, Physical review **70**, 460 (1946).

[18] V. L. Safonov, *Nonequilibrium magnons: theory, experiment and applications* (John Wiley & Sons, 2012).

[19] M. A. Ruderman and C. Kittel, Phys. Rev. **96**, 99 (1954).

[20] J. H. Van Vleck, Phys. Rev. **74**, 1168 (1948).

[21] A. W. Overhauser, Physical Review **92**, 411 (1953).

[22] T. R. Carver and C. P. Slichter, Physical Review **102**, 975 (1956).

[23] V. Safonov, Soviet Physics-JETP (English Translation) **67**, 2324 (1988).

[24] S. Okamoto, Phys. Rev. B **93**, 064421 (2016).

[25] R. Samajdar, S. Chatterjee, S. Sachdev, and M. S. Scheurer, Physical Review B **99**, 10.1103/physrevb.99.165126 (2019).

[26] E. Erlandsen and A. Sudbø, Physical Review B **102**, 10.1103/physrevb.102.214502 (2020).

[27] V. S. U. A. Vargas and A. R. Moura, Physical Review B **102**, 10.1103/physrevb.102.024412 (2020).

[28] S. Zhang, E. A. Ghioldi, L. O. Manuel, A. E. Trumper, and C. D. Batista, Physical Review B **105**, 10.1103/physrevb.105.224404 (2022).

[29] L. Messio, C. Lhuillier, and G. Misguich, Physical Review B **87**, 10.1103/physrevb.87.125127 (2013).

[30] E. A. Ghioldi, S.-S. Zhang, Y. Kamiya, L. O. Manuel, A. E. Trumper, and C. D. Batista, Physical Review B **106**, 10.1103/physrevb.106.064418 (2022).

[31] D. Reitz and Y. Tserkovnyak, Unpublished (2023).

[32] O. Tchernyshyov and S. Sondhi, Nuclear Physics B **639**, 429 (2002).

[33] S. Sarker, C. Jayaprakash, H. R. Krishnamurthy, and M. Ma, Physical Review B **40**, 5028 (1989).

[34] S. M. Rezende, R. L. Rodríguez-Suárez, and A. Azevedo, Phys. Rev. B **93**, 014425 (2016).

[35] B. Flebus, Phys. Rev. B **100**, 064410 (2019).

[36] T. Holstein and H. Primakoff, Phys. Rev. **58**, 1098 (1940).

[37] F. Utermohlen, Spin-wave theory using the holstein–primakoff transformation, https://bpb-us-w2.wpmucdn.com/u.osu.edu/dist/3/67057/files/2020/02/spin-wave_theory_using_the_Holstein-Primakoff_transformation.pdf (2020).

[38] S. K. Kim, H. Ochoa, R. Zarzuela, and Y. Tserkovnyak, Physical Review Letters **117**, 10.1103/physrevlett.117.227201 (2016).

[39] S. M. Rezende, A. Azevedo, and R. L. Rodriguez-Suarez, Journal of Applied Physics **126**, 10.1063/1.5109132 (2019), 151101, https://pubs.aip.org/aip/jap/article-pdf/doi/10.1063/1.5109132/13019547/151101_1_online.pdf .

[40] R. Urban, G. Woltersdorf, and B. Heinrich, Physical review letters **87**, 217204 (2001).

[41] S. Mizukami, Y. Ando, and T. Miyazaki, Phys. Rev. B **66**, 104413 (2002).

[42] Y. Tserkovnyak, A. Brataas, and G. E. W. Bauer, Phys. Rev. Lett. **88**, 117601 (2002).

[43] S. P. Pati, Materials Science in Semiconductor Processing **107**, 104821 (2020).

[44] S. A. Bender and Y. Tserkovnyak, Phys. Rev. B **91**, 140402 (2015).

[45] F. Lange, Z. Lenarčič, and A. Rosch, Nature Communications **8**, 15767 (2017).

[46] F. Lange, Z. Lenarčič, and A. Rosch, Phys. Rev. B **97**, 165138 (2018).

[47] Z. Lenarčič, F. Lange, and A. Rosch, Phys. Rev. B **97**, 024302 (2018).

[48] S. A. Bender and Y. Tserkovnyak, Phys. Rev. B **91**, 140402 (2015).

[49] S. Takei, B. I. Halperin, A. Yacoby, and Y. Tserkovnyak, Phys. Rev. B **90**, 094408 (2014).

[50] D. Reitz, J. Li, W. Yuan, J. Shi, and Y. Tserkovnyak, Phys. Rev. B **102**, 020408 (2020).

[51] B. Flebus, Y. Tserkovnyak, and G. A. Fiete, Phys. Rev. B **99**, 224410 (2019).

[52] D. Reitz, J. Li, W. Yuan, J. Shi, and Y. Tserkovnyak, Phys. Rev. B **102**, 020408 (2020).

[53] T. Kikkawa, D. Reitz, H. Ito, T. Makiuchi, T. Sugimoto, K. Tsunekawa, S. Daimon, K. Oyanagi, R. Ramos, S. Takahashi, Y. Shiomi, Y. Tserkovnyak, and E. Saitoh, Nature Communications **12**, 4356 (2021).

[54] H. Adachi, K.-i. Uchida, E. Saitoh, J.-i. Ohe, S. Takahashi, and S. Maekawa, Applied Physics Letters **97**, 252506 (2010).

[55] H. Adachi, J.-i. Ohe, S. Takahashi, and S. Maekawa, Phys. Rev. B **83**, 094410 (2011).

[56] H. Adachi, K. ichi Uchida, E. Saitoh, and S. Maekawa, Reports on Progress in Physics **76**, 036501 (2013).

[57] A. Hoffmann, IEEE Transactions on Magnetics **49**, 5172 (2013).

[58] L. J. Cornelissen, J. Shan, and B. J. van Wees, Phys. Rev. B **94**, 180402 (2016).

[59] J. Shan, L. J. Cornelissen, N. Vlietstra, J. Ben Youssef, T. Kuschel, R. A. Duine, and B. J. van Wees, Phys. Rev. B **94**, 174437 (2016).

[60] K. An, R. Kohno, N. Thiery, D. Reitz, L. Vila, V. V. Naletov, N. Beaulieu, J. Ben Youssef, G. de Loubens, Y. Tserkovnyak, and O. Klein, Phys. Rev. B **103**, 174432 (2021).

[61] N. H. D. Khang, Y. Ueda, and P. N. Hai, Nature Materials **17**, 808 (2018).

[62] S. Zhang and Y. Tserkovnyak, Phys. Rev. Lett. **125**, 207202 (2020).

[63] A. Slachter, F. L. Bakker, J.-P. Adam, and B. J. van Wees, Nature Physics **6**, 879 (2010).

[64] K.-i. Uchida, T. Nonaka, T. Ota, and E. Saitoh, Applied Physics Letters **97**, 262504 (2010).

[65] B. F. Miao, S. Y. Huang, D. Qu, and C. L. Chien, AIP Advances **6**, 015018 (2016).

[66] S. Geprägs, A. Kehlberger, F. Della Coletta, Z. Qiu, E.-J. Guo, T. Schulz, C. Mix, S. Meyer, A. Kamra, M. Althammer, *et al.*, Nature communications **7**, 10452 (2016).

[67] Y. Ohnuma, H. Adachi, E. Saitoh, and S. Maekawa, Phys. Rev. B **87**, 014423 (2013).

[68] J. Li, Z. Shi, V. H. Ortiz, M. Aldosary, C. Chen, V. Aji, P. Wei, and J. Shi, Phys. Rev. Lett. **122**, 217204 (2019).

[69] Y. Yamamoto, M. Ichioka, and H. Adachi, Phys. Rev. B **100**, 064419 (2019).

[70] K. Oyanagi, S. Takahashi, T. Kikkawa, and E. Saitoh, Physical Review B **107**, 10.1103/physrevb.107.014423 (2023).

[71] S. Seki, T. Ideue, M. Kubota, Y. Kozuka, R. Takagi, M. Nakamura, Y. Kaneko, M. Kawasaki, and Y. Tokura, Phys. Rev. Lett. **115**, 266601 (2015).

[72] S. M. Wu, W. Zhang, A. KC, P. Borisov, J. E. Pearson, J. S. Jiang, D. Lederman, A. Hoffmann, and A. Bhattacharya, Phys. Rev. Lett. **116**, 097204 (2016).

[73] J. Li, B. Wilson, R. Cheng, M. Lohmann, M. Kavand, W. Yuan, M. Aldosary, N. Agladze, P. Wei, M. Sherwin, and J. Shi, Nature **578**, 70 (2020).

[74] R. E. Troncoso, S. A. Bender, A. Brataas, and R. A. Duine, Phys. Rev. B **101**, 054404 (2020).

[75] B. Flebus, Y. Tserkovnyak, and G. A. Fiete, Phys. Rev. B **99**, 224410 (2019).

[76] B. Ma, B. Flebus, and G. A. Fiete, Phys. Rev. B **101**, 035104 (2020).

[77] A. Prakash, B. Flebus, J. Brangham, F. Yang, Y. Tserkovnyak, and J. P. Heremans, Phys. Rev. B **97**, 020408 (2018).

[78] J. Tersoff and D. R. Hamann, Phys. Rev. Lett. **50**, 1998 (1983).

[79] S. Zhang and Z. Li, Phys. Rev. Lett. **93**, 127204 (2004).

[80] Takashi et al. collaboration article.

[81] S. Hoffman, K. Sato, and Y. Tserkovnyak, Phys. Rev. B **88**, 064408 (2013).

[82] C. J. Gorter, (Elsevier Publishing Company, 1947).

[83] B. Flebus, K. Shen, T. Kikkawa, K.-i. Uchida, Z. Qiu, E. Saitoh, R. A. Duine, and G. E. W. Bauer, Phys. Rev. B **95**, 144420 (2017).

[84] L. Landau and E. Lifshitz, Publisher: Butterworth-Heinemann **5** (1980).

[85] H. J. Fink and D. Shaltiel, Phys. Rev. **130**, 627 (1963).

[86] H. Fink and D. Shaltiel, Phys. Rev. **137**, AB4 (1965).

[87] B. Flebus and Y. Tserkovnyak, Phys. Rev. Lett. **121**, 187204 (2018).

[88] J. R. Schrieffer and P. A. Wolff, Phys. Rev. **149**, 491 (1966).

[89] S. Bravyi, D. P. DiVincenzo, and D. Loss, Annals of physics **326**, 2793 (2011).

[90] L. P. Kouwenhoven, G. Schön, and L. L. Sohn, in *Mesoscopic Electron Transport*, edited by L. L. Sohn, L. P. Kouwenhoven, and G. Schön (Springer Netherlands, Dordrecht, 1997) pp. 1–44.

[91] G. Witt and A. Portis, Physical Review **135**, A1616 (1964).

[92] M. Petrov and E. Turov, Applied Spectroscopy Reviews **5**, 265 (1972).

[93] A. M. Portis and A. C. Gossard, Journal of Applied Physics **31**, S205 (1960).

[94] K. Uchida, T. Ota, K. Harii, S. Takahashi, S. Maekawa, Y. Fujikawa, and E. Saitoh, Solid State Communications **150**, 524 (2010).

[95] R. J. Stoner, H. J. Maris, T. R. Anthony, and W. F. Banholzer, Phys. Rev. Lett. **68**, 1563 (1992).

[96] R. J. Stevens, A. N. Smith, and P. M. Norris, Journal of Heat Transfer **127**, 315 (2005).

[97] G. T. Hohensee, R. Wilson, and D. G. Cahill, Nature communications **6**, 6578 (2015).

[98] T. Lu, J. Zhou, T. Nakayama, R. Yang, and B. Li, Phys. Rev. B **93**, 085433 (2016).

[99] F. Dyson, Nature **427**, 297 (2004).

[100] L. Svistov, J. Low, and H. Benner, Journal of Physics: Condensed Matter **5**, 4215 (1993).

[101] Y. Shiomi, J. Lustikova, S. Watanabe, D. Hirobe, S. Takahashi, and E. Saitoh, Nature Physics **15**, 22 (2019).

[102] R. Cheng, J. Xiao, Q. Niu, and A. Brataas, Phys. Rev. Lett. **113**, 057601 (2014).

[103] R. Lebrun, A. Ross, S. Bender, A. Qaiumzadeh, L. Baldrati, J. Cramer, A. Brataas, R. Duine, and M. Kläui, Nature **561**, 222 (2018).

[104] J. Li, H. T. Simensen, D. Reitz, Q. Sun, W. Yuan, C. Li, Y. Tserkovnyak, A. Brataas, and J. Shi, Phys. Rev. Lett. **125**, 217201 (2020).

[105] Y. J. Kim, C.-Y. Liu, S. K. Lamoreaux, G. Visser, B. Kunkler, A. N. Matlashov, J. C. Long, and T. G. Reddy, Phys. Rev. D **91**, 102004 (2015).

[106] Y. Luo, C. Liu, H. Saglam, Y. Li, W. Zhang, S. S.-L. Zhang, J. E. Pearson, B. Fisher, T. Zhou, A. Bhattacharya, and A. Hoffmann, Phys. Rev. B **103**, L020401 (2021).